SYNTHESIS AND CHARACTERIZATION OF INORGANIC-ORGANIC HYBRID SEMICONDUCTOR MATERIALS FOR ENERGY APPLICATIONS

by

MOJGAN ROUSHAN

A Dissertation submitted to the

Graduate School – New Brunswick

Rutgers, The State University of New Jersey

in partial fulfillment of the requirements

for the degree of

Doctor of Philosophy

Graduate Program in Chemistry and Chemical Biology

written under the direction of

Professor Jing Li

and approved by

_____

_____

_____

_____

New Brunswick, New Jersey

October 2012

ABSTRACT OF THE DISSERTATION

Synthesis and Characterization of Inorganic-Organic Hybrid Semiconductor Materials for Energy Applications

By MOJGAN ROUSHAN

Dissertation Director:

Professor Jing Li

In the past few years, it has been shown that inorganic-organic hybrid semiconductors are promising candidates for optoelectronics and clean energy applications. These materials have the advantage of combining the excellent electrical, optical, thermal and transport properties of inorganic components with the flexibility, processability and structural diversity of the organic components. A representative of such materials is the inorganic-organic hybrids based on II-VI semiconductors. We have developed a unique class of II-VI based hybrids composed of alternating layers of double atomic slabs of Zn_2S_2 and organic amine molecules. The Zn_2S_2 based double-layer hybrids emit bright white light and their internal quantum efficiencies have reached ~33-35%, very close to the performance level of the (YAG):Ce^{3+} yellow phosphors presently dominating the white light emitting diodes (WLED) market. We have demonstrated that their band-gap and photoluminescence properties, quantum yield and color quality can be systematically tuned by varying the doping level and composition of inorganic and organic components. Therefore, these white-light emitting hybrid semiconductors represent a new type of single-

phased phosphors made of semiconductor bulk materials with great promise for use in WLEDs which are of intense interest for general illuminations.

Furthermore, we have successfully synthesized a series of new hybrid materials containing one-dimensional chains or two-dimensional layers of V-VI motifs with organic spacers between the channels or the layers. Inserting organic amines in these crystal lattices reduces the thermal conductivity without any significant effect on the electrical conductivity, and thus, it may give rise to an increase in the figure of merit, a parameter that characterizes the effectiveness of thermoelectric devices. The ability to tune the optical, electrical, and thermal properties, coupled with their high fluorescence quantum yield, solution processability, low-temperature and cost-effective one-pot synthesis, precisely controllable stoichiometry and high yield, not only make these hybrid materials promising candidates for use in WLEDs, but also highly versatile semiconductors for a range of applications such as optoelectronics, energy generation, and conversion devices.

ACKNOWLEDGEMENTS

I would like to express my sincere gratitude to my supervisor, Prof. Jing Li, providing me an opportunity to do this work and for her continuous support, guidance, and encouragements throughout my graduate career. Her enthusiasm and optimism has made my research experience truly enjoyable. I would also like to gratefully thank Prof. John Brennan, Prof. Ki-Bum Lee, and Prof. Wei Jiang, not only for serving on my thesis committee, but also for their valuable comments, technical advises and suggestions. I would also like to express my appreciation for the current and former members of the group for all the support and creating a joyful environment to work in. I would especially like to thank Xiao Zhang for his intellectual advice and thought-provoking ideas. I feel very lucky to have worked with him. My thanks also go to Dr. Wooseok Ki for helping me get started in the first year and always being good consultants. I would also like to thank Dr. Yonggang Zhao and Dr. Ruibo Zhang for fruitful discussions and for patiently answering all my questions. I also wish to thank other members of our group Dr. Sanhita Pramanik, Yuchu Chen, Jingming Zhang, Qihan Gong, Zhichao Hu, Voshadhi Amarasinghe, Yin Wang, Haohan Wu and Zhijuan Zhang for their help and friendship. I am grateful for collaborators inside and outside Rutgers University. From Rutgers, I enjoyed the pleasant collaborations and discussions with Dr. Hisato Yamaguchi and Dr. Manish Chhowalla, and Hokwon Kim, for their help in electrical and optical measurements. I also benefited from valuable discussions Dr. Thomas J. Emge, as well as the course taught by him. I also wish to thank him for his helping analyzing the single crystal data. I wish to acknowledge the collaborations with Dr. Ronggui Yang at the University of Colorado at Boulder for thermal

conductivity measurement. I acknowledge funding from National Science Foundation via Grant No. DMR-0706069 and Nanotechnology for Clean Energy IGERT, Grant No. DMR-0903661. I would also like to gratefully thank Nanotechnology for Clean Energy, IGERT program for providing a great educational and funding opportunity and special thanks to Dr. Johanna Bernstein, for her help and comments and advises in preparing the poster for NSF competition and for organizing IGERT events.

Finally, my deepest gratitude goes to my husband, Dr. Pedram Roushan. I cannot thank him enough for everything he has taught me. If I have been able to accomplish anything these past few years it is only because we walked through it together. His encouragement and support made it possible for me to pursue my dreams. I also thank my parents for all the sacrifices that they made to provide a safe and nurturing environment for me and for their encouragements and supports throughout my life.

DEDICATION

To my husband

For his loving support

TABLE OF CONTENTS

Abstract……...….ii

Acknowledgments…….…..iv

Dedication……...vi

Table of contents……...….vii

List of tables…….x

List of illustrations……..……xi

List of abbreviations……..xv

Chapter 1. Introduction…….1

1.1 II-VI semiconductors ……...2

1.1.1. Structure……...3

1.1.2. Applications…….3

1.2 II-VI based hybrid semiconductors……7

1.2.1 Structure……...…8

1.2.2 Properties……11

1.3 V-VI semiconductors……11

1.3.1 Structures……11

1.3.2 Properties……12

1.4 V-VI based hybrid semiconductors……14

1.5 Solvothermal synthesis……16

1.6 References……19

Chapter 2. Optical properties of double layer II-VI based hybrid semiconductors...23

2.1 $Zn_2S_2(L)$ ……25

2.1.1 Structure……..25

2.1.2 Optical band-gap……26

2.1.3 Photoluminescence……...26

2.2. Effect of doping on optical properties……29

2.2.1 Selenium substitution……..29

2.2.2 Cadmium substitution……..30

2.2.3 Manganese substitution……35

2.3. Effect of Ligand on optical properties……..38

2.4. Conclusions……...40

2.5. References……43

Chapter 3. Mechanical properties of 3d-single layer II-VI based hybrid semiconductors …….45

3.1 Introduction to mechanical properties……46

3.2 Structure of 3D-α-ZnTe $(L)_{0.5}$……..…..48

3.3 Experimental……...48

3.3.1 Synthesis and sample preparations……..48

3.3.2 Methods……49

3.4 Results……..50

3.5 Conclusions……..52

3.6 References……52

Chapter 4. Synthesis and characterization of V-VI based hybrid semiconductors ….53

4.1 (Sb_2Se_3) (Sb_3Se_5) (*dien*H)……55

4.1.1 Synthesis……55

4.1.2 Structure……..55

4.1.3 Properties……61

4.2 (Sb_3Se_5) (*hda*H)……66

4.2.1 Synthesis……66

4.2.2 Structure……..66

4.2.3 Properties……70

4.3 (Sb_4Se_6) (Sb_3Se_5) (*amp*H)……74

4.3.1 Synthesis……74

4.3.2 Structure……..74

4.3.3 Properties……76

4.4 (Sb_2Se_3) (Sb_3Se_5) (*ba*H)……82

4.4.1 Synthesis and Structure……..82

4.4.2 Properties……..83

4.5 Bismuth based hybrids……84

4.5.1 Bi_xS_y (*L*) (L= *en, pda*)……...84

4.5.2 Bi_xSe_y (*en*)……87

4.5.3 $Bi_xCu_ySe_z$ (*en*)……...88

4.6 Conclusions……...90

4.7 References……91

Appendices

Appendix I: Methods and Instruments……..93

Appendix II: Quantum yield calculation……..96

Appendix III: Experimental data for chapter two…….101

LIST OF TABLES

Table 1.1 Room temperature bandgaps (Eg) of some II-VI compounds……..7

Table 1.2 Summary of thermoelectric figure of merit value for selected Chalcogenide compounds……...16

Table 2.1 GSAS Rietveld refinement results for 2D-Zn_2S_2 (*L*)……...26

Table 2.2 CCT, CRI and CIE data of the selected hybrid compounds……..36

Table 2.3 GSAS Rietveld refinement results for 2D-Zn_2S_2 (*L*)……..41

Table 4.1 Crystal data and structure refinement for (Sb_2Se_3) (Sb_3Se_5) (*dien*H)…….57

Table 4.2 Selected bond distances (Å) and angeles (deg) for (Sb_2Se_3) (Sb_3Se_5) (*dien*H)……..58

Table 4.3 Sb-Se bond distance of inorganic phase of Sb_2Se_3 compare to the (Sb_2Se_3) (Sb_3Se_5) (*dien*H) hybrid phase……...58

Table 4.4 Crystal data and structure refinement for (Sb_3Se_5) (*hda*H)……69

Table 4.5 Selected bond distances (Å) and angels (deg) for (Sb_3Se_5) (*hda*H)……..73

Table 4.6 Crystal Data and structure refinement for (Sb_7Se_{11}) (*amp*H)…….78

Table 4.7 Selected bond distances (Å) and angels (deg) for (Sb_7Se_{11}) (*amp*H)……..79

Table A1 Summary of PL quantum yields calculated based on comparative and absolute methods……97

Table A2 TGA data for selected II-VI based hybrids……..103

Table A3 Summary of elemental analysis for $Zn_{1.7}Cd_{0.3}S_2$ (*ha*)……105

LIST OF ILLUSTRATIONS

Figure 1.1 Unit cell of zincblende structure and wurtzite structure……4

Figure 1.2 View of single layer 3D-MQ $(L)_{0.5}$ type hybrid structure……...10

Figure 1.3 View of (a) single layer of honeycomb-like net of II-VI, (b) single-chain 1D-MQ (*L*) structure, c) single layer 3D-MQ$(L)_{0.5}$ structure, (d) single-layer 2D-MQ(*L*) structure, and (e) double-layer 2D-M_2Q_2(*L*) structure……...11

Figure 1.4 View of the structure of (a) rhombohedral, Bi_2Te_3, (b) Bi_2S_3, with *B2mm*, (c) Sb_2S_3 with *C2/c*, and (d) Sb_2Se_3 with *Pbnm*……...13

Figure 2.1 View of (a) double layer of honeycomb-like net of ZnS in the M_2Q_2(*L*) type hybrid structures, (b) double-layer 2D-M_2Q_2(*L*) structure……27

Figure 2.2 Comparison of PXRD patterns of 2D-Zn_2S_2 (*ba*), 2D-Zn_2S_2 (*ha*) and 2D-Zn_2S_2(*oa*) structures……27

Figure 2.3 Room temperature absorption spectra of Zn_2S_2 (*ba*) compare to ZnS…….28

Figure 2.4 (a) Room temperature emission spectra of Zn_2S_2 (*ba*) and ZnS, (b) CIE coordinates of ZnS, Zn_2S_2(*ba*)……28

Figure 2.5 Room temperature absorption spectra of $Zn_2S_{2-y}Se_y$ (*ba)*……..31

Figure 2.6 Room temperature emission spectra of $Zn_2S_{2-y}Se_y$ (*ba*)……...31

Figure 2.7 Room temperature absorption spectra of $Zn_{2-x}Cd_xS_2$ (*ba*)……....33

Figure 2.8 Room temperature emission spectra of $Zn_{2-x}Cd_xS_2$ (*ba*)……..33

Figure 2.9 Room temperature emission spectra of (a) $Zn_{1.7}Cd_{0.3}S_2$(*ba*) with 15% Cd and Cd_2S_2(*ba*), (b) $Zn_{1.7}Cd_{0.3}S_2$(*ba*) and Zn_2S_2(*ba*)……34

Figure 2.10 White-light assemblies using the 2D-$Zn_{1.7}Cd_{0.3}S_2$ (*ba*) phosphors……..34

Figure 2.11 Room temperature absorption spectra of $Zn_{1.7}Cd_{0.3}S_2$ (*ha*):Mn……...37

Figure 2.12 Room temperature emission spectra of $Zn_{1.7}Cd_{0.3}S_2$ (*ha*): Mn……..37

Figure 2.13 Integrated emission intensity of $Zn_{1.7}Cd_{0.3}S_2$ (*ha*): Mn as a function Mn dopant amount (0.02-0.5 mol%)……..38

Figure 2.14 **(**a) White-light LED assemblies made by coating thin-film samples on the surface of a 5 mm reference UV LED (b) bright white light from a $Zn_{1.7}Cd_{0.3}S_2$(*ha*):0.08%Mn and (c) from $Zn_{1.7}Cd_{0.3}S_2$(*ha*) deposited on glass excited at 365 nm with a UV lamp……..39

Figure 2.15 Room temperature emission spectra of $Zn_{1.7}Cd_{0.3}S_2$ (*L*).....42

Figure 2.16 Room temperature absorption spectra of $Zn_{1.7}Cd_{0.3}S_2$(*L*).....42

Figure 3.1 Stress–strain plots for the α-ZnTe$(L)_{0.5}$-type hybrid structures in comparison with three reference materials……..51

Figure 3.2 A free-standing film specimen made from a powder sample of ZnTe (*hda*) $_{0.5}$……..51

Figure 4.1 ORTEP diagram of (Sb_2Se_3) (Sb_3Se_5) (*dien*)……...57

Figure 4.2 Observed and stimulated PXRD patterns (Sb_4Se_6) (Sb_3Se_5) (*dien*H)……..59

Figure 4.3 View of packing of 1D-arrays of Sb_2Se_3 and Sb_3Se_5 chains in (Sb_2Se_3) (Sb_3Se_5) (*dien*H)……..59

Figure 4.4 **(**a) Building unit of (Sb_2Se_3) (Sb_3Se_5) (*dien*H), (b) View of 1D-chains 59

Figure 4.5 View of the structure of (Sb_2Se_3) (Sb_3Se_5) (*dien*H)……60

Figure 4.6 Structure of Sb_2Se_3……..60

Figure 4.7 Thermogravimetric analysis data for (Sb_2Se_3) (Sb_3Se_5) (*dien*H)……62

Figure 4.8 Room temperature optical absorption spectra of (Sb_2Se_3) (Sb_3Se_5) (*dien*H) and Sb_2Se_3……..62

Figure 4.9 SEM image showing the thickness of film of (Sb_4Se)(Sb_3Se_5)(*dien*H)…...63

Figure 4.10 I-V curve for (a) (Sb_4Se) (Sb_3Se_5) (*dien*H), and (b) Sb_2Se_3…….63

Figure 4.11 (a**)** Specific heat, (b) thermal diffusivity plots for (Sb_4Se) (Sb_3Se_5) (*dien*H) and Sb_2Se_3 ……...65

Figure 4.12 Thermal conductivity plots for (Sb_4Se) (Sb_3Se_5) (*dien*H)……65

Figure 4.13 Observed and stimulated PXRD patterns (Sb_3Se_5) (*hda*H)……...67

Figure 4.14 ORTEP diagram of (Sb_3Se_5) (*hda*H)……68

Figure 4.15 Structure of (Sb_3Se_5) (*hda*H)……..68

Figure 4.16 View of 1D-chains in (Sb_3Se_5) (*hda*H)……69

Figure 4.17 TGA data for (Sb_3Se_5) (*hda*H)……..71

Figure 4.18 Room temperature optical absorption spectra of (Sb_3Se_5) (*hda*H)……71

Figure 4.19 SEM image showing the thickness of film of (Sb_3Se_5) (*hda*H)……72

Figure 4.20 I-V curve for (a) (Sb_3Se_5) (*hda*H), and (b) Sb_2Se_3……72

Figure 4.21 (a**)** Specific heat, (b) thermal diffusivity plots for (Sb_3Se_5) (*hda*H)……75

Figure 4.22 Thermal conductivity plots for (Sb_3Se_5) (*hda*H)……75

Figure 4.23 (a) View of the structure of (Sb_7Se_{11}) (*amp*H), (b) Sb_3Se_5 units, (c) shows the connection of two Sb_3Se_5 units via corner-sharing, (d) connection of $\{Sb_3Se_5\}_2$ to another Sb_3Se_5 unit via six coordinated Sb atoms……77

Figure 4.24 TGA data showing weight losses of 8.2% for (Sb_7Se_{11}) (*amp*H)……80

Figure 4.25 Room temperature optical absorption spectra of (Sb_7Se_{11}) (*amp*H)……80

Figure 4.26 I-V curve for (Sb_7Se_{11}) (*amp*H)……..80

Figure 4.27 (a) Specific heat, (b) thermal diffusivity plots for (Sb_7Se_{11}) (*amp*H)……81

Figure 4.28 Thermal conductivity plots for (Sb_7Se_{11}) (*amp*H)……...81

Figure 4.29 PXRD of (Sb_2Se_3) (Sb_3Se_5) (*ba*H) ……82

Figure 4.30 TGA data for (Sb_2Se_3) (Sb_3Se_5) (*ba*H)……83

Figure 4.31 Room temperature absorption spectrum of (Sb_2Se_3) (Sb_3Se_5) (*ba*H)…….84

Figure 4.32 PXRD pattern of Bi_xS_y (*en*) ……...86

Figure 4.33 Room temperature absorption spectra of Bi_xS_y (*en*), Bi_xS_y (*en*) ……86

Figure 4.34 Room temperature absorption spectra of Bi_xSe_y (*en*)……...88

Figure 4.35 PXRD pattern of $Bi_xCu_ySe_z$(*en*) ……89

Figure 4.36 Room temperature absorption spectrum of $Bi_xCu_ySe_z$(*en*) ……89

Figure A1 (a) Integrating Sphere mounted on the fluorescence spectrophotometer, (b) sample holders and their position……98

Figure A2 Linear plots of integrated fluorescence intensity vs absorbance for a standard sample, *trans*-stilbene in hexane and hybrid samples ……100

Figure A3 Observed and calculated PXRD patterns of the double layered (a) 2D-Zn_2S_2(*ba*), (b) 2D-Zn_2S_2(*ha*)……..…102

Figure A4 PXRD patterns of refined 2D-(Zn_2S_2) (*ha*) , 2D-$Zn_{1.7}Cd_{0.3}S_2$(*ha*) , and 2D-$Zn_{1.7}Cd_{0.3}S_2$ (*ha*):0.08%Mn……..102

Figure A5 TGA data for (a) $Zn_{1.7}Cd_{0.3}S_2$ (*ha*), (b) $Zn_{1.7}Cd_{0.3}S_2$ (*oa*), (c) $Zn_{1.7}Cd_{0.3}S_2$ (*ha*):0.08% Mn, and (d) $Zn_{1.7}Cd_{0.3}S_2$ (*oa*):0.08%Mn…….103

Figure A6 CIE coordinates of (a) $Zn_{1.7}Cd_{0.3}S_2$ (*ha*), (b) $Zn_{1.7}Cd_{0.3}S_2$ (*oa*), and (c) $Zn_{1.7}Cd_{0.3}S_2$ (*ha*):0.08% Mn……..104

LIST OF ABBREVIATIONS

en	ethylenediamine
pda	1,3-propanediamine
bda	1,4-butanediamine
ptda	1,5-pentanediamine
hda	1,6- hexanediamine
N_2H_4	hydrazine
pa	*n*-propylamine
ba	*n*-butylamine
ha	*n*-hexylamine
oa	*n*-octylamine
dien	diethylentriamine
amp	N-aminoethylpiperazine
1D	One-dimensional
2D	Two-dimensional
3D	Three-dimensional
CCT	Correlated Color temperature
CIE	International commission on illumination
CRI	Color rendering index
LED	Light emitting diode
PL	Photoluminescence
PLQY	Photoluminescence quantum yield

PXRD	Powder X-ray diffraction
QY	Quantum yield
QCE	Quantum Confinement Effect
SEM	Scanning electron microscope
SSL	Solid state lighting
TGA	Thermogravimetric analysis
WLED	White light emitting diode

CHAPTER ONE

INTRODUCTION

Semiconductors have made a great impact on the modern technology and contributed to many aspects of the human life.[1] They are the vital components of most of the electronic devices such as radio, computers, transistors, solar cells, and different types of diodes. Wide band-gap II-VI and narrow bang-gap V-VI binary compounds are two important classes of semiconductor materials that make a significant impact on our everyday lives. Due to their importance, vast amount of research work has been carried out to study their structures and properties. To develop new and high performance semiconductor materials for the future generation of advanced electronic and optoelectronic devices, one approach is to tailor the optical and electrical properties of these semiconductors by modifying their particle size, shape or chemical composition. Another approach is development of new hybrid inorganic-organic materials with new and unique properties. In this chapter the structure and basic properties and applications of group II-VI and V-VI semiconductors and their hybrid based compounds will be discussed.

1.1 II-VI Semiconductors

Combination of cations of group IIB (Zn, Cd, Hg) and anions of group VIA (O, S, Se and Te) in the periodic table results in the formation of the II-VI semiconductors materials. ZnS, ZnSe, ZnTe, CdS, CdSe, and CdTe are few examples of II-VI materials. They are important components in the electronic and optical technologies and have applications in optoelctronics, light emitting diodes, hetrojunctions diodes, transistors and photovoltaics. Physical properties of these materials can be tailored by simple modifications, such as doping, and varying particle size and shape.[1, 2]

1.1.1 Structure

II-VI semiconductors exist in two main crystal forms, one is the cubic form or zinc blende (ZB, space group *F-43m*) (**Fig. 1.1a**) and another is the hexagonal form or wurtzite (W, space group $P6_3mc$) structure (**Fig. 1.1b**). Both structures are closely related and have very similar atomic arrangements. In both polymorphs, the coordination geometry of both cations and anions are tetrahedral. They only differ in the stacking of anion layers. In the zinc blende structure, the anions are arranged in cubic close-packed arrays and the stacking sequence is repeated every three layers (…*ABC*…) along [111] direction, while in wurtzite, the anions are arranged in hexagonal close-packed arrays and it repeats the stacking sequence every 2 layers (…*AB*…). Both structures are composed of sheets of continuously linked puckered hexagonal rings or honeycomb-like rings in which II and VI group atoms are alternating (**Fig. 1.1c**).[3]

1.1.2 Applications

II-VI semiconductors with a direct band-gap in a range of 1.4-3.6eV (**Table 1.1**) have a wide applications in the transistors, heterojunctions diodes, space charge limited diodes, lasers, optoelectronic devices, photovoltaic devices, photoconductors and solar cells.[1, 2] By changing the physical dimensions of the semiconductor, it is possible to tune the band-gap of the compound and as a result optical, electrical and other properties of semiconductors can be tuned without changing their chemical composition.[1] Doping also can be used to tune several properties such as luminescence or conductivity. Another rapidly growing application of II-V based semiconductor materials is in solid state lighting (SSL).

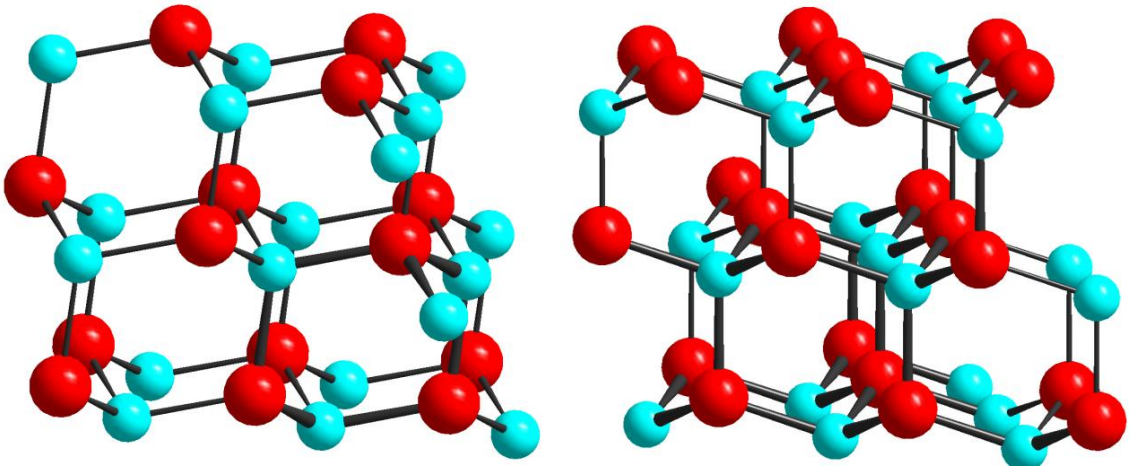

(a) **(b)**

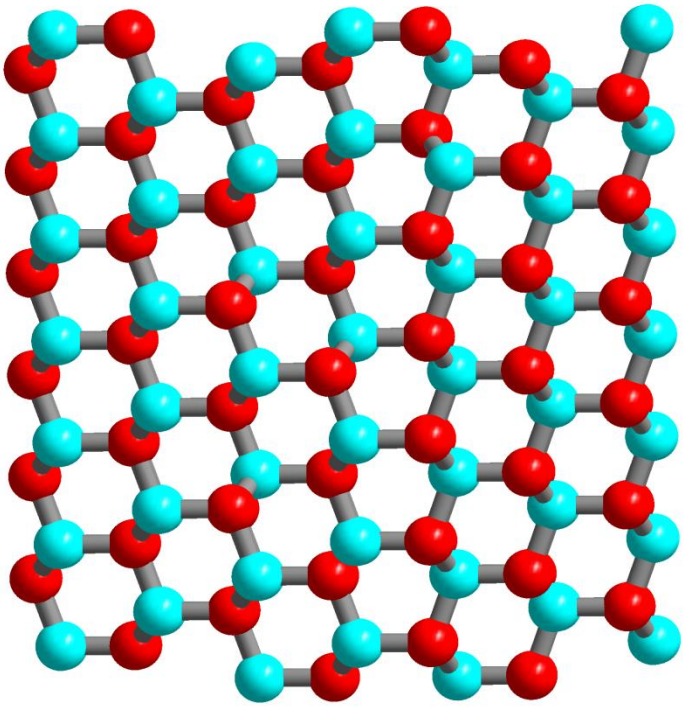

(c)

Figure 1.1 (a) zincblende structure, b) wurtzite structure, (c) honey-comb net view in wurtzite structure.

SSL (primarily light emitting diodes (LED) and organic light emitting diodes (OLED) technology uses semiconducting materials to convert electricity into light. Both LEDs and OLEDs have received considerable attention in recent years due to their enormous potential for utility in lighting and displays.[4] The major advantages of SSL over the current lighting technology are lower energy consumption, higher efficiency, and longer lifetime.[4] SSL is a promising approach for decreasing the energy consumption and reducing CO_2 emission.[4] By using of solid state lighting technology the total electricity consumption for lighting would decrease by roughly 46 percent by the year 2030 in US.[4] Switching to SSL, over the 20 year analysis period, spanning 2012-2030, could potentially have a cumulative energy savings of approximately 2,700 terawatt-hours, representing approximately $250 billion at today's energy prices, and it also reduces the greenhouse gas emissions by 1,800 million metric tons of carbon in US alone.[4]

The white light emitting diodes (WLEDs) are of particular interest because of the great need in general illuminations. Common approaches to produce WLEDs include blending of three primary colored LEDs, namely red, green, and blue (RGB) diodes, or combination of a blue (or UV) LED with a yellow phosphor or multiphosphors.[5-8] The process of color mixing requires complex doping methods and use of the multiple components. In addition, the efficient mixing of colors, maintaining the appropriate amount of each color and color control is a challenging task.[5-7] At the present time, commercially available WLEDs are predominantly phosphor based (a yellow emitting phosphor, yttrium aluminum garnet or (YAG):Ce^{3+}, coupled with a blue emitting InGaN/GaN diode)[5]. While less expensive than the RGB diodes, the (YAG):Ce^{3+} type phosphors and WLEDs have

issues such as inaptness for solution process, poor color rendering index (CRI) and high correlated color temperature (CCT) which limit their widespread commercialization in general lighting applications[5,6c] Semiconductor quantum dots (QDs) or nanocrystals (NCs) with broad and strong absorption and tunable emission are promising candidates for low-cost LEDs because they are solution processable.[9-18] However, their emission bands are often too narrow.[12,15] White light obtained by combining blue-, green-, and red-emitting QDs of various sizes suffers from low efficiency caused by self-absorption, scattering and related energy transfer issues.[9] In addition, size of each component should be very carefully adjusted because emission wavelength changes with particle size.[11,17] It is of great difficulty and complexity to control the size of QDs and maintain an appropriate amount of each component to balance the color. Some other issues which may occur include an irregular dispensation of converter NCs on the LED chip, a lack of consistency in LED performance, and other complex fabrication processes.[11,17] These problems may be reduced or eliminated by developing a) more complex QDs/NCs composites[9] or b) single-phased white-light emitters in bulk form.[7,8] For (a), significantly improved quantum efficiency of 30% for onion-like CdSe/ZnS/CdSe/ZnS,[9a] 15% for InP/ZnS/SiO_2,[9b] 17% for trap-rich CdS,[9a] 17% for Cu:Mn-ZnSe,[16] and 12% for alloyed $Zn_xCd_{1-x}Se$,[11] have been achieved. However, in most cases, multiple steps are involved in the synthesis, and precise control of NC core and/or shell size remains highly challenging. In addition, surface modification is often required which adds further complexity to the synthesis process. For (b), on the other hand, there are only very few known examples of single-phase white-light emitters in the bulk form.[7, 8, 11] One of them is [{AgL}$_n$·nH2O] (L=4-cyanobenzoate), for which a quantum yield (QY) of 10.9% is achived.[7c] Additionally, several single-phase

organic white-light-emitting materials with low quantum efficiency have been developed.[7] In this thesis it has been shown that crystalline structures, built on periodically arranged two-dimensional (2D) nano-modules of ZnS and organic amines are capable of generating white light upon illumination with UV LED.[18c,d] These new solution-processable, low-cost, and high-efficiency hybrid semiconductor bulk materials can be used as single-phase white-light-emitting phosphors. Having a white light emission QY as high as 37%, the new phosphors are approaching the performance of commercially available (YAG):Ce^{3+}.

Table 1.1 Room temperature band-gaps (Eg) of some II-VI compounds[2]

	Band-gap (eV)		**Band-gap (eV)**
ZnS	3.54-3.67	**CdS**	2.50
ZnSe	2.58	**CdSe**	1.74
ZnTe	2.26	**CdTe**	1.44-1.5

1.2 II-VI based hybrid semiconductors

Inorganic-organic hybrid semiconductor materials have received enormous attention because of their interesting, enhanced and unique properties that may not be possible in either of the components alone. Inorganic materials have high carrier mobility and offer superior electrical, optical, magnetic and thermal properties while the organic component offers flexibility and high processibility. In addition they are structurally diverse and cost effective. They have great potentials for applications in optoelectronic devices, such as transistors, light emitting diode (LED) and solar cells. A new class of inorganic–organic hybrid semiconductor bulk materials with a general formula of $M_nQ_n(L)_x$ (M = Mn, Zn,

Cd; Q = S, Se, Te; L= mono- or di-amine; n = 1 and 2; x = 0.5 and 1) has been developed. These crystalline compounds are extended networks of one-, two- and three dimensions and are composed of alternating II–VI binary semiconductor (inorganic) modules and amine molecules (organic) at nano- or sub-nanometer scale and in periodic arrangement by coordinate bonds. They exhibit interesting and enhanced structural, optical, thermal, and mechanical properties.[19]

1.2.1 Structure

Incorporating organic amine layers between the chains and slabs of II-IV semiconductors resulted in a new class of inorganic-organic hybrid nanostructures. These hybrid materials are composed of alternating inorganic and organic modules (at nanometer or subnanometer scale) in periodic and uniform arrangement. The layers are connected to each other via coordinate bonds and they possess perfectly ordered structures (**Fig 1.2a-d**). Inorganic slab may be regarded as a slice from the zincblende or wurtzite structure of II-VI semiconductor. It is the honeycomb net of alternating, three-coordinated metal (Zn/Cd) and chalcogen (S, Se, and Te) (**Fig. 1.3a**). Nitrogen of the amine molecules bonds to metal (Zn or Cd) via its lone pair of electrons to complete the tetrahedral coordination of the metal and this way amine molecules bridge to two Zn or Cd metal centers from the adjacent slabs. The length of amine molecules can be modified to manipulate the mechanical, luminescence or thermal expansion properties of these hybrids (Fig. 1.2a-d). It is also possible to change the thickness of the inorganic layer, and change the dimensionality from one-dimension (1D) to two-dimension (2D), and three-dimension (3D) (**Fig. 1.3b-e**).

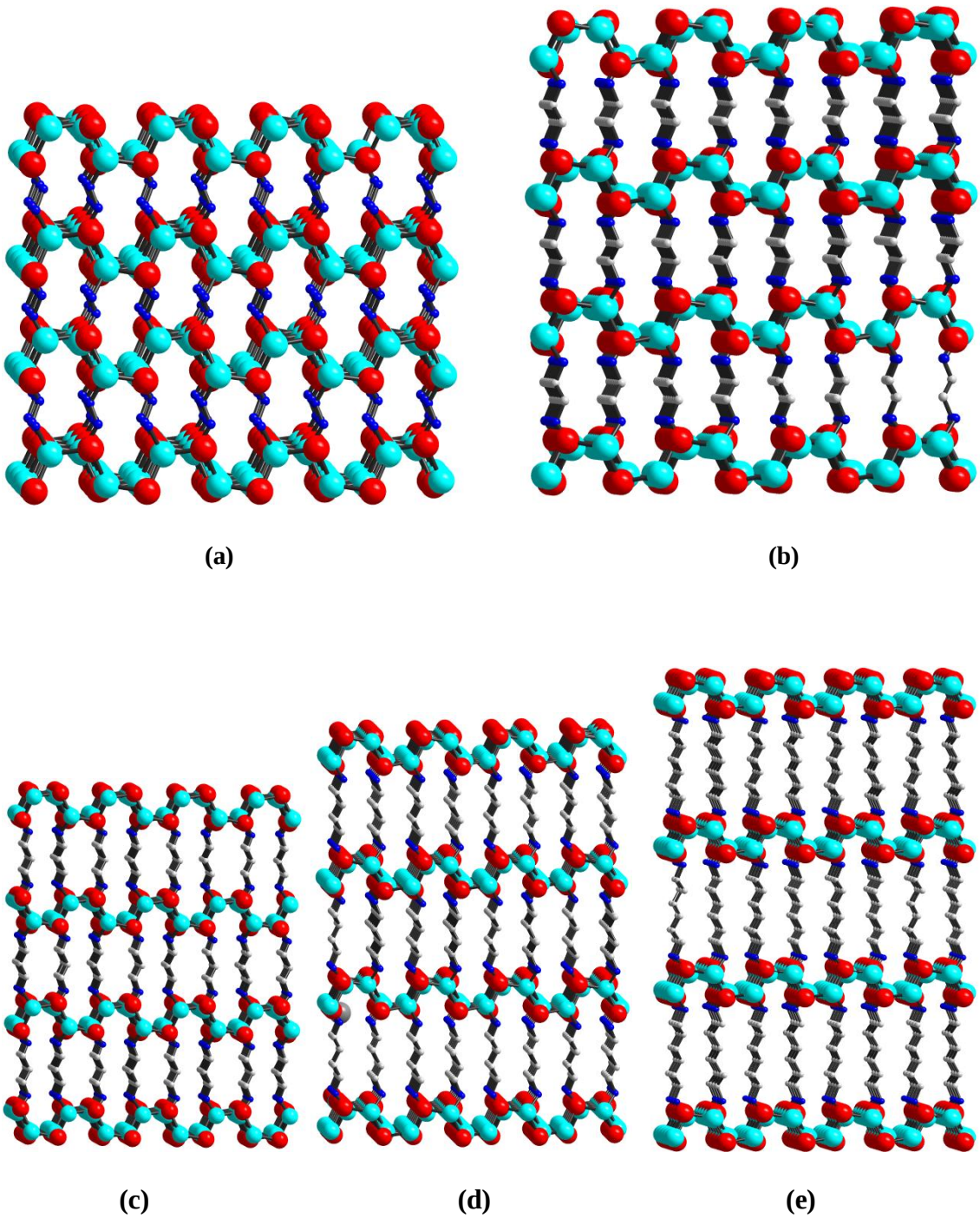

Figure 1.2 View of single layer 3D-MQ(L)$_{0.5}$-type hybrid structure (M=Zn, Cd; Q=S, Se, Te; L = *diamine*), (a) ZnTe(*hydrazine*)$_{0.5}$, (b) ZnTe(*en*)$_{0.5}$, (c) ZnTe(*pda*)$_{0.5}$, (d) ZnTe(*bda*)$_{0.5,}$ (e) ZnTe(*hda*)$_{0.5}$**.** M: red, Q: cyan, N: blue, C: grey. Hydrogen atoms are omitted for clarify.

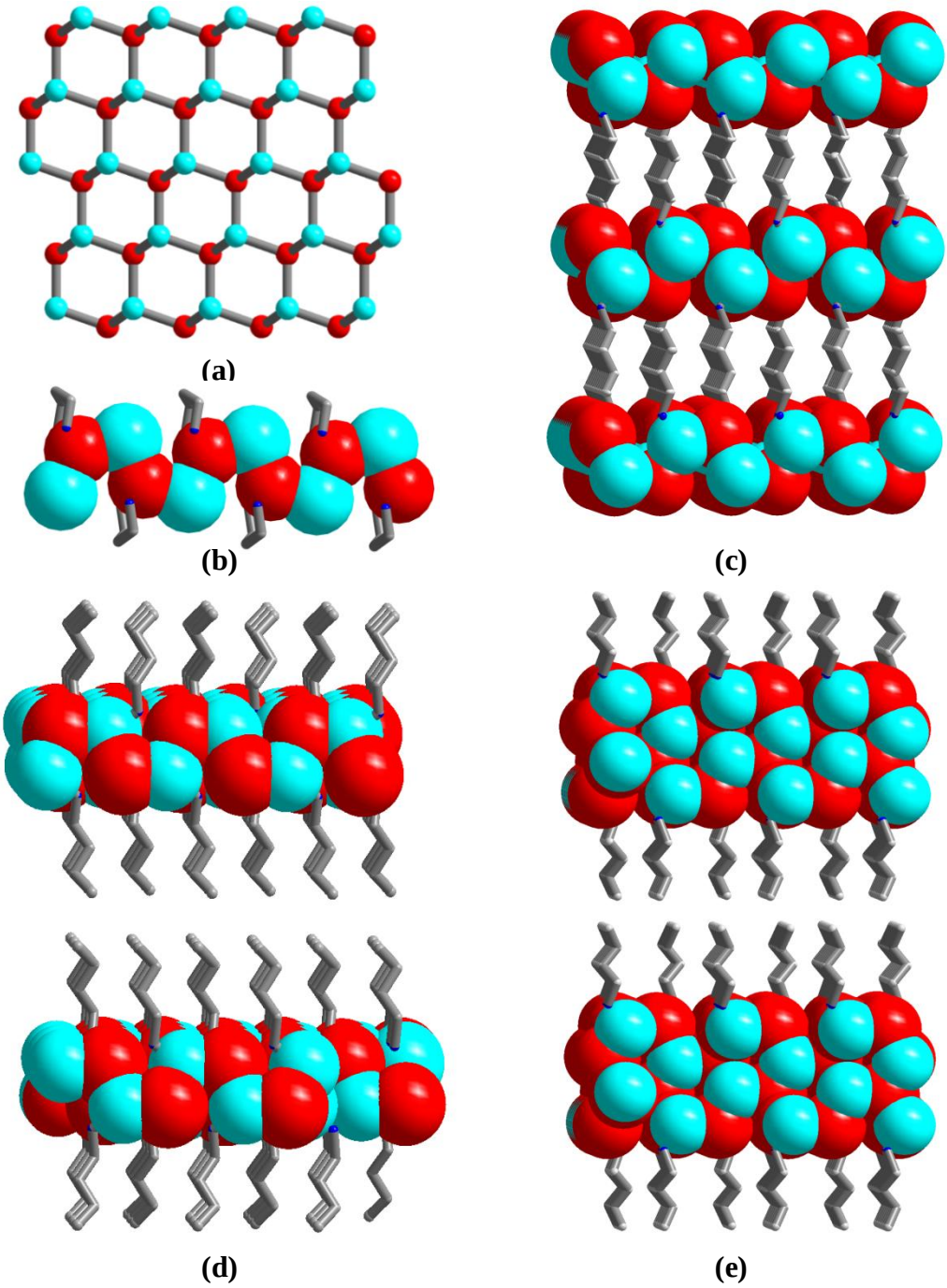

Figure 1.3 View of (a) single layer of honeycomb-like net of II-VI in the $M_nQ_n(L)_x$-type hybrid structure (M = Zn, Cd; Q = S, Se, Te; *L*= monoor diamine), (b) single-chain 1D-MQ(*L*) structure, (c) single layer 3D-MQ$(L)_{0.5}$ structure, d) single-layer 2D-MQ(*L*) structure, and (e) double-layer 2D-$M_2Q_2(L)$ structure. Blue M, red Q, in (b)–(d) the stick model corresponds to *L*.

1.2.2 Properties

II-VI based hybrids with a general formula of $M_nQ_n(L)_x$ (M = Zn, Cd, Q= S, Se, Te, L = mono- and di-amine) exhibit strong structure-induced quantum confinement effect (QCE), and thus, large blue shift in their optical band gap.[19] Their absorption spectra show a sharp band edge absorption, and high absorption coefficient. Band gap tunability by means of changing the thickness of the inorganic layer, reduced and tailorable thermal expansion, improved flexibility, lower thermal conductivity, and white light emission are among the numerous interesting and unique characteristics of this group of compounds.

1.3 V-VI Semiconductors

Group V-VI binary compounds are among the best semiconductors available today. Because of their well known high conductivity, good thermoelectric properties, switching effects and excellent photovoltaic power.[20-23] They form from the combination of cations of group VA (Sb, Bi) and anions of group VIA (O, S, Se, Te) in the periodic table. Sb_2Te_3, Bi_2Te_3, Bi_2S_3, and Sb_2Se_3 are few examples of the V-VI semiconductors.

1.3.1 Structure

Bismuth and antimony chalcogenide binary compounds have layered structures, and are highly anisotropic. Structure of Bismuth selenide and bismuth telluride as well as that of the antimony telluride consists of the five layers slabs in a sequence of Q-Bi-Q-Bi-Q where Q is Se or Te. Several phases of Bismuth selenide and Bismuth telluride have been known.[21] Within the slabs, Bi and Sb have octahedral coordination. The bonding

interaction between the layers in each slab is covalent while the interaction between the slabs is Van der Waals type and weaker in nature. Bi_2Se_3 and Bi_2Te_3crystallize in a rhombohedral structure with space group *R-3m*.[20, 21] (**Fig. 1.4a**). The crystal structure of Bi_2S_3 is different from that of the bismuth selenide and telluride; it crystallizes in *B2mm* or *Pbnm* space group (**Fig. 1.4b**). Sb_2S_3 and Sb_2Se_3 crystallize in an orthorhombic space group *Pbnm* (**Fig. 1.4c**). Monoclinic space group of *C2/c* has also observed for Sb_2S_3 (**Fig. 1.4d**).

1.3.2 Properties

Group V-VI binary compounds and their derivatives are by far the best known materials for applications in thermoelectric devices (**Table 1.2**). Sb_2Te_3 and Bi_2Te_3 are recognized for their high thermoelectric power. Bismuth telluride is not only one of the best available semiconductors with high electrical conductivity, but also the most important thermoelectric (TE) material near the room temperature.[20-22]

Concept of thermoelectric was defined after the discovery of Seebeck (1821), Peltier (1834) and Thommson (1854) effects. Few years later, figure of merit (ZT) was introduced to evaluate the efficiency of thermoelectric materials. Figure of merit is formulated as $ZT = T\alpha^2\sigma/\kappa$, where T is the absolute temperature, α is the Seebeck coefficient, σ is the electrical conductivity and κ is the thermal conductivity. Base on this concept, good thermoelectric materials are the ones with high electrical conductivity, high Seebeck coefficient and low thermal conductivity.[23]

Today, research on thermoelectric device fabrication is motivated by two main factors, power generation and refrigeration. Thermoelectric device have applications in air conditioning, and spot cooling of electronic chip, thermal suits for fire-fighting, and

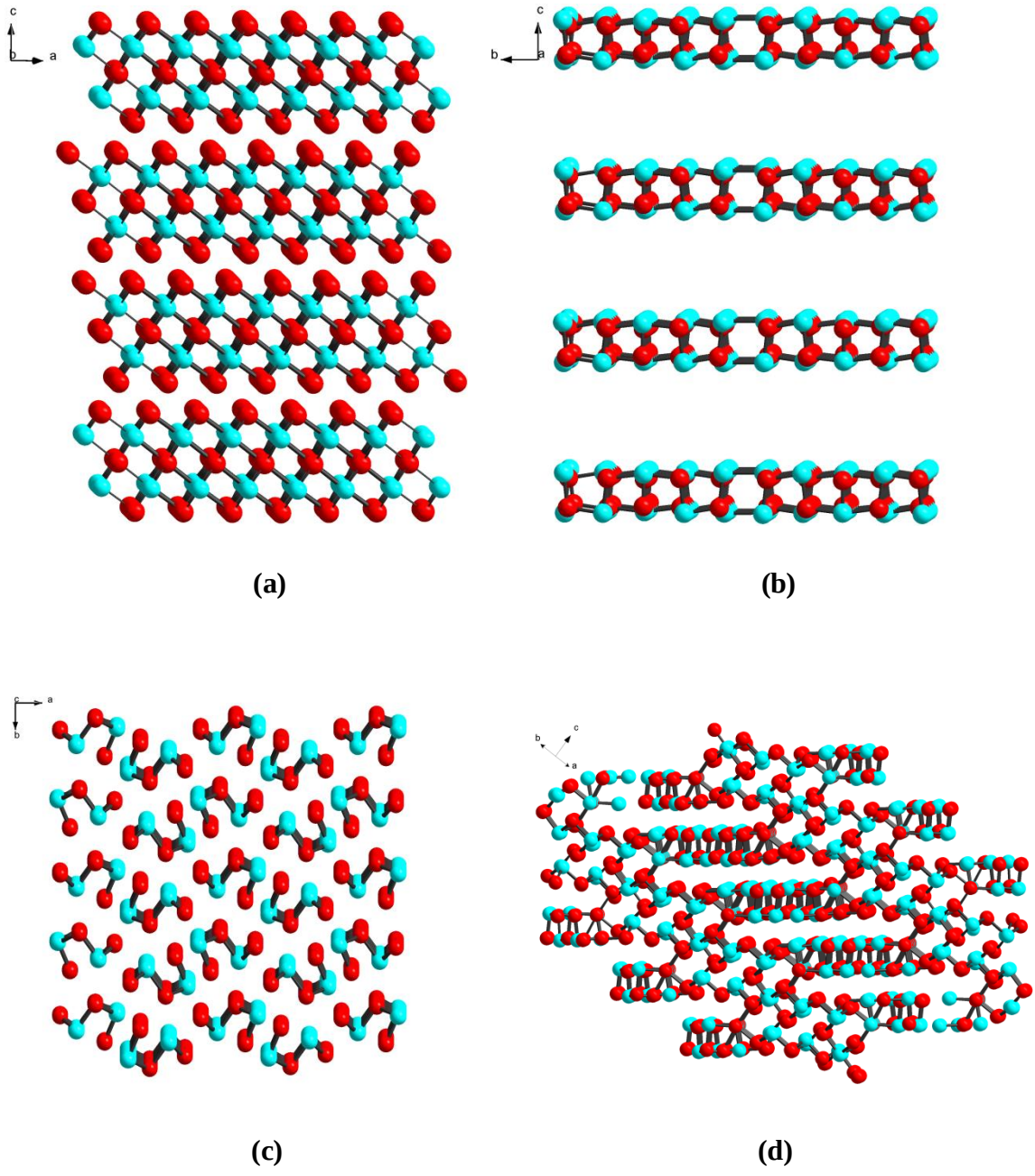

Figure 1.4 View of the structure of (a) rhombohedral, Bi_2Te_3 with a space group *R-3m* (b) Bi_2S_3, with *B2mm* (d) Sb_2Se_3 with *Pbnm,* and (d) Sb_2S_3 with *C2/c* space group. Sb and Bi atoms are shown in cyan and chalcogens in red.

geothermal power generation. They can be used in Space shuttles and rockets for compact source of power. In addition they have application in waste heat recovery and can be used for in automobile engines for energy recovery.[23] Years of studies have showed that the best thermoelectric candidates are the narrow band-gap semiconductors, heavy elements, materials with high mobility and low thermal conductivity. Compounds which are highly anisotropic or highly symmetric with a large unit cell and complex compositions and structures are among the promising choices.[23]

Beside their application in thermoelectric cooling modulus, these materials are promising for other applications in optical and photoelectrochemical devices, as well as solar cells. Semiconductors such as Sb_2S_3 and Bi_2S_3 with the direct band gap of 1.7-2.2 eV [24] and 1.3-1.7 eV respectively,[24, 25] are good candidates for use as an absorber layer in the semiconductor-sensitized solar cell or in thin film photovoltaic device.[20, 25] Sb_2Se_3 with the band-gap of 1.13-1.15 eV have received much attention due to its switching effects, thermoelectric and photovoltaics properties and applications in TV, cameras, interference filters and different photonic and optoelectronic devices.[20]

1.4 V-VI based hybrid semiconductors

Developing new types of layered metal chalcogenides is important for different applications where a particular property is required. Hybrid inorganic-organic compounds show unique properties that are not achievable in any of the component alone. Due to the stereochemically active lone pair of Sb^{III}, Sb can have variable coordination number and as a result a rich structural diversity is observed for thio- and selenoantimonates. Using amines as a solvent has led to a wide variety of hybrid compounds with diverse structures.

While there are many reports on solvothermal synthesis of thioantimonates hybrids,[26, 27] the selenosntimonates are less explored. Some reported structures include, $[M(dien)_2]_2Sb_4Se_9$ (M: Mn, Fe), $[Co(dien)_2]_2Sb_2Se_6$, and $[Ni(dien)_2]_2Sb_2Se_5$,[28a] $Cu_2SbSe_3.0.5en$ and $Cu_2SbSe_3.en$,[28b] $[Fe(en)_3]_2(Sb_2Se_5)$,[28c] $[La(trien)_2(H_2O)]SbSe_4$ $[Eu(en)_2(dien)(SbSe_4)]$ (IIa), $[Eu(en)(trien)(\eta_2\text{-}SbSe_4)]$ (IIb), and $[Eu(dien)_2(\eta 2\text{-}SbSe_4)]$,[28d] $[Ln(en)_4(SbSe_4)]$ (Ln = La, Nd) and $[Sm(en)_4]SbSe_4 \cdot 0.5en$,[28e] $[Ge(en)_3][enH][SbSe_4]$.[29] In most of these solvothermaly prepared compounds the primary building unit is SbQ_3 (Q = S, Se) trigonal pyramids. Secondary building units such as Sb_2Q_5 and Sb_2Q_5 are formed by corner sharing or edge sharing of the primary units. The final structures, such as discrete anions, chains, 2D-layers or 3D-structures are the result of the connection of the primary and secondary units. Transition or rare earth metals are usually introduced into the reaction to obtain a compound with specific and desired property. These transitions metals usually form a complex with the amine and can act as a structure directing agents or charge compensating cations and lie in channels or between the layers of anionic frameworks. Incorporation of these metal ions with strong coordination to solvent molecules would result in a molecular or low dimensional, such as chain structures. An example of these chalcogenidometalates is $[Fe\ (en)_3]_2(Sb_2Se_5)$[28c]. On the other hand, metal ions of group 13-15 usually directly bind to the chalcogen because they don't have much tendency to form a cation complex with solvent. They usually form the intercalated layer structures, in which layers of the inorganic network are separated by organic molecules, with a very small or no interactions between the layers. Examples of this type of structures are $Cu_2SbSe_3.0.5en$ and $Cu_2SbSe_3.en$.[28b] In contrast to wide variety of known thio-and seleno-anotimonates, hybrid compounds of

antimony telluride have not been discovered and the sole reported hybrid structures based on bismuth chalcogenide is $[NEt_4][BiSe_2]$.[29]

Table 1.2 Summary of thermoelectric figure of merit (ZT) value for selected chalcogenide compounds

Compound	ZT (K^{-1})	Temperature (K)	Ref.
$Bi_2(Te_{1-x}.Se_x)_3$	1.2	Room T	22a
$CsBi_4Te_6$	0.8	225	22b
$Ag_{0.8}Pb_{22}SbTe_{20}$	1.37	673	22c
$Ag_{0.8}Pb_{22.5}SbTe_{20}$	1.5	700	22d
TI_9BiTe_6	0.89	580	22e
TI_5SnTe_5	1	500	22f,23
$PbBi_4Te_7$	0.5	700	22g,23
Ag_9TITe_5	1.23	700	22h,23
$Na_{0.95}Pb_{20}SbTe_{22}$	1 1.7	475 700	22i, 23
$La_{0.2}Bi_{1.8}Te_3$	0.58	480	22j, 23
$Mo_3Sb_{5.4}Te_{1.6}$	0.8	1000	22k,l, 23

1.5 Solvothermal synthesis

Solvothermal method has been widely used for synthesis of purposes and crystal growth of metal carbonates, phosphates, oxides and halide.[30] Solvothermal method is simple and cost effective. It does not require any organometallic or toxic precursors and synthesis can be done at relatively low temperatures. In a typical solvothermal reaction, reactants and solvent are loaded in a Teflon lined autoclave or in another closed system such as glass ampoule. Sealed reaction is heated at temperatures above the solvent boiling point. Autogeneous pressure developing in the autoclave would change the solubility of the

reactants. Under these conditions, solubility and reactivity of reactants are usually enhanced because some properties of solvents such as density, viscosity and diffusion coefficient are different from ambient conditions. As the solubility increases, reaction can take place at lower temperatures and under the milder condition compare to the usual synthetic method.[30, 31]

Amines are among the common solvents in solvothermal synthesis. They can also act as structure directing agents and can be used as organic templates. In some cases they can also serve as reagent and be incorporated in the inorganic frameworks or intercalate between the layers.[19, 26-28, 32] To make the inorganic-organic hybrids, metal chlorides or metal nitrates can be used as a source of metal ions and elemental sulfur, selenium and tellurium as chalogens. Aliphatic amines such as butylamine(*ba*), hexylamine(*ha*) octyleamine(*oa*), ehtylenediamine(*en*), 1,3-propanediamine(*pda*), 1,4-butyldiamine(*bda*), 1-6, hexanediamine(*hda*), and diethylentriamnes(*dien*) can act both as a solvent and a reactant. To design different structures of organic-inorganic hybrid with different dimensionality it is possible to use different organic ligands, i.e mono- and bi-functional organic spacers. These ligands can function as a capping agent to control the dimensionality of the structure and also they can act as bridging ligands. One-dimensional chain, two-dimensional layers or three-dimensional network structures can be designed using the proper ligands. Organic ligands with different length can also be used and their effect on properties of the synthesized materials can be studied. Bi-functional spacers can bridge the chains or layers while use of mono-functional spacer result in chains or layers which are not interconnected and exist in isolated forms. Ligands containing unsaturated bonds or aromatic rings such as aminopyridyne may be capable in charge transfer between

organic and inorganic layers and can be used by dissolution in water or solvents such as DMF. Final products and their structures are also greatly affected by the reaction temperature and time, the ratio between metal and ligand, and the amount of solvent used in the starting reactions.[19d]

In this dissertation, we discuss, synthesis, structure and properties of the II-VI and the V-VI based hybrid compounds and their applications. Chapter 2 goes over the structures and optical properties of 2D-double layer hybrids with a general formula of $M_2S_2(L)$ where M is Zn or Cd and *L* is organic amine. Effect of doping, composition, and length of amine on the band-gap, optical emission range and intensity, quantum yield, and color quality will be discussed in details. Possible applications of this hybrid system and its advantages as promising candidates for use in white light emitting diodes (WLEDs) are also discussed in this chapter. In chapter 3, mechanical properties of 3D-single layer II-VI based hybrid compounds will be presented. The effect of organic amine's chain length on the flexibility of the hybrids is analyzed. In the last chapter, chapter 4, discussions are focused on synthesis, structure and properties of a new V-VI based hybrids. It reports the crystal structure analysis, optical, electrical and thermal conductivity of several new hybrid structures containing one-dimensional chains or two-dimensional layers of V-VI motifs.

1.6 References

1. a) S.M. Sze, *Semiconductor Devices: Physics and Technology*, 2nd Ed., Wiley, **2001**; b) K.K. Ng, *Complete Guide to Semiconductor Devices*, 2nd Ed., Wiley-IEEE Press, **2002**; c) J. Singh, *Semiconductor Optoelectronics: Physics and Technology*, McGraw-Hill: New York, **1995**; d) I.P. McClean, C.B. Thomas, *Semicond. Sci. Technol*. **1992**, *7*, 1394; e) H. Yang, S. Santra, P.H. Holloway, *J. Nanosci. & Nanotech.* **2005**, *5*, 1364; f) A.P. Alivisatos, *Science* **1996**, *271*, 933; g) S. Kumar, T. Nann, *Small* **2006**, *2*, 316.

2. a) *Handbook of Chemistry and Physics*, 86 edition, CRC Press, **2005-2006**; b) J. *Physics of Semiconductors and Their Heterostructures*, McGraw-Hill, **1993**.

3. A.B. Chen, A. Sher, *Semiconductor Alloys: Physics and Materials Engineering*, Plenum press, New York, **1995**.

4. a) *Worldwide Trends in Energy Use and Efficiency;* International Energy Agency: Paris, France 2008; b) *Solid-State Lighting* http://ssls.sandia.gov/; c) U.S. department of energy http://www1.eere.energy.gov/buildings/ssl/; d) U.S. Department of Energy, "*Energy Savings Potential of Solid-State Lighting in General Illumination Applications",* Prepared for: Solid-State Lighting Program, January **2012**; e) U.S. Energy Information Administration, www.eia.gov; f) U.S. Energy Information Administration, *Annual Energy Review*, **2012**.

5. a) N. Guo, Y.J. Huang, H.P.You, M. Yang, Y.H. Song, K.Liu, Y. H. Zheng, *Inorg. Chem.* **2010**, *49*, 10907; b) L. Chen, K.-J. Chen, S.-F. Hu, R.-S. Liu, *J. Mater. Chem.* **2011**, *21*, 3677; c) L. T. Su, A. I. Y. Tok, Y. Zhao, N. Ng, F. Y. C. Boey, J. L. Woodhead, C. J. Summers, *J. Phys Chem. B* **2008**, *112*, 10830; d) V. Bachmann,C. Ronda,A. Meijerink, *Chem. Mater.* **2009,** *21*, 2077; e) R. J. Xie, N. Hirosaki, M. Mitomo, K. Takahashi, K. Sakuma, *Appl. Phys. Lett.* **2006**, *88*, 101104; f) H. S. Jang, W. B. Im, D. C. Lee, D. Y. Jeon, S. S. Kim, *J. Lumin.* **2007**,*126*, 371.

6. a) P. O. Anikeeva, J. E. Halpert, M.G. Bawendi, V. Bulovic, *Nano. Lett* **2007**, 7(8), 2196; b) Y. Li, A. Rizzo, R.Cingolani, G. Gigli, *Adv. Mater.* **2006**, *18*, 2545; c) S. Nizamoglu, G. Zengin, H. V. Demir, *Applied Physics Letters* **2008**, *92*, 031102.

7. a) X-H. Zhu, J. Peng, Y. Cao, J. Roncali, *Chem. Soc. Rev*. **2011**, *40*, 3509; b) R. M. Adhikari, L. Duan, L. Hou, Y. Qiu, D. C. Neckers, B. K. Shah, *Chem. Mater.* **2009**, *21*, 4638; c) Y. Liu, M. Nishiura, Y. Wang, Z. Hou, *J. Am. Chem. Soc.* **2006**, *128*, 5592.

8. M. S. Wang, S. P. Guo, Y. Li, L. Z. Cai, J. P. Zou, G. Xu, W. W. Zhou, F. K. Zheng, G. C. Guo, *J. Am. Chem. Soc.* **2009**, *131*, 13572.

9. a) S. Sapra, S. Mayilo, T. A. Klar, A. L. Rogach, J. Feldmann, *Adv. Mater.* **2007**, *19*, 569; b) J. Ziegler, S. Xu, E. Kucur, F. Meister, M.Batentschuk, F. Gindele, T. Nann. *Adv. Mater.* **2008**, *20*, 4068.

10. a) M. J. Bowers II, J. R. McBride, S. J. Rosenthal, *J. Am. Chem. Soc.* **2005**, *127*, 15378; b) M. J. Bowers II, J. R. McBride, M. D. Garrett, J. A. Sammons, A. D. Dukes, M. A. Schreuder, T. L. Watt, A. R. Lupini, S. J. Pennycook, S. J. Rosenthal, *J. Am. Chem. Soc.* **2009**, *131*, 5730; c) M. A. Schreuder, J. D. Gosnell, N. J. Smith, M. R. Warnement, S. M. Weiss, S. J. Rosenthal, *J. Mater. Chem.* **2008**, *18*, 970; d) M. A. Schreuder, J. R. McBride, A. Dukes, J. A. Sammons, S. J. Rosenthal, *J. Phys. Chem. C* **2009**, *113*, 8169; e) A. Nag, D. D. Sarma, *J. Phys. Chem. C* **2007**, *111*, 13641.

11. a) C. C. Shen, W. L. Tseng, *Inorg. Chem.* **2009**, *48*, 8689; b) B. H. Kwon, H.S. Jang, H. S. Yoo, S.W. Kim, D.S. Kang, S. Maeng, D.S. Jang, H. Kim, D.Y Jeon, *J. Mater. Chem*. **2011**, 21, 12812; c) E. Jang, S. Jun, H. Jang, J. Lim, B. Kim and Y. Kim, *Adv. Mater.* **2010**, *22*, 3076.

12. M. A. Schreuder, K. Xiao, I. N. Ivanov, S. M. Weiss, S. J. Rosenthal, *Nano Lett.* **2010**, *10*, 573.

13. Y. Zhang, C. A. Xie, H. P. Su, J. Liu, S. Pickering, Y. Q. Wang, W.W. Yu, J. K. Wang, Y. D. Wang, J. I. Hahm, N. Dellas, S. E. Mohney, J. A. Xu, *Nano Lett.* **2011**, *11*, 329.

14. H. Z. Sun, H. Zhang, J. H. Zhang, H. T. Wei, J. Ju, M. J. Li, B. Yang, *J. Mater. Chem.* **2009**, *19*, 6740.

15. H. S. Chen, S. J. J. Wang, C. J. Lo, J. Y. Chi, *Appl. Phys. Lett.* **2005**, *86*, 131905.

16. S. K. Panda, S. G. Hickey, H. V. Demir, A. Eychm-ller, *Angew. Chem. Int. ed.* **2011**, *50*,4432.

17. L. Qian, D. Bera, P.H. Jolloway, *Nanotechnology* **2008**, *19*, 285702.

18. a) W. Ki, J. Li, *J. Am. Chem. Soc.* **2008**, *130*, 8114 – 8115; b)W. Ki, J. Li, G. Eda, M. Chhowalla, *J. Mater. Chem.* **2010**, *20*, 10676; c) M. Roushan, X. Zhang, J.Li, *Angew. Chem. Int. Ed.* **2012**, *51*, 436; d) X. Fang, M. Roushan, R. Zhang, J. Peng, H. Zeng, J. Li, *Chem. Mater.* **2012**, *24* (10), 1710.

19. a) X. Y. Huang, J. Li, *J. Am. Chem. Soc.* **2007**, *129*, 3157; b) X. Y. Huang, H. R. Heulings, V. Le, J. Li, *Chem. Mater.* **2001**, *13*, 3754; c) X. Y. Huang, J. Li, H. X. Fu, *J. Am. Chem. Soc.* **2000**, *122*, 8789; d) X. Y. Huang, J. Li, Y. Zhang, A. Mascarenhas, *J. Am. Chem. Soc.* **2003**, *125*, 7049; e) X. Y. Huang, M. Roushan, T. J. Emge, W. H. Bi, S. Thiagarajan, J. H. Cheng, R. G. Yang, J. Li, *Angew. Chem. Int. Ed*. **2009**, *48*, 7871.

20. a) K.Y. Rajpure, C.H. Bhosale, *Materials Chem. and Phys.* **2002**, *73*, 6; b) K.Y Rajpure, C.D Lokhande, C.H Bhosale, *Thin solid films*, **1997**, *311*, 114; c) N.S. Platakis, H.C. Gatos, *Phys. Status Solidi A* **1972**, *13*, K1; d) P**.** Arun, A. G. Vedeshwar, N. C. Mehra, *J. Phys. D: Appl. Phys.* **1999**, *32*, 183; e) A.M. Fernández, M.G Merino, *Thin Solid Films*, **2000**,*366*, 202; f) Y. Yu, R.H. Wang, Q. Chen, L.M. Peng, *J. Phys. Chem B* **2006**, *110*, 13415; g) S. Messina, M.T.S. Nair, P.K. Nair, *Thin Solid Films* **2007**, *515*, 5777; h) F.J. DiSalvo, *Science* **1999**, *285*, 703; i) D.M. Rowe, *Handbook of Thermoelectroics*, CRC Press, Boca Raton, FL, **1995**; j) B. Poudel, Q. Hao, Y. Ma,Y. Lan, A. Minnich, B. Yu, X. D. Wang, A.Muto, D. Vashaee, X. Chen, J. Liu, M. S. Dresselhaus, G. Chen, Z. Ren, *Science* **2008**, *320*, 634.

21. a) H. Lind, S. Lidin, U. Häussermann, *Physical Review B* **2005**, *72*, 184101; b) N.W. Tideswell, F.H. Kruse, J.D. McCullough, Acta Cryst. **1957**, *10*, 99; c) A. Kyono, M. Kimata M, Matsuhisa, Y. Miyashita, K. Okamoto, *Phys Chem. Miner.* **2002**, *29(4)*, 254; d) P. Bayliss, W. Nowacki, Z Kristallogr. **1972**, *135*, 308; e) L. F. Lundegaard. E. Makovicky T. Boffa-Ballaran, T. Balic-Zunic, *Phys. Chem. Minerals* **2005**, *32*,578.

22. a) D.Y. Chung, T. Hogan, P. Brazis, M. Rocci-Lane, C. Kannewurf, M. Bastea, C. Uher, M.G. Kanatzidis, *Science* **2000**, *287***,** 597; b) H. Wang, J.F. Li, C.W. Nan, M. Zhou, W.S. Liu, B.P. Zhang, T. Kita, *Appl. Phys. Lett.* **2006**, *88*, 092104; c) M. Zhou, J.F. Li, T. Kita, *J. Am. Chem. Soc.* **2008**, *130 (13)*, 4527; d) S. Yamanaka, A. Kosuga, K. Kurosaki, *J. Alloys and Compounds* **2003**, *352*, 275; e) J.W. Sharp, B.C. Sales, D.G. Mandrus, *Appl. Phys. Lett.* **1999**, *74*, 3794; f) L.A. Kuznetsova, V.L. Kuznestov, D.M. Rowe, *J. Phys. Chem. Solids* **2000, *61*,** 1269; g) K. Kurosaki, A. Kosuga, H. Muta, M. Uno, S. Yamanaka, *Appl. Phys. Lett.* **2005**, *87***,** 1; h) P.F. P. Poudeu, J. D'Angelo, A. D. Downey, J. L. Short, T.P. Hogan, M.G. Kanatzidis, *JACS* **2006**, *128*, 14347; i) Y.H. Zhang, T.J. Zhu, J.P. Tu, Z.B. Zhao, *Mater. Chem. Phys.* **2007**, *103*, 484; j) E. Dashav, A. Szczepenowska, H. Klenke, H. *J. Mater. Chem.* **2002**, *12*, 345; k) W.U. Huynh, J.J. Dittmer, A.P. Alivisatos, *Science* **2002**, *295***,** 2425; l) A.P. Alivisatos, *Science **1996**, 271(5251)*, 933.

23. a) T.J. Seebeck, *Proc. Prussian Acad. Sci*. **1822**, 265; b) E. Altenkirch, *Phys. Zeitschrift* **1909**, *10*, 560; c) E. Altenkirch, *Phys. Zeitschrift* **1911**, *12***,** 1920; d) D.G. Walker, A. Bulusu, *Supper Lattices and Microstructures* **2008**, *44*, 1; e) A.V. Shevelkov, *Russian Chemical Reviews* **2008**, *77*, 1.

24. a) Y. Itzhaik, O. Niitsoo, M. Page, G. Hodes, G. *J. Phys. Chem. C* **2009**, *113*, 4254; b) Y.R. Lazcano, Y. Pena, M.T.S. Nair, P.K. Nair, *Thin Solid Films* **2005**, *493*, 77; c) Z.R. Geng, M.X. Wang, G.H. Yue, P.X. Yan. *J. Crystal Growth* **2008**, *310*, 341.

25. a) L.M. Peter, K.G.U. Wijiayantha, D.J. Riley, J.P. Waggett, *J. Phys. Chem. B.* **2003**, *107*, 8378; b) M.W. Shao, M.S. Mo, Y. Cui, Y. Chen, Y.T. Qian, *J. Crystal Growth* **2001**, *233*, 799.

26. a) B. Seidlhofer, V. Spetzler, C. Näther, W. Bensch, *J. Solid State Chem.* **2012**, *187*, 269; b) A.V. Powell, J. Thun, A. M. Chippindale, *J. Solid State Chem.* **2005**, *178*, 3414; c) V. Spetzler, C. Näther, W. Bensch, *J. Solid State. Chem.* **2006**, *179*, 3541; d) M. L. Feng, Z. L. Xie, X.Y. Huang, *Inorg. Chem.* **2009**, *48*, 3904; e) H. Lühmann, Z. Rejai, K. Möller, P. Leisner, M. E. Ordolff, C. Näther, W. Bensch, *Z. Anorg. Allg. Chem*. **2008**, 634, 1687;

27. a) Z. Rejai, H. Lühmann, C. Näther, R. K. Kremer, W. Bensch, *Inorg chem.* **2010**, *49*, 1651; b) A. V. Powell, S. Boissière, A .M. Chippindale, *J. chem. Soc. Dalton, trans.* **2000**, 4192; c) M. Zhang, T. L. Sheng, X. H. Huang, R. B. Fu, X. Wang, S. M. Hu, S.C. Xiang, X. T. Wu, *Eur. J. Inorg. Chem.* **2007**, *2007*, 1606; d) L. Engelke, C. Näther, W. Bensch, *Eur. J. Inorg. Chem*, **2002**, *2002*, 2936; e) J. L. Mertz, N. Ding, M. G. Kanatzidis, *Inorg chem*. **2009**, *48*, 10898; f) J. Zhou, X. H Yin, F. Zhang, *Inorg.Chem.* **2010**, *49*, 9671.

28. a) D. Jia, Y. Zhang, Q. Zhao, J. Deng. *Inorg. Chem.* **2006**, *45*, 9812; b) Z. Chen, R. E. Dilks, R. J.Wang, J. Y. Lu, J. Li, *chem. Mater.* **1998**, *10*, 3184; c) Z. Chen, R.J. Wang, X.Y. Huang, J. Li, *Acta Cryst.* **2000**, *C56*, 1100; d) D. X. Jia, Q. Jin, J. Chen, Y. Pan, Y. Zhang, *Inorg Chem.* **2009**, *48*, 8286; e) D. X. Jia, Q. X. Zhao, Y. Zhang, J. Dai, J. Zhou, *Eur. J. Inorg. Chem.* **2006**, *37*, 2760.

29. M. A. Pell, J. A. Ibers, *Inorg. Chem* **1996**, *35(16)*, 4559.

30. a) H.M. Yuan, G.S. Zhu, J.S. Chen, W. Chen, G.D. Yang, R.R. Xu, *J. Solid State Chem*. **2000**, *151***,** 145*;* b) P.M. Forste, A.K. Cheetham, *Topics in Catalysis* **2003**, *24*, 79; c) *S.* Bauer, N. Stock, N. *Angew. Chem .Int. Ed.* **2007**, *46*, 6857.

31. J. Li, Z. Chen, R.J. Wang, D. M. Proserpio, *Coordination Chemistry Review*, **1999**, *190-192*, 707.

32. R.M. Barrer, *Hydrothermal Chemistry of Zeolites*, Academic Press, London, **1982**.

CHAPTER TWO

OPTICAL PROPERTIES OF DOUBLE LAYER II-VI BASED HYBRID SEMICONDUCTORS

Solid state lighting (SSL) technologies including light emitting diodes (LEDs) represent a promising approach to decrease the energy consumption and reduce CO_2 emission.[1] Replacing the conventional lighting systems with solid state lighting technologies is predicted to reduce the world's electricity consumption for lighting by 50% by 2020.[1] Compared to incandescent lamps, LEDs are brighter, more efficient, have lower power consumption, and a longer lifetime.[1]

Today, rare earth elements (REE) play an important role in production of many electronics including LEDs. Due to their luminescence properties, they are a critical component of phosphors used in LED.[2] Due to the high demand for rare-earth elements in various applications and technologies, there is concern that the demand of some of these materials might exceed the present supply within a few years. Chine is the main supplier of the rare earth metals and about 97% of rare earth ores and rare earth oxides are produced by China.[2] If China cut its export, as it happened in 2010, world's access to rare earth metals would be restricted. In addition to the export restriction, the high demand and shortage of supply lead to a significant increase in rare earth prices. To solve this problem, new supplies of REE needs to be explored and techniques have to be developed for higher efficiencies in mining. Another option is to find the substituent for REE. Due to the importance of REE in lighting technology, and their applications in LEDs, shortage of supply and rising of the price will have a negative effect on these technologies. Therefore, development of new rare-earth free materials is required that can be used as alternative phosphors with high efficiency and high light quality.

In an effort to explore new materials for LEDs, hybrid semiconductor materials built on periodically arranged two-dimensional (2D) layers of ZnS and organic

amines has been developed. These hybrid systems, which are free of rare-earth elements, generate direct white light in their bulk form.[3] Their emission intensity, range, quantum efficiency, and color quality can be systematically tuned by varying the composition of both the inorganic and organic components. This unique family of solution-processable, low-cost, and high-efficiency hybrid semiconductor bulk materials shows great promise as a new type of single-phase white-light-emitting phosphors and may particularly be suitable for use in white light emitting diodes (WLEDs) which are of intense interest because of the great need in general illuminations. Developing of single-emitting bulk materials that generate white light is of great interest because complex procedure of mixing and color balancing, size control, and self absorption is reduced or avoided. Consequently, the quantum yield is significantly improved.

2.1 Zn_2S_2 (*L*)

2.1.1 Structure

Structure of Zn_2S_2 (*L*) (*L* = *pa*, *ba*, *ha* and *oa*) is composed of alternating 2D-modules of ZnS layers and amine molecules in periodic arrangement (**Fig. 2.1**). ZnS (inorganic) layers have a uniform thickness and are bonded to organic layers via coordinate bonds. The Zn_2S_2 (*L*) (*L* = *pa*, *ba*, *ha* and *oa*) compounds crystallize in orthorhombic space groups (**Table 2.1**).[3,4] Enlargement of unite cell as a result of the increases in a amine's chain length from *pa* to *oa* leads to the shift of the first diffraction in the PXRD pattern to the lower angles (**Fig. 2.2**). They feature a double-layer structure made of 2D ZnS semiconductor motifs (~8Å in thickness) that are bonded to amine (*L*) molecules (**Fig. 2.1**).[3a, 4]

Table 2.1. GSAS Rietveld refinement results for 2D-$Zn_2S_2(L)$ (*L* = *pa*, *ba*, *ha* and *oa*).

Empirical Formula	$C_3H_9NS_2Zn_2$ [Zn_2S_2(*pa*)]	$C_4H_{11}NS_2Zn_2$ [Zn_2S_2(*ba*)]	$C_6H_{15}NS_2Zn_2$ [Zn_2S_2(*ha*)]	$C_8H_{19}NS_2Zn_2$ [Zn_2S_2(*oa*)]
Fw	254.00	268.03	296.08	324.13
Space Group	*Pbca* (No.61)	*Pbca* (No.61)	*Pbca* (No.61)	*Pbca* (No.61)
***a*(Å)**	6.240	6.189	6.190	6.210
***b*(Å)**	5.801	5.747	5.746	5.703
***c*(Å)**	37.704	42.595	52.501	62.502
V(Å^3)	1356.0	1514.7	1840.7	2213.5
Z	8	8	8	8
T	293	293	293	293
λ(Å)	1.54	1.54	1.54	1.54
2θ Range(°)	3-50	3-50	3-50	3-50

2.1.2 Optical band-gap

At room temperature $Zn_2S_2(L)$ shows a sharp absorption edge and its absorption intensity is enhanced and blue-shifted compare to those of the ZnS bulk compound. $Zn_2S_2(L)$ has an optical band gap of 3.9eV which is about 0.4eV higher than that of the parent structure, ZnS (3.5 eV) (**Fig. 2.3**).

2.1.3 Photoluminescence

$Zn_2S_2(L)$ emits strongly in the green-blue region with its emission peak centered at ~425 nm (λ_{ex}: 360nm) (**Fig. 2.4**). It photoluminescence intensity is enhanced compare to that of the ZnS (peak at ~420nm) bulk compound. Similar blue emission with a peak centered at 425nm has been observed for the inorganic/organic ZnS/$NaSCH_2COONa$ nanocomposite which is also ascribed to the sulfur vacancies.[4] Emission from the ZnS nanoparticle in the range of 420~450nm has been also attributed to sulfur vacancies.[5]

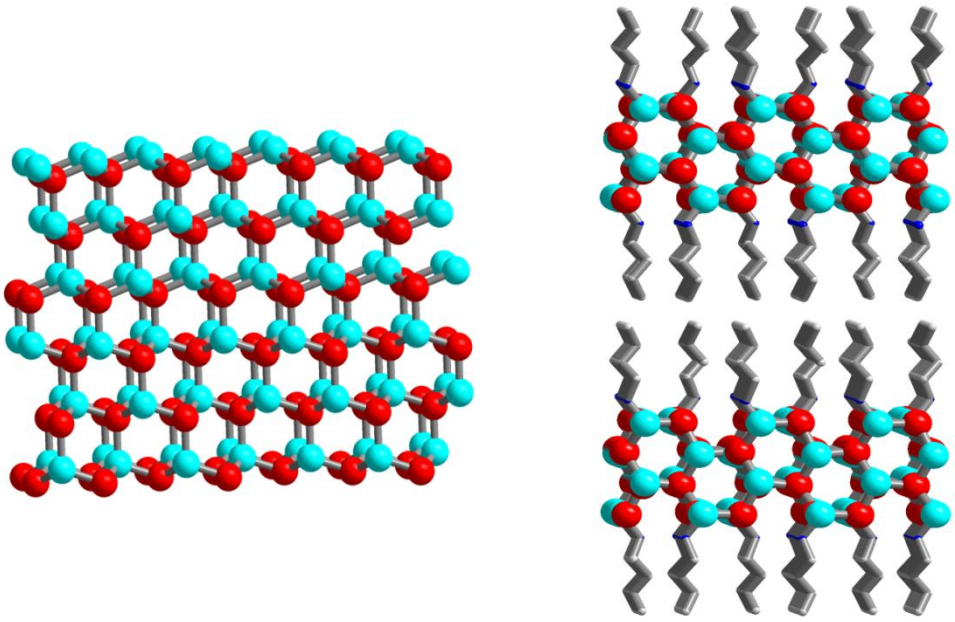

(a) **(b)**

Figure 2.1 Schemetic of (a) double layer of honeycomb-like net of ZnS in the $M_2Q_2(L)$ type hybrid structures (M = Zn; Q = S; L = mono-amine), (b) double-layer 2D-$M_2Q_2(L)$ structure.

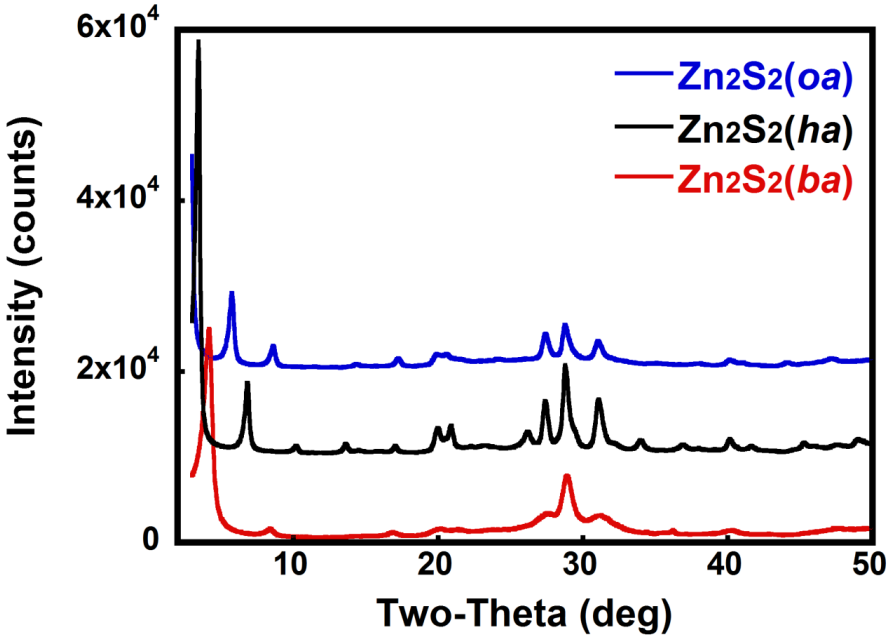

Figure 2.2 Comparison of PXRD patterns of 2D-Zn_2S_2(*ba*) (red), 2D-Zn_2S_2(*ha*) (black), and 2D-Zn_2S_2(*oa*)(blue) structures.

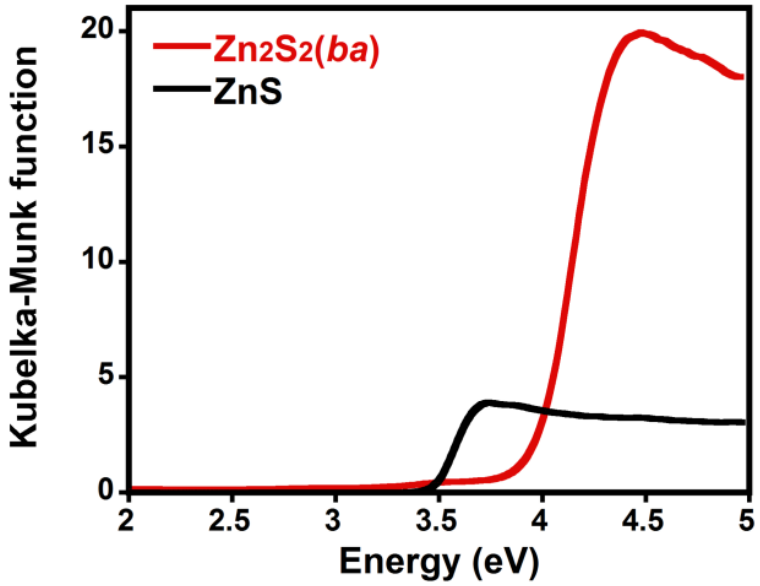

Figure 2.3 Room temperature absorption spectra of Zn_2S_2(*ba*) compared to ZnS binary compound (both in powder forms).

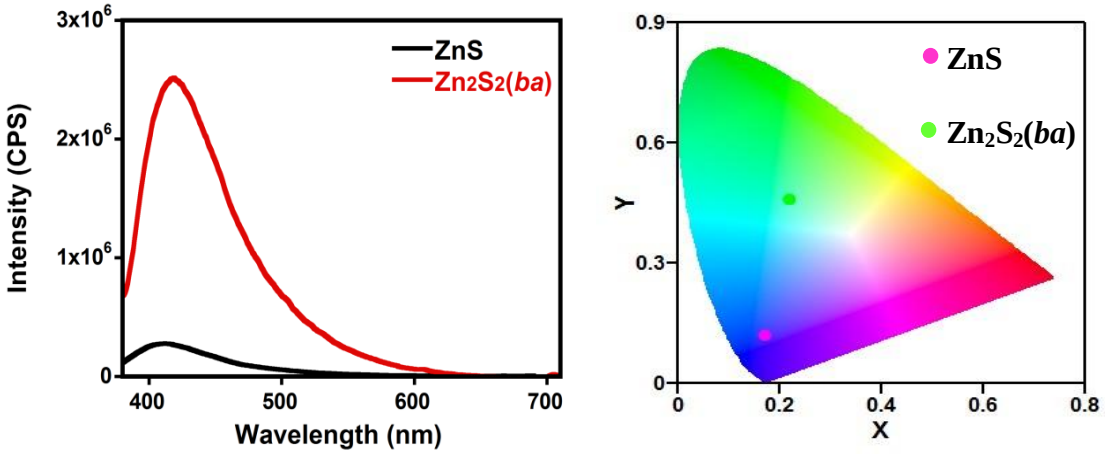

(a) **(b)**

Figure 2.4 (a) Comparison of room temperature emission spectra of Zn_2S_2(*ba*) and ZnS binary compound (λ_{ex} = 360 nm), (b) CIE coordinates of ZnS (0.17, 0.12) and Zn_2S_2(*ba*) (0.22, 0.46) showing their emissions in the blue and green regions, respectively.

The observed emission for $Zn_2S_2(L)$ is not a band-edge emission and can be attributed to the effect of the surface traps introduced by amines, defect-state recombination at the surface,[6] or it can be due to the self-activated centers as a result of the crystal lattice vacancies.[6] Although the shape of the emission peak of $Zn_2S_2(L)$ resembles that of the ZnS, the former with the C.I.E. Chromaticity Coordinates of (0.22,0.46) covers a wider range of wavelengths and generates the bluish white light while ZnS emits blue light with CIE coordinates of (0.17,0.12)(**Fig. 2.4b**)

One possible explanation for the observed emission enhancement in $Zn_2S_2(L)$ compared to ZnS is that amines are Lewis bases and they can donate electrons to Zn^{2+} and this lead to the reduction of the nonradioactive decay. [6] The same effect was observed for CdS colloids modified with ($N(C_2H_5)_3$) where the amine acts as a donor and reduce the nonradioactive decays.[6] Amine also acts as passivating agent and reduces the chances of nonradioactive decays due to the surface traps.[7]

2.2 Effect of doping on optical properties

2.2.1 Selenium substitution

Although the emission intensity of $Zn_2S_2(L)$ is enhanced compared to that of the ZnS, its emission peak is too narrow to be suitable for generating white light. To obtain a white light emission, materials with broad emissions covering the entire visible spectrum are required. In an effort to broaden the emission range of $Zn_2S_2(L)$, the effect of Se substitution on the emission range was investigated. Samples with different amount of Se in a range of 5-25 mol percent were synthesized and their phase purity was confirmed by PXRD. **Fig. 2.5** shows the room temperature absorption spectra of the $Zn_2S_{2-x}Se_x(ba)$

where x is 0.10, 0.20, 0.30, 0.40, and 0.50. As the amount of Se increases the band gap of the compound decreases but this change in the band gap is small. Replacing S with Se leads to the decrease in the emission intensity but it doesn't have any significant effect on the emission range. Observed emission spectra resembles that of the undopped Zn_2S_2(*ba*) with an emission peak at 420nm (λ_{ex}:360nm) (**Fig. 2.6**). The emission at around 425nm can be attributed to the self-activated centers due to the crystal lattice vacancies,[5] or it can be due to the to the effect of the surface traps introduced by amine. Further investigation is needed to be able to determine the reason for this emission.

2.2.2 Cadmium substitution

Cd_2S_2(*L*), an analogue of Zn_2S_2(*L*), shows a broad emission that covers the entire visible range and it generates white light upon excitation with UV light. However, its emission intensity is very low and has low quantum efficiencies (QY: ~4-5%).[3] Zn_2S_2(*ba*) is giving an order of magnitude increase in the emission intensity compared to that of the Cd_2S_2(*ba*) analogue. In an effort to enhance the performance of these materials we have developed a series of cadmium doped ZnS based Zn_2S_2(*L*) compounds. To study the effect of Cd on the emission of five sets of samples with different concentration of Cd were synthesized. **Fig. 2.7** shows the room temperature absorption spectra of $Zn_{2-x}Cd_xS_2$(*ba*) compounds where x = 0.1, 0.20, 0.30, 0.40, 0.50. Absorption spectra of all 5 samples show one sharp band edge absorption peak which shows that phase separation has not occurred. The absorption edge moves toward the higher wavelength and the band-gap increases as the amount of Cd increases. Results suggest that it is possible to effectively modulate the band gap of Zn_2S_2 (*L*) by substitution of Zn with different amount of Cd.

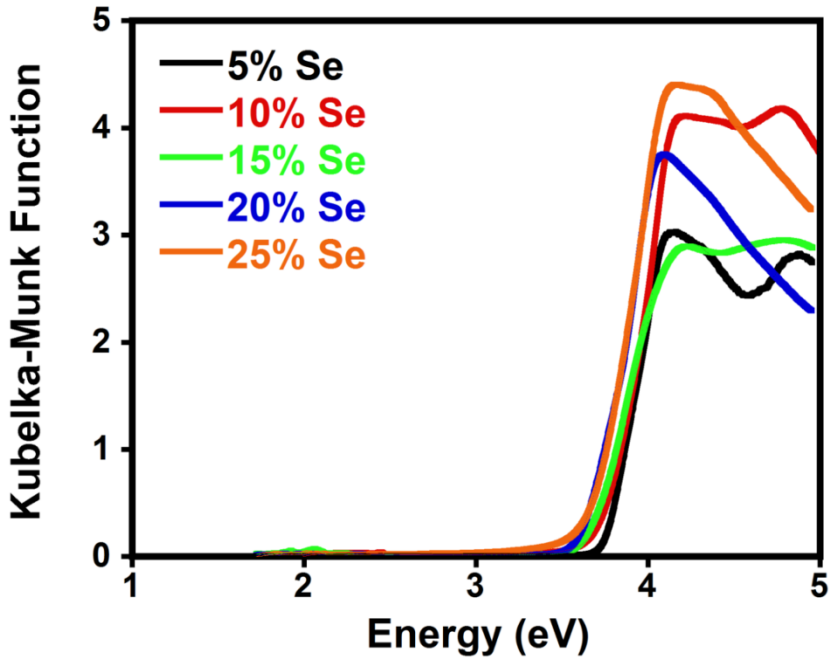

Figure 2.5 Room temperature absorption spectra of $Zn_2S_{2-y}Se_y$(*ba*) where y = 0.10, 0.20, 0.30, 0.40, 0.50.

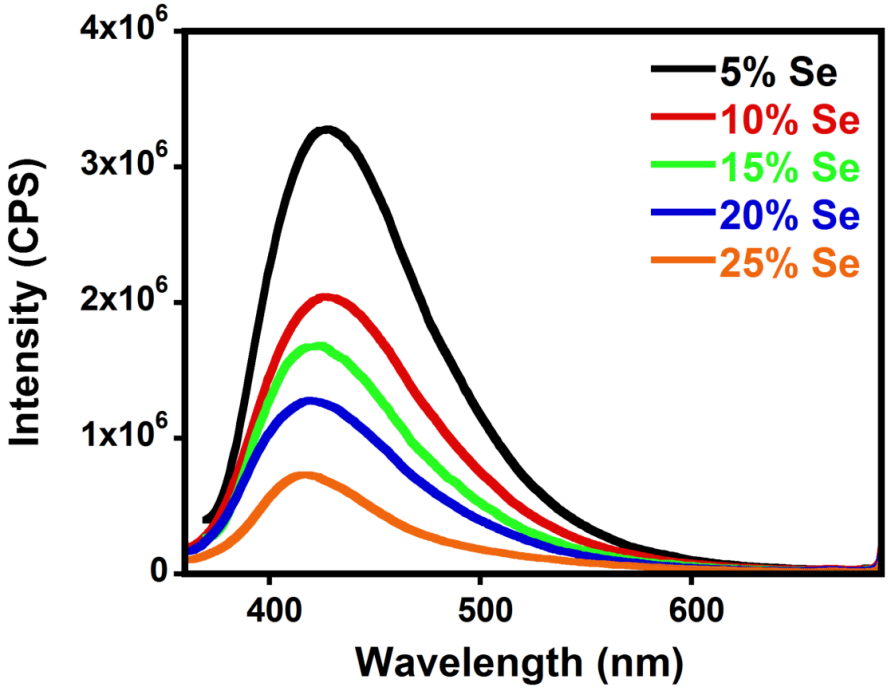

Figure 2.6 Room temperature emission spectra of $Zn_2S_{2-y}Se_y$(*ba*) where y = 0.10, 0.20, 0.30, 0.40, 0.50 (λ_{ex} = 360 nm).

Figure 2.8 shows the room temperature PL emission spectra of the ternary $Zn_{2-x}Cd_xS_2$(*ba*) hybrid compounds (x = 0.10, 0.20, 0.30, 0.40 and 0.50), along with those of Zn_2S_2(*ba*) (x = 0) and Cd_2S_2(*ba*) (x = 2). As the Cd content increases the emission intensity for $Zn_{2-x}Cd_xS_2$ (*ba*) gradually decreases. Such a decrease in the PL emission intensity is also observed for the $Cd_xZn_{1-x}S$ nanoparticles prepared at room temperature.[8] Lowering of the PL emission is most likey due to defects created by introducing the Cd atoms into the Zn_2S_2 slabs. Defects sites originated from the lattice mismatch can act as the nonradiative recombination centers, leading to a decrease in PL emission.[9,10]

Although substitution of Zn by Cd suppresses the emission intensity but, on the positive side, it also broadens the emission spectrum. Upon addition of 10 mol percent or more Cd, two emission peaks appear and the emission range becomes wider. An optimized composition of $Zn_{1.7}Cd_{0.3}S_2$ (*ba*) gives rise to a well-balanced broad emission peak, as shown in **Fig. 2.9**. $Zn_{1.7}Cd_{0.3}S_2$ (*ba*) illustrate a single and sharp band edge absorption peaks (**Fig. 2.7**), from which a band gap of ~2.9 eV is estimated. $Zn_{1.7}Cd_{0.3}S_2$ (*ba*)'s emission intensity is higher than that of the Cd_2S_2 (*ba*) (**Fig. 2.9a**) and it is broader than that of the Zn_2S_2 (*ba*) (**Fig. 2.9b**). Phase purity is confirmed by powder X-ray diffraction, elemental analysis (EA), thermogravimetric analysis (TGA) (**appendix III**), and optical absorption experiments. The CIE coordinates of $Zn_{1.7}Cd_{0.3}S_2$(*ba*) is calculated to be (0.31,0.37), well within the white region defined by the International Commission on Illumination (CIE) 1931 color space chromaticity diagram (**Fig. 2.10**). The very broad emission peak of $Zn_{1.7}Cd_{0.3}S_2$ (*ba*) is most likely a combined result of band edge emission, Cd substitution, [9,11] and also possibly contributions from the ligand modulated trap-state [10,11] and surface state emission related to its 2D nanostructures.[10,11]

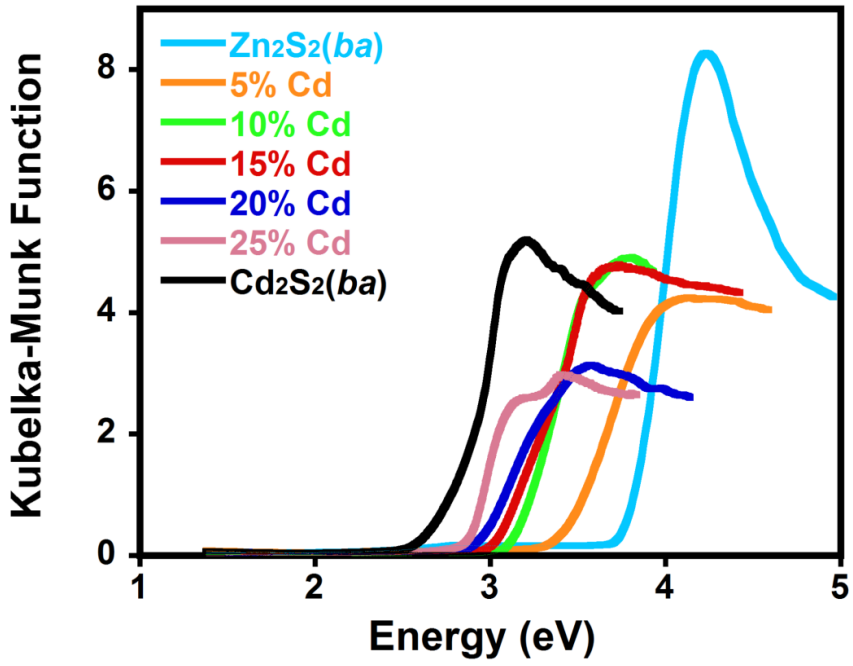

Figure 2.7 Room temperature absorption spectra of $Zn_{2-x}Cd_xS_2$(*ba*) compounds where x = 0.1, 0.20, 0.30, 0.40, 0.50.

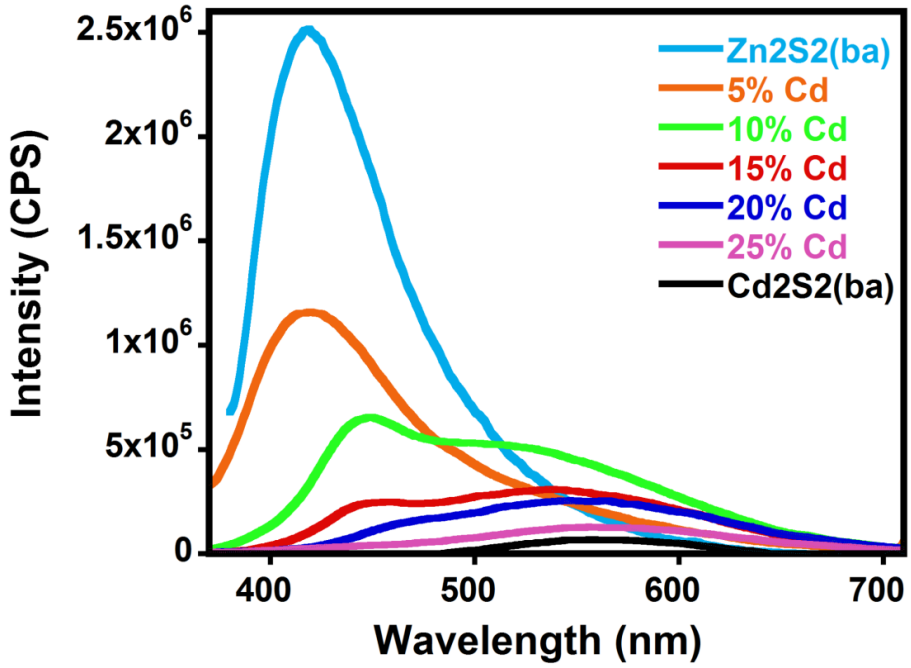

Figure 2.8 Room temperature emission spectra of $Zn_{2-x}Cd_xS_2$(*ba*) compounds where x = 0.1, 0.20, 0.30, 0.40, and 0.50 (λ_{ex}: 360nm).

$Zn_{1.7}Cd_{0.3}S_2$(*ba*) emits a bright white light and its white light emission is illustrated in **Figure 2.10**. The reference UV LED (360 nm) emits blue light (**Fig. 2.10a**). Upon coating its surface with a thin layer of $Zn_{1.7}Cd_{0.3}S_2$ (*ba*) (**Fig. 2.10b**), the LED change the emission color from blue to white (**Fig. 2.10c**). The fluorescence QY of the $Zn_{1.7}Cd_{0.3}S_2$(*ba*), obtained by both relative/comparative and absolute methods on solution and solid samples, is in the range of 12-13%, significantly higher than those of the previously achieved values for Cd_2S_2(*ba*) (4-5%) [3a] and CdSe QDs (2-3%).[12a]

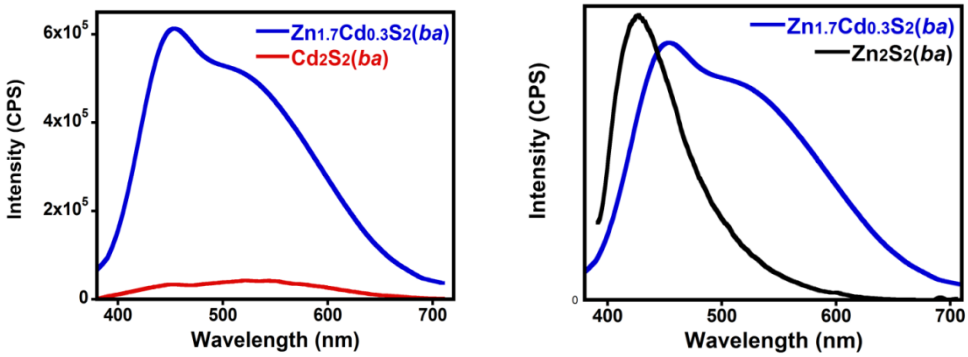

Figure 2.9 Room temperature emission spectra of (a) Zn_2S_2(*ba*) with 15% Cd compare to that of the Cd_2S_2(*ba*), showing the difference in emission intensity of the two compounds, (b) Zn_2S_2(*ba*) with 15% Cd compare to non-doped Zn_2S_2(*ba*), showing the broadening of the spectrum upon addition of Cd.

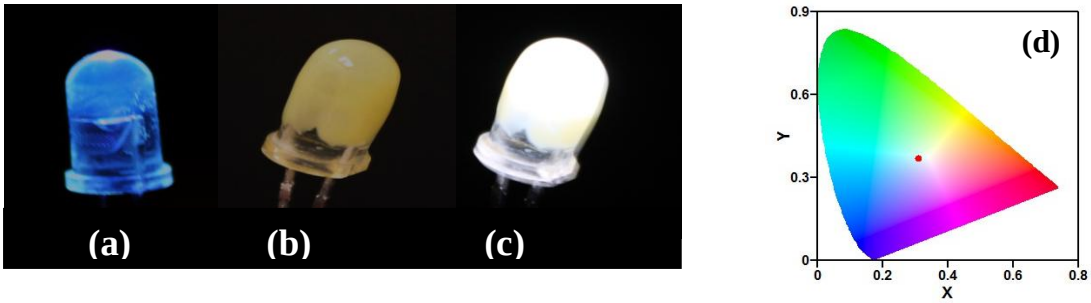

Figure 2.10 White-light assemblies using the 2D-$Zn_{1.7}Cd_{0.3}S_2$(*ba*) phosphors, (a) 5 mm reference UV LED (360 nm) illuminates blue light (commercially available from Le Group Fox, Inc.), (b) the same LED coated with a thin layer of $Zn_{1.7}Cd_{0.5}S_2$(ba), (c) the same LED in (b) illuminating, **(**d) CIE diagram showing the chromaticity coordinates of $Zn_{1.7}Cd_{0.3}S_2$ (*ba*) (0.31,0.37).

2.2.3 Manganese substitution

The effect of Mn on the electronic and optical properties of hybrid compounds including band-gap, photoluminescence intensity and emission range was also examined. Previous studies have shown that Mn doping enhanced the photoluminescence intensity.[13, 14] It has also been shown that emission range and the emission peak position can be tuned by addition of small amount of Mn.[14] Those studies shows that the coordination environment of Mn^{2+} and the strength of the crystal field determines the position of the emission peak.[15]

Optical properties of $Zn_{1.7}Cd_{0.3}S_2$(*ha*) with different amount of Mn have been studied. Although substitution of small amount of Mn doesn't impose any noticeable effect on the band-gap of the compound (**Fig. 2.11**) but it does lead to significant change in the emission intensities (**Fig. 2.12**). Addition of a very small amount of Mn leads to an increase in the emission intensity. The maximum enhancement occurs when the concentration of Mn reaches to ~0.08 mole percent. Higher concentrations give rise to reduced PL intensity (**Fig. 2.13**). The same trend was reported for Mn doped CdS quantum dots. [16] Quenching of the PL intensity at higher Mn^{2+} concentrations is due to the concentration quenching. [17]At higher Mn^{2+} concentration, the energy migration among the ions leads to the loss of energy in defect sites via nonradiactive decays.[17]

Mn^{2+} 3d-electrons are the efficient centers for luminescence, they also interact with s-p orbitals of the host ZnS crystals. Mixed electronic states of the Mn and the host lattice facilitate the efficient energy transfer from the ZnS host to the Mn^{2+} ions. The very strong confinement in the 2D layers of the hybrid systems further promotes such energy transfer.

Since the band-gap of $Zn_{1.7}Cd_{0.3}S_2$(*ha*) (2.9eV) is greater than the energy of Mn^{2+} internal transition (~2.12eV), Mn^{2+} luminescence is observed.[13] In the Mn doped compound, first the excited electron/hole pairs transfer into Mn^{2+} ions, then recombination of the 3d electrons and holes occur and this leads to the observed luminescence and is responsible for the red shift in the emission peak (**Fig. 2.12**).[13, 14]

Addition of Mn and the consequent shift in an emission peak results in emission of a warmer color with a lower correlated color temperature (CCT) of 4061K compare to that of the similar but un-doped sample (CCT of $Zn_{1.7}Cd_{0.3}S_2$(*ha*) is 7775K). A more yellowish appearance of the emitted light compare to that of the un-doped sample can be seen in **Fig. 2.14**. $Zn_{1.7}Cd_{0.3}S_2$(*ha*): 0.08%Mn with the chromacity coordinates of (0.37, 0.37) has a color rendering index of (CRI) of 86 which is higher than that of the commercially available YAG:Ce^{3+}. Calculated CRI, CCT, and CIE data are summarized in **Table 2.2**. The Fluorescence quantum yield for the $Zn_{1.7}Cd_{0.3}S_2$ (*ha*): 0.08%Mn is calculated to be of 26-29%, a remarkable increase compare to the undoped compounds.

Table 2.2 Calculated CRI, CCT, and CIE data.

Formula	**x**	**y**	**CCT**	**CRI**
$Zn_{1.7}Cd_{0.3}S_2$(*ha*)	0.292	0.324	7775	83
$Zn_{1.7}Cd_{0.3}S_2$(*ha*):0.08% Mn	0.376	0.370	4061	86
$Zn_{1.7}Cd_{0.3}S_2$(*oa*)	0.303	0.367	6703	86
$Zn_{1.7}Cd_{0.3}S_2$(*oa*):0.08% Mn	0.358	0.373	4629	86

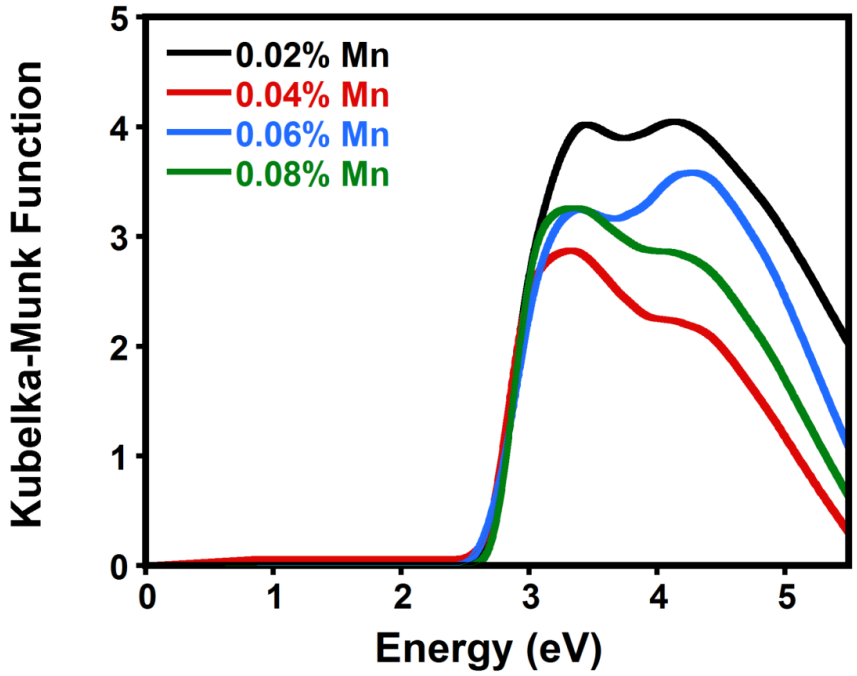

Figure 2.11 Room temperature absorption spectra of $Zn_{1.7}Cd_{0.3}S_2$(*ha*):Mn at various Mn concentrations.

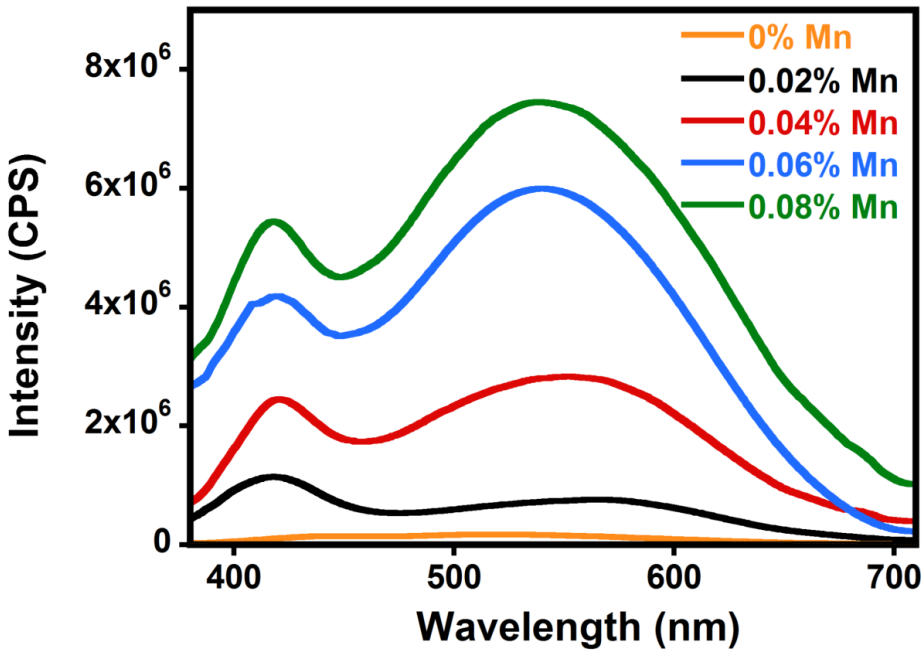

Figure 2.12 Room temperature emission spectra of $Zn_{1.7}Cd_{0.3}S_2$(*ha*):Mn at various Mn concentrations (λ_{ex} = 360 nm).

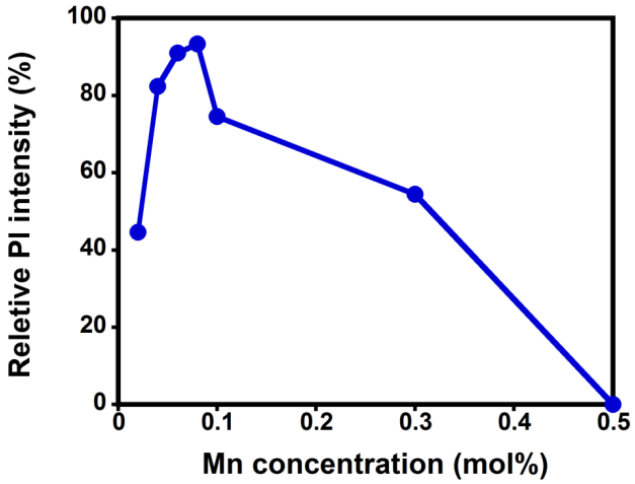

Figure 2.13 Integrated emission intensity of $Zn_{1.7}Cd_{0.3}S_2$(*ha*):Mn as a function Mn dopant amount (0.02-0.5 mol%).

2.3 Effect of ligand on optical properties

To examine the effect of organic ligands on the absorption and emission behavior of the hybrid compounds, four amines, propylamine (*pa*), butylamine (*ba*), hexylamine (*ha*), and octylamine (*oa*), with various chain lengths were used for synthesis of four sets of $Zn_{1.7}Cd_{0.3}S_2$(*L*) samples. All compounds were structurally characterized by PXRD methods. Data used for the Rietveld refinement of the double-layer 2D-Zn_2S_2(*L*) structures were collected in a 2θ range of 3-50° at room temperature with a scan speed of 0.05°/min using Rigaku D/M-2200T automated diffraction system (Ultima+) using Cu Kα radiation (λ = 1.5406 Å). The PXRD pattern of 2D-Zn_2S_2(*ba*), 2D-Zn_2S_2(*ha*), and 2D-Zn_2S_2(*oa*) are shown in **Fig. 2.2**. All four double-layer structures crystallize in orthorhombic crystal system. *GSAS* Rietveld Refinement data are summarized in **Table 2.3** and the calculated PXRD patterns are shown in **appendix III**.

As it is shown in **Fig. 2.15**, increasing the chain length follows by the enhancement

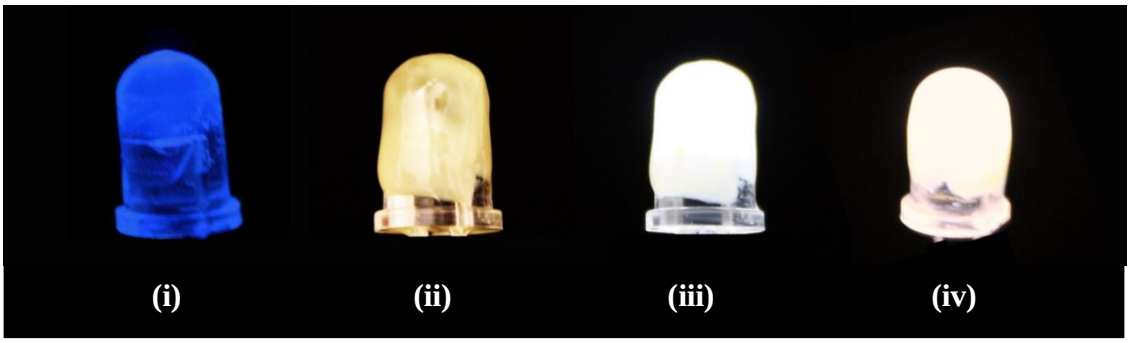

(a)

(b)

(c)

Figure 2.14 **(**a) White-light LED assemblies made by coating thin-film samples on the surface of a 5 mm reference UV LED (360 nm emission, commercially available from Le Group Fox, Inc.): (i) illuminating reference UV LED, (ii) the same LED in (i) coated with a thin layer of $Zn_{1.7}Cd_{0.3}S_2$(*ha*) prepared in a DMSO solution (before illumination), (iii) The same LED in (ii) illuminating, and (iv) $Zn_{1.7}Cd_{0.3}S_2$(*ha*):0.08%Mn coated LED illuminating, (b) bright white light from a $Zn_{1.7}Cd_{0.3}S_2$(*ha*):0.08%Mn and (c) from $Zn_{1.7}Cd_{0.3}S_2$(*ha*) deposited on glass excited at 365 nm with a UV lamp.

Semiconductor systems.[3a] Since the inorganic layer $Zn_{1.7}Cd_{0.3}S_2$ remains the same in all three compounds, enhancement of PL intensity should be related to the amine length. Introduction of amines between the double layers of semiconductor results in a strong quantum confinement along the packing direction of the II-VI layers. This quantum confinement leads to the formation of 2D exciton.[13] As the length of amine molecule increases, the interlayer interactions are reduced, and thus, an enhanced quantum confinement to the 2D inorganic layers. Consequently, local carrier density of states close to Fermi energy is increased and more electrons become available, leading to the enhancement of PL intensity.[13] In contrast to their strong effect on the PL emission intensity, changes in amine chain length show negligible effect on the band gap of the hybrid compounds (**Fig. 2.16**).

Fluorescence QY of 15-17% was obtained for $Zn_{1.7}Cd_{0.3}S_2$(*ha*) (C6 amine) and QY was increased to 25-28% for $Zn_{1.7}Cd_{0.3}S_2$ (*oa*) (C8 amine). When Mn was doped (0.08 mol %) in to a sample containing the amine with the longest chain length, $Zn_{1.7}Cd_{0.3}S_2$(*oa*), QY was increased to 31-37%, a value that is approaching to some of the phosphors currently used in commercial WLED productions.[1]

2.4 Conclusions

In summary, a new family of single white light emitting semiconuctor materials in bulk form has been developed. These ZnS-based crystalline inorganic-organic hybrid semiconductors with the well defined and precisely controllable crystal structure and composition have a high florescence quantum yield. Their optical properties, including band-gap, emission intensity, quantum yield, and color quality, can be systematically tuned

by varying the composition of both inorganic and organic components. High quantum yield of 37% was obtained for a 0.08% Mn doped sample of $Zn_{1.7}Cd_{0.3}S_2$(*oa*). High quantum yield combined with other properties such as excellent solution-processability, low-temperature and cost-effective one-pot synthesis, accurate stoichiometry control, and high yield, are among the advantageous features of the ZnS based hybrid materials over and QD based phosphors and (YAG):Ce^{3+} phosphors that currently dominating the commercial market of WLEDs. In addition, being free of rare-earth elements, these hybrid materials are not affected by supply chain vulnerability and rise of the price of those elements. Also their production is not dependent on the single national supplier.

Table 2.3 GSAS Rietveld refinement results for 2D-Zn_2S_2 (*L*) (*L = pa*, *ba*, *ha* and *oa*).

Empirical Formula	**$C_3H_9NS_2Zn_2$ [Zn_2S_2(*pa*)]**	**$C_4H_{11}NS_2Zn_2$ [Zn_2S_2(*ba*)]**	**$C_6H_{15}NS_2Zn_2$ [Zn_2S_2(*ha*)]**	**$C_8H_{19}NS_2Zn_2$ [Zn_2S_2(*oa*)]**
Fw	254.00	268.03	296.08	324.13
Space Group	*Pbca*	*Pbca* (No.61)	*Pbca* (No.61)	*Pbca* (No.61)
a (Å)	6.240	6.189	6.190	6.210
b (Å)	5.801	5.747	5.746	5.703
c (Å)	37.704	42.595	52.501	62.502
V(Å^3)	1356.0	1514.7	1840.7	2213.5
Z	8	8	8	8
T	293	293	293	293
λ (Å)	1.54	1.54	1.54	1.54
2θ Range(°)	3-50	3-50	3-50	3-50

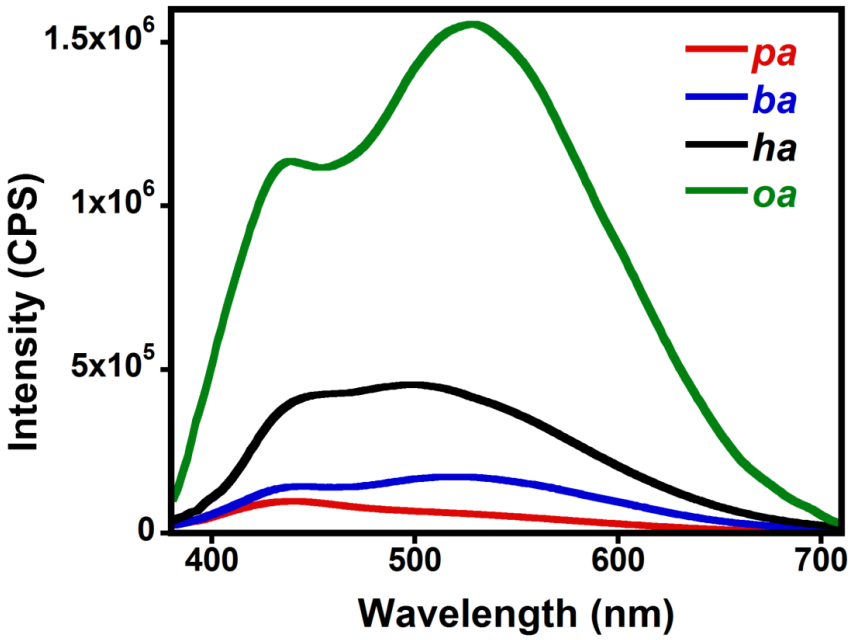

Figure 2.15 Room temperature emission spectra of $Zn_{1.7}Cd_{0.3}S_2$(*L*) (*L = pa, ba, ha, oa)* (λ_{ex}: 360nm).

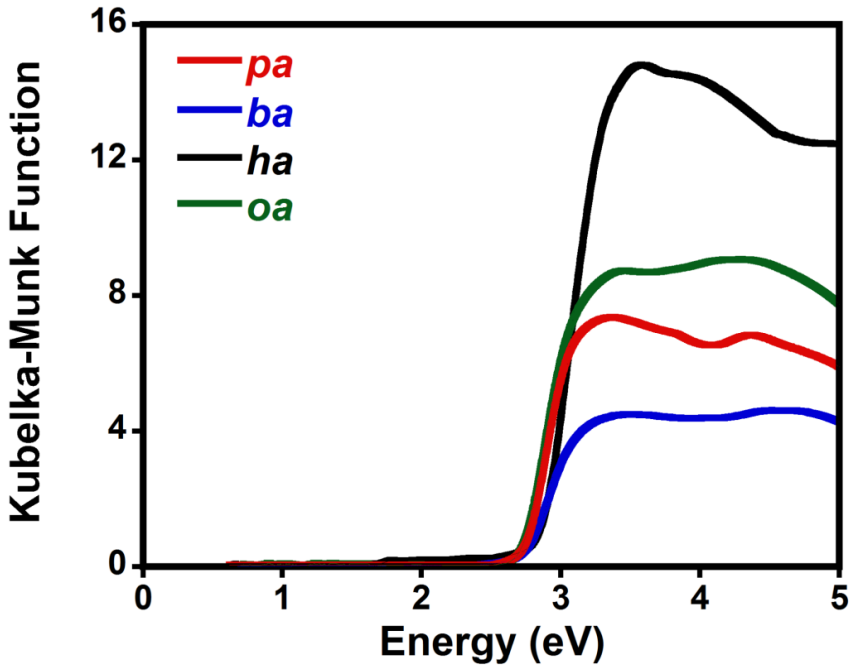

Figure 2.16 Room temperature absorption spectra of $Zn_{1.7}Cd_{0.3}S_2$(*L*) (*L = pa, ba, ha, oa*). Estimated band gap values are 2.89, 2.89, 2.90 and 2.92 eV for *pa*, *ba*, *ha*, and *oa*, respectively.

2.5 References

1. a) Worldwide Trends in Energy Use and Efficiency; International Energy Agency, Paris, France 2008; b) Solid-State Lighting http://ssls.sandia.gov/; c) U.S. Department of Energy, "*Energy Savings Potential of Solid-State Lighting in General Illumination Applications",* Prepared for: Solid-State Lighting Program, January **2012**; d) U.S. Energy Information Administration, *Annual Energy Review*, **2012**; e) U.S. Energy Information Administration, www.eia.gov.

2. a) C.R. Ronda, T. Justel, H. Nikol, *J. Alloys and Compounds* **1998**, *275-277*,669; b) J. Lifton, "The Battle Over Rare Earth Metals", *J. of Energy Security* **2010**; c) D. Schüler, M. Buchert, R. Liu, S. Dittrich, C. Merz, "Study on Rare Earths and Their Recycling", *Final Report for The Greens/EFA Group in the European Parliament*, **2011.**

3. a) W. Ki, J. Li, *J. Am. Chem. Soc.* **2008**, *130*, 8114 – 8115; b)W. Ki, J. Li, G. Eda, M. Chhowalla, *J. Mater. Chem.* **2010**, *20*, 10676; c) M. Roushan, X. Zhang, J.Li, *Angew. Chem. Int. Ed.* **2012**, *51*, 436; d) X. Fang, M. Roushan, R. Zhang, J. Peng, H. Zeng, J. Li, *Chem. Mater.* **2012**, *24* (10), 1710.

4. a) X. Y. Huang, J. Li, *J. Am. Chem. Soc.* **2007**, 129, 3157; b) X. Y. Huang, H. R. Heulings,V. Le, J. Li, *Chem. Mater.* **2001**, 13, 3754; c) X. Y. Huang, J. Li, H. X. Fu, *J. Am. Chem. Soc*. **2000**, 122, 8789; d) X. Y. Huang, J. Li, Y. Zhang, A. Mascarenhas, *J. Am. Chem. Soc.* **2003**, *125*, 7049; e) X. Y. Huang, M. Roushan, T. J. Emge, W. H. Bi, S. Thiagarajan, J. H. Cheng, R. G. Yang, J. Li, *Angew. Chem. Int. Ed.* **2009**, 48, 7871.

5. a) W.H. Zhang, J.L. Shi, H.R. Chen, Z.L. Hua, D.S. Yan, *Chem. Mater*. **2001**, 13, 648; b) Qian, Y. T.; Liu, Y. K.; Xi, G. C.; Chen, S. F.; Zhang, X. F.; Zhu,Y. C. *Nanotechnology* **2007**, 18, 285605; c) S. Sapra, A. Prakash, A. Ghangrekar, N. Periasamy, D.D. Sarma, *J.Phys. Chem. B* **2005**, *109*, 1663; d) W.C. Becker, A.J. Bard, *J. Phys. Chem.* **1983**, *87*, 4888.

6. T. Dannhauser, M. O'Neil, K. Johansson, D. Whitten, G. McLendon, *J. Phys. Chem.* **1986**, *90*, 6074.

7. J. Lu, S. Wei, Y. Peng, W. Yu, Y. Qian, *J. Phys. Chem. B* **2003**, *107*, 3427.

8. Y. C. Li, M.F. C.H. Ye, Yang, X.H. Li, Y.F. Li, *Adv. Func. Mater.* **2005**, *15*, 433.

9. J. Z. Liu, P. X. Yan, G. H. Yue, J. B. Chang, D. M. Qu, R.F. Zhuo, *J. Phys. D: Appl. Phys.* **2006**, *39*, 2352.

10. a) N. A. Hill, K. B. Whaley, *J. Chem. Phys.* **1994**, *100*, 2831; b) D. F. Underwood, T. Kippeny, S. J. Rosenthal, *J. Phys. Chem. B* **2001**, *105*, 436; c) M. A. Schreuder, K. Xiao, I. N. Ivanov, S. M. Weiss, S. J. Rosenthal, *Nano Lett.* **2010**, *10*, 573; d) M. A. Schreuder, J. R. McBride, A. D. Dukes, J. A. Sammons, S. J. Rosenthal, *J. Phys. Chem. C* **2009**, *113*, 8169.

11. a) S. Biswas, S. Kar, S. Santra, Y. Jompol, M. Arif, S. I. Khondaker, *J. Phys. Chem. C* **2009**, *113*, 3617 – 3624; b) P. Yang, M. Lu, D. Xu, D. Yuan, G. Zhou, *Appl. Phys. A* **2001**, *73*, 455.

12. a) M. J. Bowers II, J. R. McBride, S. J. Rosenthal, *J. Am. Chem. Soc.* **2005**, *127*, 15378; b) M. J. Bowers II, J. R. McBride, M. D. Garrett, J. A. Sammons, A. D. Dukes, M. A. Schreuder, T. L. Watt, A. R. Lupini, S. J. Pennycook, S. J. Rosenthal, *J. Am. Chem. Soc.* **2009**, *131*, 5730; c) M. A. Schreuder, J. D. Gosnell, N. J. Smith, M. R. Warnement, S. M. Weiss, S. J. Rosenthal, *J. Mater. Chem*. **2008**, *18*, 970.

13. a) S. Sapra, A. Prakash, A. Ghangrekar, N. Periasamy,D. D. Sarma, *J. Phys. Chem. B* **2005**, *109*, 1663; b) J. Lu, S.Wei,W. C. Yu, H. B. Zhang, Y. T. Qian, *Chem. Mater.* **2005**, *17*, 1698; c) J. Lu, S. Wei, Y. Peng, W. Yu, Y. Qian, *J. Phys. Chem. B* **2003**, *107*, 3427; d) M. Zhang, C. Shi, T.-K. Zhang, L. Chang, W.-T. Yao, S. H. Yu, *Chem. Mater.* **2009**, *21*, 5485.

14. a) S. W. Lu, B. I. Lee, Z. L. Wang, W. S. Tong, B. K. Wagner, W. Park, C. J. Summers, *J. Lumin.* **2001**, *92*, 73; b) R. N. Bhargava,D. Gallagher, X. Hong,A. Nurmikko, *Phys. Rev. Lett.* **1994**, *72*, 416; c) A. Nag, D. D. Sarma, *J. Phys. Chem. C* **2007**, *111*, 13641.

15. N. Guo, Y. J. Huang, H. P. You, M. Yang, Y. H. Song, K. Liu,Y. H. Zheng, *Inorg. Chem.* **2010**, *49*, 10907.

16. L. Levy, N. Feltin, D. Ingert, M. P. Pileni, *Langmuir* **1999**, *15*, 3386.

17. Z. H. Ju, R. P. Wei, X. P. Gao, W. S. Liu, C. R. Pang, *Opt. Mater*. **2011**, *33*, 909.

CHAPTER THREE

MECHANICAL PROPERTIES OF 3D-SINGLE LAYER II-VI BASED HYBRID SEMICONDUCTORS

Organic modules in II-VI hybrid compounds play an important role in tuning properties such as thermal expansion, thermal conductivity and mechanical properties.[1] In hybrid materials which are formed from the combination of two distinct components, contribution from each component and integration of their individual properties may lead to unique and enhanced properties and new functionalities. Inorganic binary phases of II-VI semiconductors have superior optical, magnetic and electric properties and are usually structurally rigid and stable. On the other hand, organic molecules are light and flexible. This chapter examines the effect of organic amines on the mechanical properties of the 3D II-VI based hybrid structures and shows how introducing the organic molecules to the inorganic structures can make the materials more flexible and more processable.[1]

3.1 Introduction to mechanical properties

When materials are being used in different applications, usually they are subjected to forces or loads. It is possible to calculate those forces and measure how the materials behave, deform or break, under the applied load or stress. Mechanical behavior is an important property that measures how flexible and deformative a substance is under different type of stress.[2] Mechanical properties can be tested by different ways such as compression, extension, shear and flexure, from which the elastic or inelastic behavior and properties of materials under the load or stress may be estimated.[2] To select a right material for desired applications, it is necessary to examine the stresses and strains that occur inside the materials that deform under loads. Stress-strain curves can be used to analyze mechanical properties of materials and to characterize the behavior of material tested. Mechanical properties of materials can be determined from the shape of their stress-strain

curve. For example, stress-strain curve with a concave up shape, in which there is no tangent point, identifies materials that fracture before they yield.

Among properties that can be determined by the stress-strain curve are toughness, harness and stiffness of material.[2] While stress is defined by force applied to a unit of area of surface, strain describes the deformation and displacement of the material under the stress relative to the reference length. Strain measures the ratio of the change in length relative to the original length. Deformation is reversible in the elastic materials, meaning that deformation can be recovered when the stress is removed but in plastic materials deformation is irreversible.[2] Toughness measures the amount of force requires to deform a material to its breaking point. Materials are tough if they can absorb large amount of energy before they fracture. It is the area under the stress-strain curve. Hardness measures the resistance of materials to an irreversible deformation. A material is stiff if it resistant to deform or bend under load and it can be measured by measuring the slope of the stress-strain curve. Lower the slope meaning that materials are more flexible and less stiff. [2]

Compressive strength of materials can be measured by applying force perpendicular to the area that is being measured.[2] By applying force to a material, its atoms are forced together, and this distracts the equilibrium distance that exists between the atoms in the solid therefore, atoms try to oppose this external force. This internal force that arises within the material can be defined as stress. Applying force beyond a material compressive strength will crush them. Compression tests examine the capacity of materials to tolerate axial pushing forces.

Organic materials are usually lighter and more flexible than inorganic compounds. As a result, crystalline hybrid semiconductors are expected to be lighter and substantially

more flexible than their inorganic counterparts. To investigate the effect of organic amine on the mechanical properties of the II-VI, crystal structure of series of 3D-ZnTe(L)$_{0.5}$ made of ZnTe single-atomic slabs and diamines, were studied.

3.2 Structure of 3D-α-ZnTe(L)$_{0.5}$

3D-α-ZnTe(L)$_{0.5}$ where L is organic amines (*hdz, en, pda, bda,* and *had*) structures are composed of single-atomic ZnTe slabs interconnected via diamine molecules by Zn-N coordinative bonds. Each zinc atom bonds to three tellurium atoms. Zn atom completes its tetrahedral conformation by binding to one nitrogen atom from the alkyldiamine molecule. Each tellurium atom connects to three neighboring zinc atoms. A puckered six-member rings which is extended in two dimensions is formed by alternating zinc and tellurium atoms (**Fig. 1.2**). α-ZnTe(*hdz*)$_{0.5}$ and α-ZnTe(*en*)$_{0.5}$ crystallize in orthorhombic, space group *Pbca* while ZnTe(*pda*)$_{0.5}$ crystallizes in *Cmc*2$_1$ space group. α –ZnTe(*bda*)$_{0.5}$ and α -ZnTe(*hda*)$_{0.5}$ are isostructural and both crystallize in the orthorhombic space group *Pbca*.[1a, 3]

3.3 Experimental

3.3.1 Synthesis and sample preparation

Solvothermal method was used to synthesize the single-layer 3D-α-ZnTe(L)$_{0.5}$ structures. The solid starting materials were weighted and added to the 23ml acid diestion bomb. Then amines, which act both as a solvent and as a reactant, were added to the mixture. The bombs were then heated in an oven at the desired temperature. After few days

of heating, the bombs were cooled down to room temperature and the final products were washed with ethanol and distilled water followed by drying at 60 °C at the vacuum oven. $ZnTe(en)_{0.5}$ was obtained from the reaction of $ZnCl_2$ (0.272g, 2 mmol), Te (0.128g, 1 mmol) and ethylenediamine (6 mL) at 200 ˚C for 3 days. Colorless thin plate-like crystals of $ZnTe(pda)_{0.5}$ were obtained by reaction of Zn $(NO_3)_2 \cdot 6H_2O$ (0.595g, 2 mmol), Te (0.127g, 1mmol) and 1,3-propanediamine (5mL) at 200 °C for 3 days. Reaction of ZnF_2 (0.207g, 4mmol), Te (0.127g, 1mmol) and 1,4-butanediamine (6mL) at 200 °C for 4 days afforded colorless plate-like crystals of $ZnTe(bda)_{0.5}$. α-ZnTe $(hda)_{0.5}$ was prepared through reaction of ZnF_2 (0.206g, 2mmol), Te (0.127g, 1mmol) and 1,6-hexanediamine (*hda*, 8mL) at 200 °C for 5 days.

3.3.2 Methods

Disks (pellets) of 13 mm in diameter and 0.5-0.8 mm were made by pressing the powders in the 13 mm diameter dye using the Caver laboratory press and load of 3.8 tons (applied pressure of 2500 psi) (**Fig. 3.1**). The data file was exported to Kaleida Graph where the data were extracted to produce a stress/strain curve.

Compression method was used to test the mechanical properties of selected II-VI-based hybrid. Measurements were performed on pellet samples prepared from polycrystalline powders. The mechanical analysis was performed on a PE DMA 7e with TAC 7/DX instrument controller. For data collection we used the PE Pyris version 3.81 software on a Dell Optiplex GX110 computer. Static stress of 1 Pa to 60kPa was applied on pellets at the rate of 3kPa/min. The experiments were performed at a constant temperature of 22 °C.

3.4 Results

The compressive strength of some selected 3D-structures of II-VI hybrid compounds was tested and the stress/strain profile of the samples in the low pressure range are shown in **Fig. 3.1** for ZnTe(L)$_{0.5}$, with *L, hdz, en, pda, bda*, and *hda*, in comparison with three reference samples, ZnTe, pentacene, and polystyrene prepared in the same manner. The stress–strain curve shows that as the length of amine chain in the ZnTe(L)$_{0.5}$ series of samples increases, materials become more flexible and less stiff. ZnTe(*en*)$_{0.5}$ with the shortest organic chain is the least flexible one and have a similar behavior as organic pentacene. Comparing the stress-strain curve of hybrid materials to that of the parent structure, ZnTe, suggests that introduction of the organic linear amines is responsible for the increase in flexibility of the hybrids. Introduction of organic amines decrease the density of the material and increase in the strain and deformation, therefore materials become less brittle and more flexible.

ZnTe(*hda*)$_{0.5}$, whith the longest organic chain in the series, is the most flexible one in the series and it shows larger strain than polystylene under the same amount of load. The image in **Fig. 3.2** demonstrates the extend of flexibility of ZnTe(*hda*)$_{0.5}$ by showing the bending capability of the free-standing film of 25 micron thick.

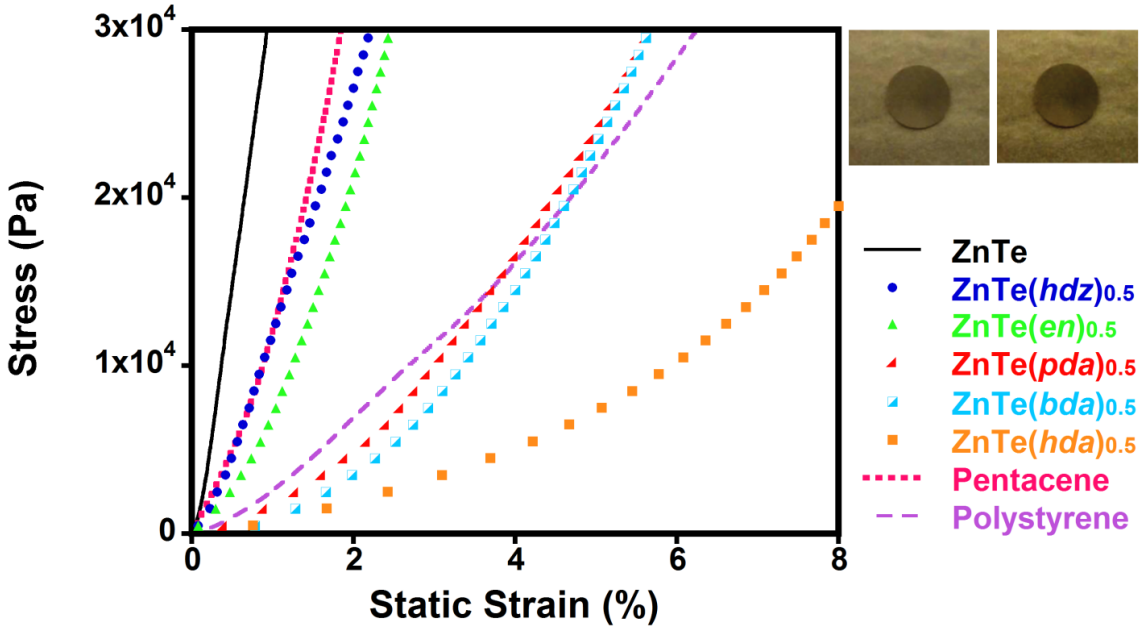

Figure 3.1 Stress–strain plots for the α-ZnTe(L)$_{0.5}$-type hybrid structures in comparison with three reference materials. Insets: two pellets (α-ZnTe(*en*)$_{0.5}$ and α-ZnTe(*pda*)$_{0.5}$).

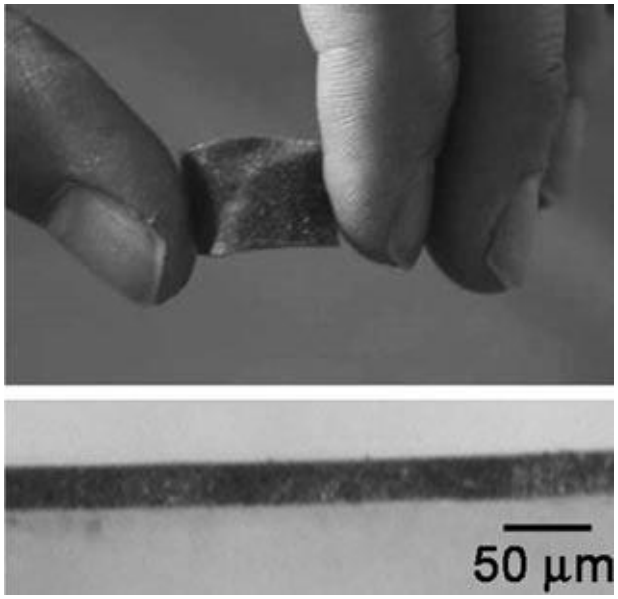

Figure 3.2 Top: A free-standing film specimen made from a powder sample of ZnTe(*hda*)$_{0.5}$. Bottom: side view of the film. The thickness of the film is about 25 mm.

3.5 Conclusions

In summary, unique type of inorganic–organic hybrid semiconductor material composed of covalently bonded ZnTe single-atomic slabs and long-chain organic alkyldiamines is synthesized. The structure of these hybrid materials is significantly more flexible than the inorganic parent structure (ZnTe). Introduction of organic amine enhances the flexibility of the material and as the length of amine's chains increases, materials become lighter and more flexible. Utilization of hybrid semiconductors of this type in low-weight and flexible optoelectronic devices may well become a future possibility.

3.6 References

1. a) X. Y. Huang, M. Roushan, T. J. Emge, W. H. Bi, S. Thiagarajan, J. H. Cheng, R. G.Yang, J. Li, *Angew. Chem. Int. Ed.* **2009**, 48, 7871; b) J. Li, W. Bi, W. Ki, X. Huang, S. Reddy, *J. Am. Chem. Soc.*, **2007**, *129* (46), 14140.

2. a) L. E. Nielsen, R. F. Landel, *Mechanical Properties of Polymers and Composites*, 2nd Ed. Marcel Dekker Inc, **1994**; b) F. Beer, R. Johnston, J. Dewolf, D. Mazurek, *Mechanics of materials*. New York: McGraw-Hill **2009**; c) M. Nic, J. Jirat, B. Kosata, B., eds. *"Modulus of Elasticity (Young's Modulus)*". *IUPAC Compendium of Chemical Terminology* (Online Ed.) **2006**, ISBN 0-9678550-9-8; e) E. Bodros, *Composite Part A* **2002**, *33 (7)*, 939.

3. a) C.Y. Moon, G.M. Dalpian, Y. Zhang, S.H. Wei, X.Y. Huang, J. Li, *Chem. Mater.* **2006,** *18*, 2805; b) X.Y. Huang, J. Li, *J. Am. Chem. Soc.* **2000,** *122*, 8789; c) X.Y. Huang, J. Li, Y. Zhang, A. Mascarenhas, *J. Am. Chem. Soc.* **2003**, *125*, 7049.

CHAPTER FOUR

SYNTHESIS AND CHARACTERIZTION OF V-VI BASED HYBRID SEMICONDUCTORS

Semiconductors such as Sb_2S_3 , Sb_2Se_3 and Bi_2S_3 with the direct band gap of 1.7-2.2 eV,[1] 1.13-1.15 eV,[2] and 1.3-1.7 eV[3] respectively, have received much attention due to their switching effects, thermoelectric and photovoltaics properties with important applications in TV cameras with photoconducting targets, interference filters and different photonic and optoelectronic devices.[1-3] Studies have shown that incorporation of organic ligands between the semiconductor layers reduces the thermal conductivity and as a result gives rise to an increase in the figure of merit, a parameter that characterizes the effectiveness of thermoelectric devices.[4] It also leads to the quantum confinement which in turn enhances the Seebeck coefficient by increasing the local density of states per unit volume near the Fermi level.[4,5] In addition, enhancement of the absorption coefficient in the inorganic-organic materials makes them suitable for use in optoelectronic as well as photovoltaic devices.[6]

A large number of thioantimonate[7-9] and few selenoantimontae[10-11] compounds containing organic amines have been reported. Majority of the reported structures contain negatively charged $[SbQ]^{z-}$ and positively charged organic amines. Introducing the transition metals results in the formation of an anionic antimony-chalcogenide framework with a charge balancing cationic transition-metal complex such as $[Co(dien)_2]_2Sb_2Se_6$, and $[Ni(dien)_2]_2Sb_2Se_5$.[10a] There are also few reports on the incorporation of the transition metals into main group metal sulfide or selenide framework.[8c,10b] There are also many examples of hybrid compounds containing only thioantomonates frameworks, with organic amines perpendicular to the layers, e.g.$(paH)_2Sb_4S_7$,[9d] or parallel to them, e.g. (trans-1,4-$C_6N_2H_{15})Sb_3S_5$.[9a] However, hybrid compounds with selenoanitimonates framework

without any transition metals are less explored and there is no, or only very few, examples may be found in the literature.

In an effort to develop new types of metal chalcogenides with particular properties, series of new inorganic-organic hybrid materials based on V-VI semiconductors have been synthesized and their optical, thermal and electrical properties were measured. The ability to tune the optical, electrical, and thermal properties of such organic-inorganic hybrid nanostructures makes them highly versatile materials for a range of energy generation and conversion devices.

4.1 (Sb_2Se_3)(Sb_3Se_5)(*dien*H) (1)

4.1.1 Synthesis

Sb (99.5%, Strem), Se (99.5%, Strem), Diethylentriamine(dien)(99%, Alfa Aesar) were obtained commercially and used without further purification. Solvothermal method was used for the synthesis. Mixture of elemental Sb (2mmol, 243.5mg) and Se (3mmol, 236.8mg), in diethylentriamine (*dien*) (8ml) were loaded in a Teflon-lined acid digestion bombs and the sealed containers heated at 150 ˚C for 7 days. This reaction was resulted in the formation of the dark needle type crystals of (Sb_2Se_3) (Sb_3Se_5) (*dien*H) **(1)** with a yield of 60% based on Ss. The final products were collected and washed with 95% ethanol and water and dried at 50 ˚C vacuum oven for 10 minutes. While no product was formed at temperature lower than 150 ˚C, using higher temperature resulted in the formation of binary phase of Sb_2Se_3.

4.1.2 Structure

Crystal of compound **1** with a moiety formula of $(Sb_2Se_3)(Sb_3Se_5)(C_4H_{14}N_3)$, crystallizes in monoclinic space group *P2₁* (**Table 4.1**). ORTEP diagram and pxrd pattern of $(Sb_2Se_3)(Sb_3Se_5)$(dien) are shown in **Figure 4.1** and **Figure 4.2** respectively. The structure consists of 1-D arrays of Sb-Se along the needle b-axis (**Fig. 4.3**), there are two unique arrays in the bc plane, namely the neutral $\{Sb_4Se_6\}_\infty$ (array A) and the charged $\{(Sb_3Se_5)^-\}_\infty$ (array B), that alternate in the …ABBABBABB… fashion (**Fig. 4.3**). The diffraction data appeared to be nearly centrosymmetric and choice of space group, $P2_1$, rather than $P2_1/m$ required the use of near racemic twinning (53:47 ratio), but based upon a Hamilton wR factor ratio analysis, the twinned noncentrosymmetric case used here was statistically preferred over the centrosymmetric choice. One Sb site has a twofold positional disorder of about 0.5 Å, but still gives the typical 1 short (~2.6 A) and 4 long (2.7 – 3.1 A) bonds for either Sb at that site, as also found for the other two 5-coordinate Sb atoms, with short (2.57, 2.59Å) and longer (2.7 – 3.1Å) Sb-Se bonds (**Fig. 4.4a**). The structure is consisting of the corner sharing $SbSe_3$ pyramids, such that Sb_4Se_6 and Sb_3Se_5 secondary units form by joining of 2 or 3 $SbSe_3$ pyramids, respectively (**Fig. 4.4a**). Propagation of these secondary building units results in the formation of 1D-chains alongthe b axis (**Fig. 4.4b**), containing 3-coordinate Sb (in addition to the 5-coordinate Sb described above) with Sb-Se distances in the range 2.58-2.67 Å and longer Sb-Se distances in the range 2.93-3.26 Å (**Table 4.2**). The next two nearest Se atoms for Sb (1), Sb(2) and Sb(4) are located in the chains in the neighboring sheets with Sb-…Se distances of 3.6 – 4.0 Å, which are slightly less than sum of the van der Waals radii of Sb-Se (4.20 Å) but greater than the covalent radii sum of 2.78Å for Sb^{3+} and Se^{2-}, respectively, indicative of a

weaker, dative bond or interaction. There is a relatively wide (~7Å) separation between the 1-D arrays of Sb and Se, and it contains sites of twofold disordered diethylenetriiminium cations (dien) (**Fig. 4.5**). **S**tructure of the parent structure, Sb_2Se_3 **(Fig 4.6)**, with 1-D arrays of $\{Sb_4Se_6\}_\infty$,[12] is analogous to array in compound **1** (**Fig. 4.5**). **Table 4.3** compare the Sb-Se bond distances of (Sb_2Se_3) (Sb_3Se_5) (*dien*H) with Sb_2Se_3.

Table 4.1 Crystal and structure refinement data for compound **1.**

formula	C4 H14 N3 Sb5 Se8	**T (K)**	100(2)
fw	1344.61	**Z**	2
crystal system	Monoclinic	**D_{cal} (mg/m^3)**	4.565
space group	P2(1)	**total reflns**	11669
a (Å)	13.7477(12)	**Unique reflns**	5915
b (Å)	3.9545(4)	**F (000)**	1172
c (Å)	18.3057(16)	**R1[*I* >2σ(*I*)]**	0.0301
α (deg)	90	**wR2[all data]**	0.0656
β (deg)	100.628(2)	**GOF**	1.003
γ (deg)	90	**T (K)**	100(2)
***V* (Å^3)**	978.12(16)		

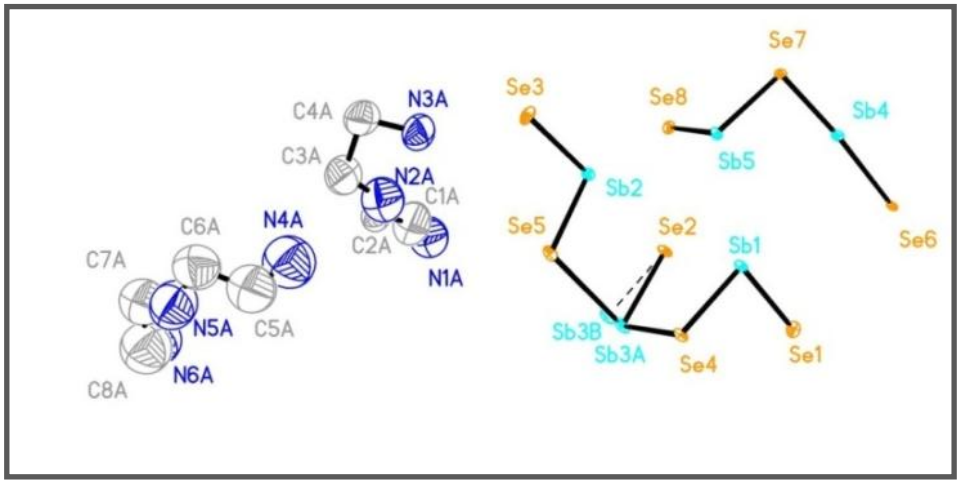

Figure 4.1 ORTEP diagram of (Sb_4Se_6) (Sb_3Se_5)(dien).

Table 4.2 Selected bond distances (Å) and angels (deg) for compound **1**.

Sb(1)-Se(4)	2.5701(5)	Sb(3B)-Se(2)	2.5388(13)
Sb(1)-Se(1)#1	2.693(2)	Sb(3B)-Se(5)#2	2.694(3)
Sb(1)-Se(1)	2.706(2)	Sb(3B)-Se(5)	2.729(4)
Sb(1)-Se(2)#1	3.1178(19)	Sb(3B)-Se(4)#2	3.075(3)
Sb(1)-Se(2)	3.1281(19)	Sb(3B)-Se(4)	3.112(3)
Sb(2)-Se(5)	2.5852(5)	Sb(4)-Se(6)#3	2.5889(5)
Sb(2)-Se(3)	2.654(2)	Sb(4)-Se(7)	2.796(2)
Sb(2)-Se(3)#2	2.672(2)	Sb(4)-Se(7)#2	2.810(2)
Sb(2)-Se(2)	3.261(2)	Sb(4)-Se(6)#1	2.933(2)
Sb(2)-Se(2)#1	3.267(2)	Sb(4)-Se(6)	2.948(2)
Sb(3A)-Se(2)	2.5502(14)	Sb(5)-Se(7)	2.6221(5)
Sb(3A)-Se(4)	2.712(3)	Sb(5)-Se(8)#1	2.640(2)
Sb(3A)-Se(4)#2	2.732(4)	Sb(5)-Se(8)	2.652(2)
Sb(3A)-Se(5)	3.071(4)	Sb(5)-Se(6)#4	3.2560(19)
Sb(3A)-Se(5)#2	3.094(3)	Sb(5)-Se(6)#3	3.2674(19)
Se(4)-Sb(3A)-Se(5)	93.92(13)	Se(1)-Sb(1)-Se(2)	93.33(7)
Se(4)-Sb(1)-Se(1)	93.07(5)	Se(2)-Sb(2)-Se(2)#1	74.573(14)
Se(4)-Sb(1)-Se(2)	83.67(4)	Se(2)-Sb(3A)-Se(4)	93.15(9)
Se(4)#2-Sb(3B)-Se(4)	79.46(3)	Se(2)#1-Sb(1)-Se(2)	78.564(15)
Se(5)-Sb(2)-Se(3)	93.10(6)	Se(2)-Sb(3B)-Se(5)	92.44(9)
Se(5)-Sb(2)-Se(2)	80.33(4)	Se(6)#3-Sb(4)-Se(7)	88.77(5)
Se(5)-Sb(3A)-Se(5)#2	79.80(3)	Se(6)#1-Sb(4)-Se(6)	84.516(15)
Se(5)#2-Sb(3B)-Se(5)	93.64(4)	Se(7)-Sb(5)-Se(8)	91.41(5)
Se(3)-Sb(2)-Se(3)#2	95.887(19)	Se(7)#2-Sb(4)-Se(6)	92.24(7)
Se(3)#2-Sb(2)-Se(2)	94.39(7)	Se(8)-Sb(5)-Se(6)#3	93.45(6)

Table 4.3 Sb-Se bond distances of inorganic phase of Sb_2Se_3 and $(Sb_2Se_3)(Sb_3Se_5)$(*dien*H) hybrid phase.

Sb-Se distance	**Sb_2Se_3**	**(Sb_2Se_3) (Sb_3Se_5) (*dien*H)**
within same chain	2.57-2.77 (Å)	2.55-2.81(Å)
	3.22-3.79(Å)	2.93-3.26(Å)
nearest pairs of chains	2.98(Å)	2.94(Å)
between chains in neighboring sheets	3.46-3.74(Å)	3.69-3.82 (Å)

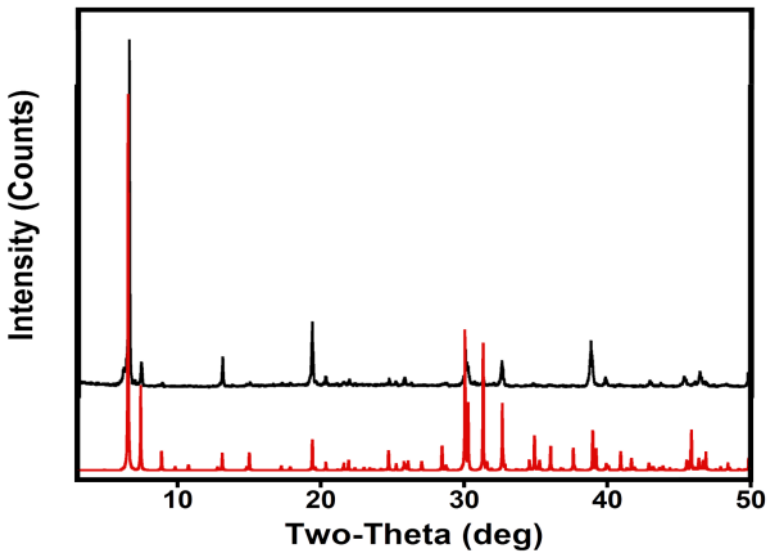

Figure 4.2 Observed (black) and stimulated (red) PXRD patterns (Sb_4Se_6) (Sb_3Se_5) (*dien*H).

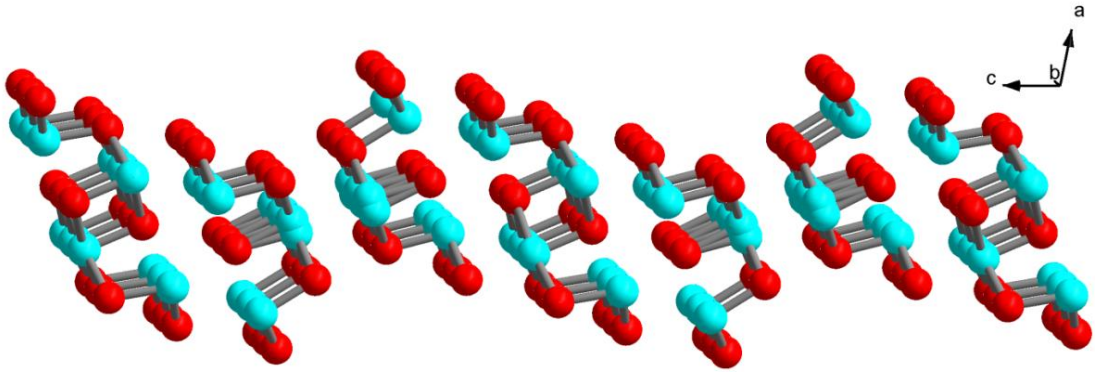

Figure 4.3 View of packing of 1D-arrays of Sb_2Se_3 and Sb_3Se_5 chains in compound 1 along the b axis.

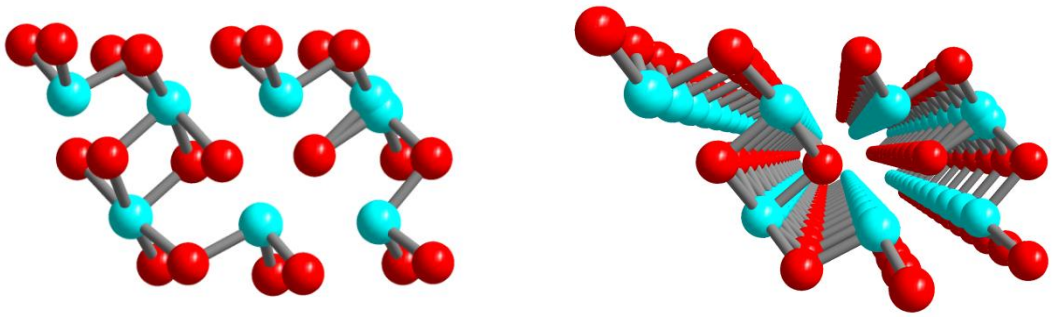

(a) **(b)**

Figure 4.4 (a) Building unit of compound **1**, showing the connectivity of $SbSe_3$ units to form Sb_2Se_3 and Sb_3Se_5, (b) View of 1D-chains along the b axis.

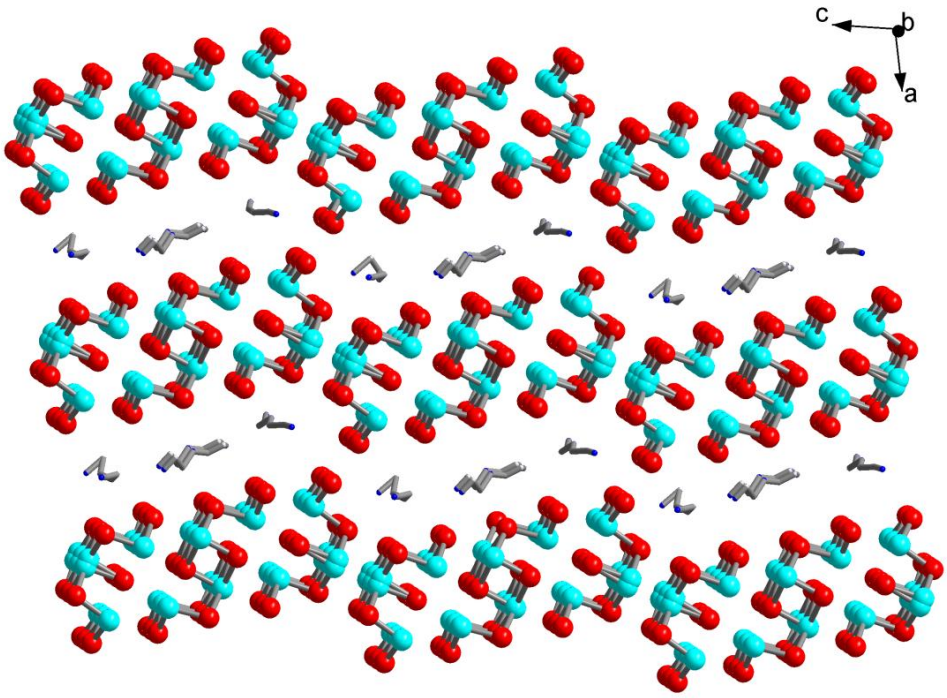

Figure 4.5 View of the structure of **1** along b axis, showing the location of *dien* molecules. Antimony atoms are represented by cyan, Selenium by red, Nitrogen by dark blue and Carbons by grey.

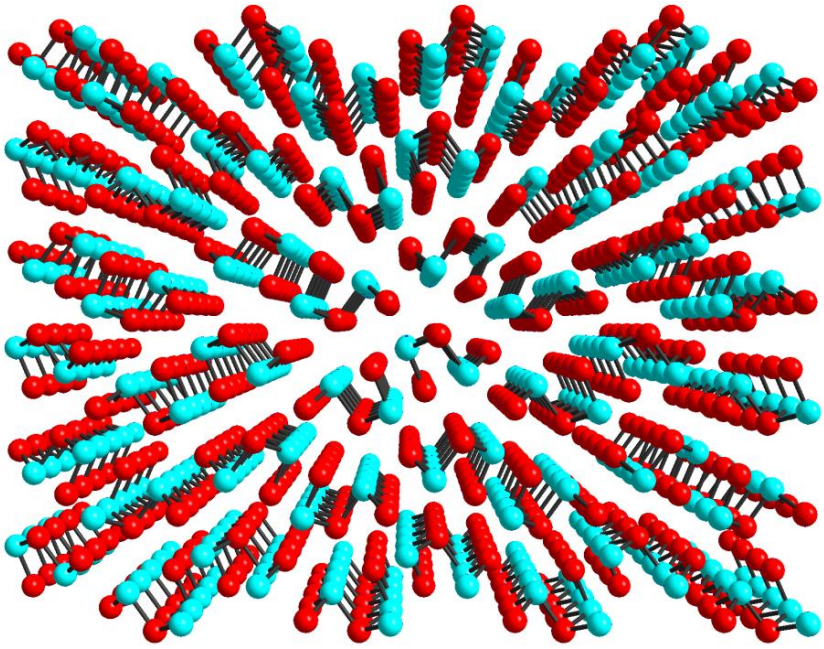

Figure 4.6 Structure of Sb_2Se_3 along the c axis. Sb atoms are blue and Se are red.

4.1.3 Properties

Thermal properties: Themegravimetric analysis (TGA) was performed to study the thermal stability and to determine the composition of the compounds. About 10 mg of sample was loaded onto a platinum sample pan and heated from room temperature to 600 °C at a rate of 4 °C/min under nitrogen flow. Crystal structure was stable up to 80 ˚C and showed a weight-loss of 8.9% in two steps (**Fig. 4.7**) which is slightly higher than what is expected for the emission of amine molecule (calculated: 7.67%). PXRD of the compound after the initial weight-loss shows the reflections of Sb_2Se_3 in the residue of the samples. Final decomposition occurs after 400 ˚C.

Optical properties: Optical absorption spectra were measured at room temperature on a Schimadzu UV-3600 UV/VIS/NIR spectrometer. The reflectance data were used to estimate the band gap using Kubelka-Munk function, $\alpha/S = (1-R)^2/2R$, where α is the absorption coefficient, S is the scattering coefficient and R is the reflectance. Compound **1** has an optical band-gap of ~0.9eV which is very close to that of the binary phase of Sb_2Se_3 (**Fig.4.8**). Arrangement of organic amines parallel to the inorganic chains in the structure of compound **1**, don't have a significant contribution to the interaction between the chains. As a result, quantum confinement due to the incorporation of organic spacer is negligible and blue-shift in a band-gap is not observed.

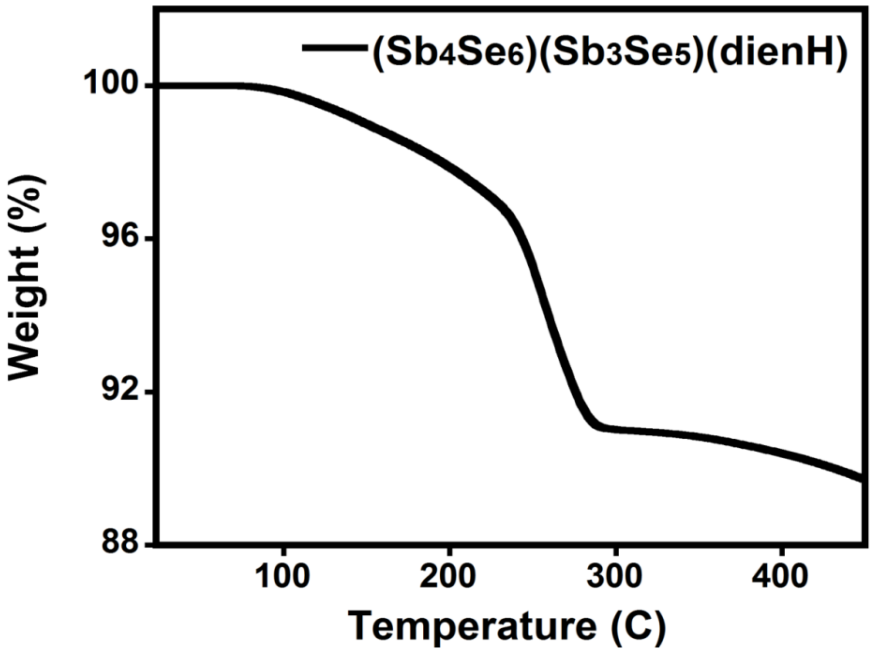

Figure 4.7 TGA data showing weight losses of 8.9% for $(Sb_2Se_3)(Sb_3Se_5)$(*dien*H).

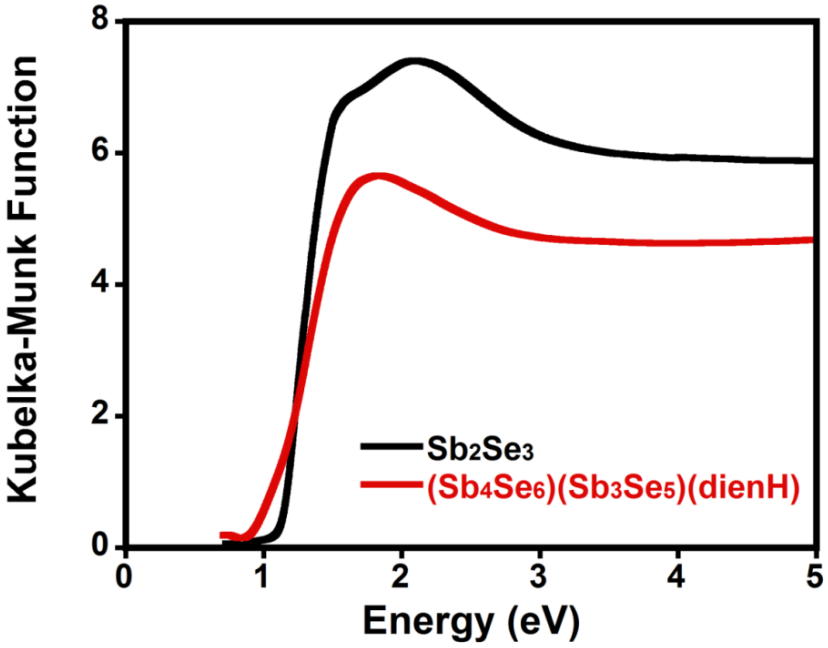

Figure 4.8 Room temperature optical absorption spectra of $(Sb_2Se_3)(Sb_3Se_5)$(*dien*H) compare to that of the Sb_2Se_3 structure.

Electrical conductivity: Powder samples of compound **1** was pressed into pellets with the thickness ranging 80-120 micron using a Caver laboratory press under a load of 3.8 tons (2500 atm pressure) (**Fig. 4.9**). Gold contacts were evaporated on these pellets and they were used for electrical conductivity measurements. I-V curves were obtained by applied voltage in a range of -1 to 1 V with 0.1 V incremental steps (**Fig. 4.10**). Resistivity was calculated using the equation $\rho = R.d.a/b$ where d is the film thickness, b is the distance between the contacts, a is the length of the contacts, and R is resistance which was obtained from the slope of the linear fit to I-V curves. Compound **1** shows the electrical resistivity of 2.7×10^7 Ωcm which is higher than that of the inorganic Sb_2Se_3 which was used as a reference ($\rho = 7 \times 10^5$ Ωcm). This higher resistivity is expected and is due to existence of organic molecules, with very low conductivity in the structure.

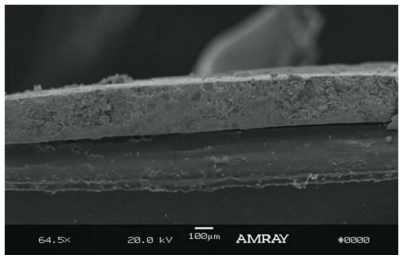

Figure 4.9 SEM image showing the thickness (~200micron) of the film of $(Sb_4Se)(Sb_3Se_5)$(*dien*H) used for the I-V measurements.

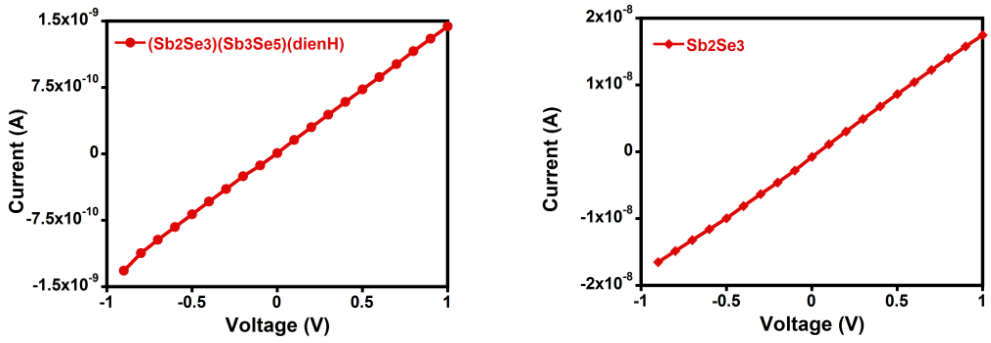

Figure 4.10 I-V curve for a) $(Sb_4Se)(Sb_3Se_5)$(*dien*H), and b) Sb_2Se_3.

Thermal conductivity: For the thermal conductivity measurements powders were pressed to the pellets with diameter of 10mm and thickness of 1-1.5mm. Pellets were made under a load of 3.8 tons and annealed at 60 °C for 1 hour. Sb_2Se_3 Pellet was prepared using the same condition and was used as a reference material. The thermal diffusivity, specific heat and density of the samples were measured in the temperature range 25 °C to 100 °C first and then thermal conductivity was calculated using the following equation: $\kappa = \rho\alpha C_p$, where κ is the thermal conductivity, ρ is the density, α is the thermal diffusivity, and Cp is the specific heat of the material.

Specific heat capacity in $(Sb_2Se_3)(Sb_3Se_5)$(*dien*H) increases while there is a slight decrease in thermal diffusivity (**Fig. 4.11**).This leads to a net increase in thermal conductivity with temperature. Thermal conductivity shows an increase up to 70°C and then drops (**Fig. 4.12**). $(Sb_2Se_3)(Sb_3Se_5)$(*dien*H) sample shows a lower thermal conductivity compare to that of a Sb_2Se_3 (**Fig. 4.12**). Decrease in thermal conductivity of hybrid compound is probably due to phonon scattering[13] Disorder in organic-inorganic interfaces can act as scattering centers and these disorders plus interface roughness lead to phonon scattering. Reduced thermal conductivity of the hybrid compounds compare to that of the pure inorganic phase can also be the result of acoustic mismatch between the two phases. Differences in densities and sound speeds in organic and inorganic phases leads to a mismatch in the acoustic impedances thus interface reflection can occur which in turn reduces the thermal conductivity.[13]

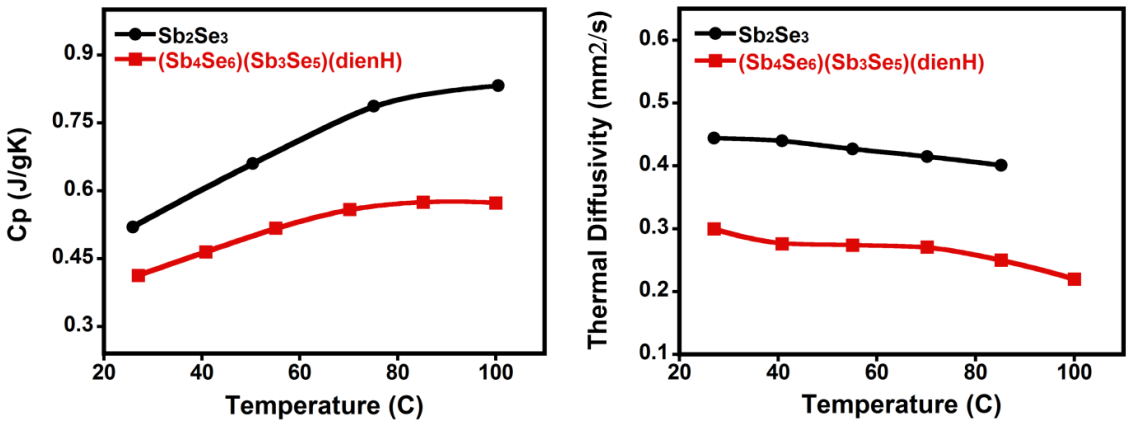

(a) **(b)**

Figure 4.11 (a**)** Specific heat, (b) thermal diffusivity plots for $(Sb_4Se)(Sb_3Se_5)$(*dien*H) in comparison with Sb_2Se_3 as a reference material.

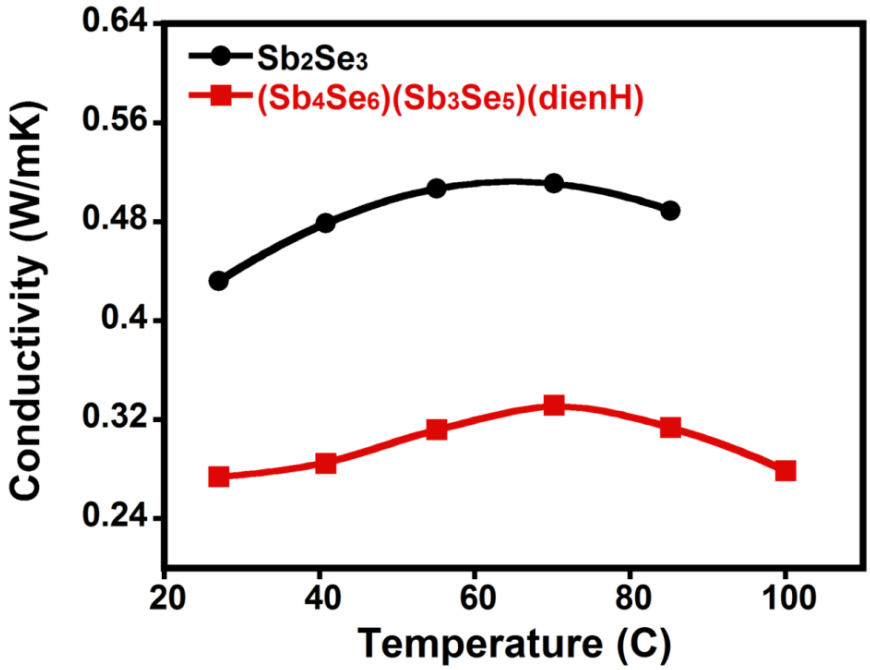

Figure 4.12 Thermal conductivity plots for $(Sb_4Se)(Sb_3Se_5)$(*dien*H), in comparison with Sb_2Se_3 as a reference material.

4.2 (Sb_3Se_5)(*hda*H) (2)

4.2.1 Synthesis

Plate-type crystals of **2** were obtained by reaction of Sb (2mmol, 243.5mg) and Se (3mmol, 236.8mg) in 1,6-diaminohexane (*hda*) (8ml) at 150 ˚C for 7 days. The yield was about 50%. Excess of solvents was discarded via filtration and the obtained crystals were washed with water and ethanol and dried at 50 ˚C vacuum oven for 15 minutes.

4.2.2 Structure

Compound **2** crystallizes in orthorhombic space group *Pbcm* (**Table 4.4**). Its PXRD and ORTEP diagram is shown in **Figure 4.13,** and **4.14**, respectively. The structure of compound **2** consists of protonated hda cations (hdaH+) and interacting ionic chains $\{(Sb_3Se_5)^-\}_\infty$ anions, the latter forming 2-D sheets. The organic cations alternate with the inorganic anionic layers in a sandwich manner perpendicular to *a* axis (**Fig. 4.15**). Both short (nine at 2.56 – 2.72 Å) and long (four at 3.11 – 3.31 Å) Sb-Se bonds are present in the structure, and somewhat longer ones (three at 3.24 – 3.33 Å) connect the chains to form the 2-D sheets (**Fig. 4.16 a, b, c**). Atom Sb (1) is centrally located and poised to connect chains into the 2-D sheets. In the anion sheet, there are three unique Sb atoms, 6-coordinate Sb(1), and 5-coordinate Sb(2), and Sb(3), forming square pyramidal [Sb(2) and Sb(3)] and square anti-prismatic [Sb(1)] polyhedral (**Fig. 4.16d**). All bond lengths and angles (**Table 4.5**) are in agreement with the reported values in the literature for Sb_xSe_y species.[10] Adjacent $Sb(2)Se_5$ square pyramids are connected via the Se(1)- Se(4) edge in much the same way as the adjacent $Sb(3)Se_5$ square pyramids are connected via the Se(1)-Se(5) edge (**Fig. 4.16 a, b, c**) . As a result, atoms Se (4) and Se (5) are 2-coordinate and

extend away from the anionic sheets and towards the region of the cations. The approximate thickness of the anionic 2-D layer is around 8Å, and these are separated by protonated linear iminium cations that run parallel to the b axis and are perpendicular to the $\{(Sb_3Se_5)^-\}_\infty$ anionic layers and nearly anti-parallel to adjacent cations in the space in between the anionic layers that are separated by about 10Å. As a result, the protonated "head" of one cation appears to form a hydrogen-bond to the "tail" of the laterally adjacent one. There does not appear to be any N-H...Se weak H-bonds here, and such contacts are not expected for these less rigid cation regions that alternate between rigid $\{(Sb_3Se_5)^-\}\infty$ sheets.

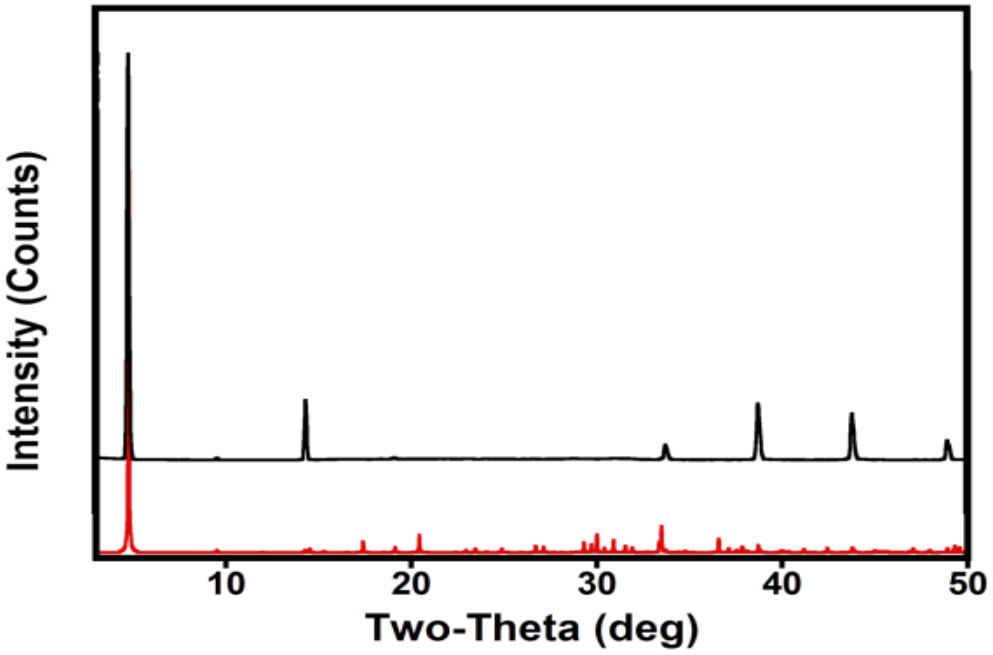

Figure 4.13 Observed (black) and simulated (red) PXRD patterns of (Sb_3Se_5) (*hda*H).

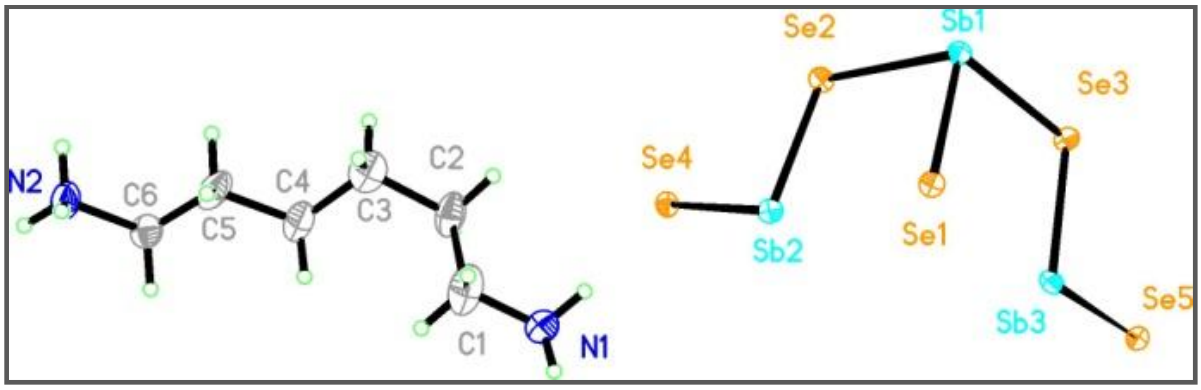

Figure 4.14 ORTEP diagram of (Sb_3Se_5)(*hda*H).

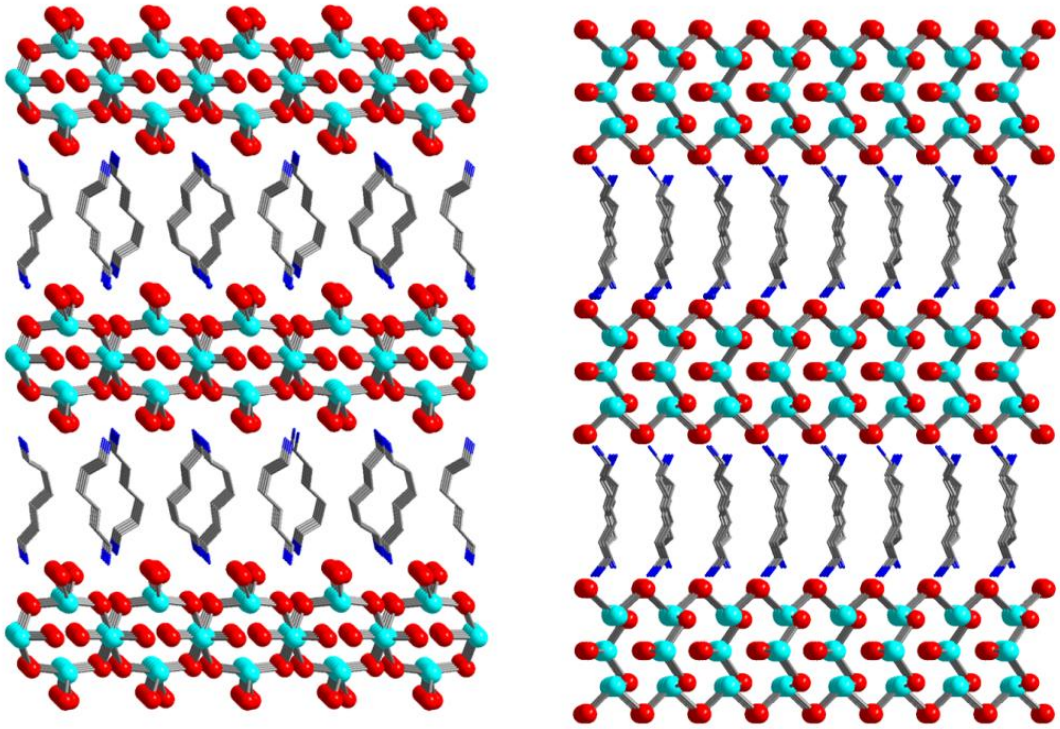

Figure 4.15 Structure of compound **2** showing the location of monoprotonated *hda* molecules, view along (a) c axis, and (b) along a axis. Antimony atoms are represented by cyan, Selenium by red, Nitrogen by dark blue and Carbons by grey.

Table 4.4 Crystal and structure refinement data for compound **2**.

formula	C6 H17 N2 Sb3 Se5	**T (K)**	100(2)
fw	877.27	**Z**	4
crystal system	Orthorhombic	**D_{cal} (mg/m^3)**	3.318
space group	Pbcm	**total reflns**	18313
a (Å)	12.1838(7)	**Unique reflns**	5302
b (Å)	18.5992(11)	**F (000)**	1560
c (Å)	7.7487(5)	**R1[I >2σ(I)]**	0.0562
α (deg)	90	**wR2[all data]**	0.1326
β (deg)	90	**GOF**	1.050
γ (deg)	90	***V*** **(Å^3)**	1755.92(18)

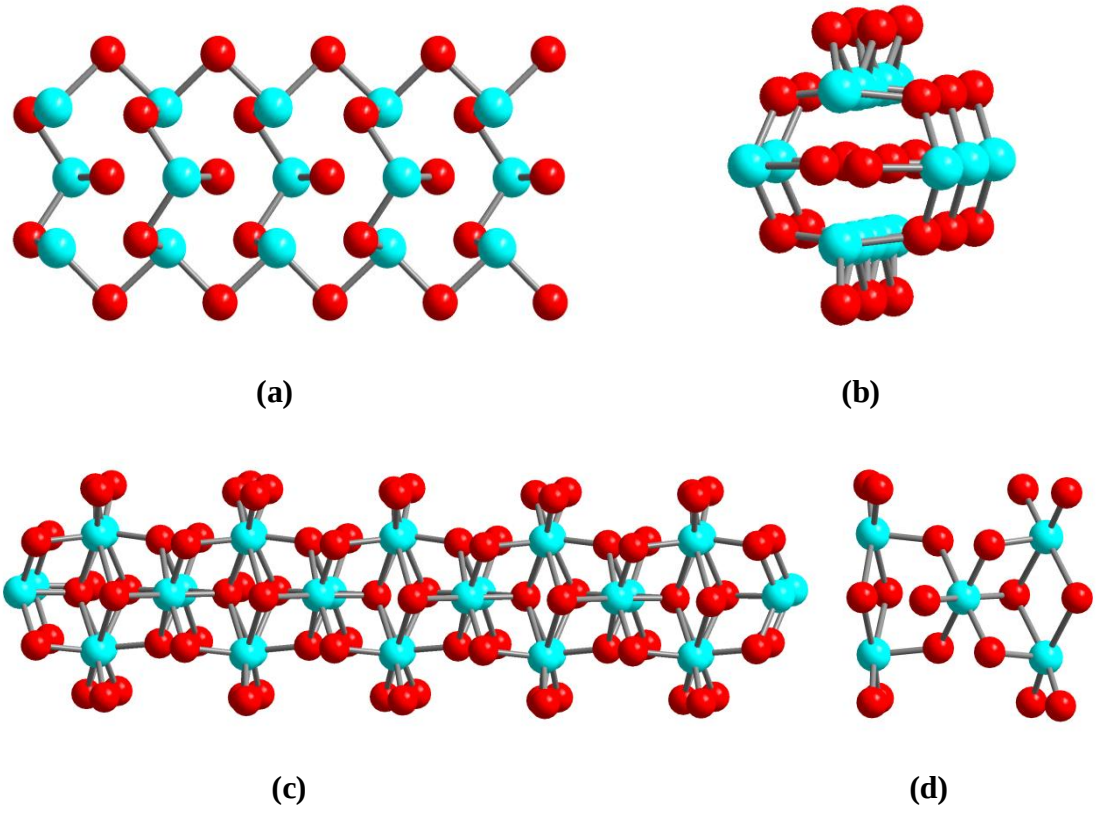

Figure 4.16 View of 1D-chains in **2**; showing the edge sharing of $Sb(2)Se_5$ square pyramids via the Se(1)-Se(4) edge and $Sb(3)Se_5$ square pyramids via the Se(1)- Se(5) edge, (a) along the a axis, (b) along the c axis. longer bonds are not shown for clarity, (c) 2D-anionic layers forming by further corner sharing of $SbSe_3$ units through bonding of Sb(1) from $Sb(1)Se_3$ chain to the Se(3) and Se(2) atoms of the pyramid from another chain, (d) building unit of compound 2 showing the connectivity of Sb atoms; 6-coordinate Sb(1), and 5-coordinate Sb (2), and Sb (3), forming square pyramidal [Sb(2) and Sb(3)] and square anti-prismatic [Sb(1)] polyhedral.

4.2.3 Properties

Thermal properties: Thermal stability of compound 2 was studied using TGA. About 10 mg of the sample was loaded onto a platinum sample pan and heated from room temperature to 600 °C at the rate of 4 °C/min under the nitrogen flow. Decomposition starts at 60˚C and the experimental two-steps weight-loss of 13.2% is in good agreement with the expected value (calc. 13.2%) for the loss of amine (*hda* molecule) (**Fig. 4.17**). Powder x-ray pattern of the compound after the initial weight-loss shows the reflections of Sb_2Se_3 in the residue of the sample. Final decomposition occurs after 400 ˚C.

Optical properties: (Sb_3Se_5)(*hda*H) has an optical band-gap of ~1.5eV which is blue shifted compare to the inorganic parent structure (**Fig. 4.18**). This increase in the band gap may be due to the arrangement of amine molecules between the layers. The *hda* molecules separate the layers from each other; therefore, it reduces the electron interactions between the Sb-Se chains in different layers. This reduction of the interaction between the inorganic layers leads to the confinement of electrons in the layers and as a result band-gap increases.

Electrical conductivity: Pellets with the thickness of 80-120 micron were prepared and gold contacts were deposited on them using the same procedure as used for compound **1** (**Fig. 4.19**). I-V curves were obtained by applied voltage in the range of -1 to 1 V with 0.1 V incremental steps (**Fig. 4.20**). Compound **2** shows a resistivity of 6.01×10^8 Ωcm which is higher than that of the compound **1** and that of the inorganic Sb_2Se_3 (10^3-10^4 Ωcm for single crystal, [14]and 10^6-10^7 Ωcm for the bulk and thin film).[14] This higher resistivity with respect to compound **1** is expected due to higher energy band-gap of compound **2**.

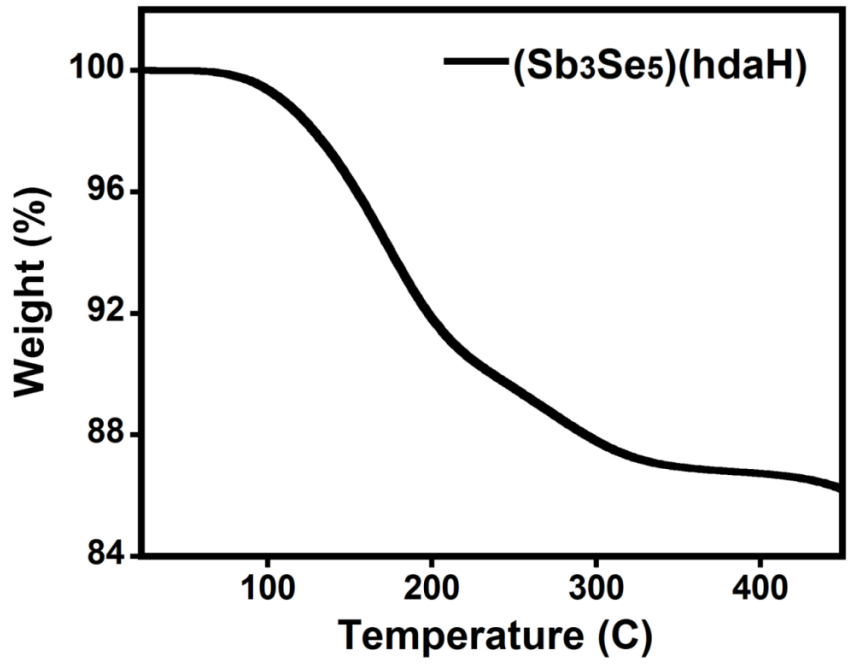

Figure 4.17 TGA data showing weight losses of 13.3 % for compound **2**.

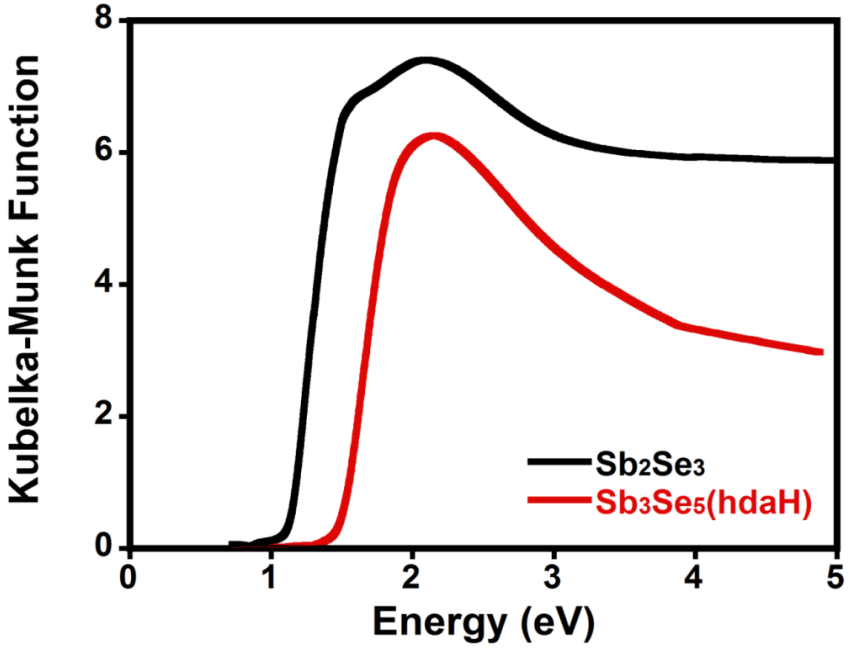

Figure 4.18 Room temperature optical absorption spectrum of (Sb_3Se_5)(*hda*H) compared to that of Sb_2Se_3.

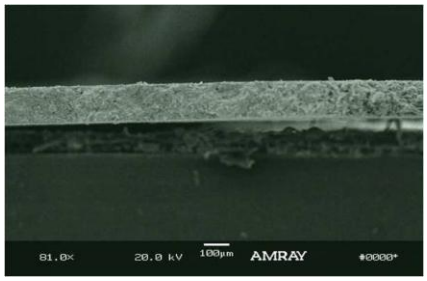

Figure 4.19 SEM image showing the thickness of film of (Sb_3Se_5)(*hda*H) that used for the I-V measurements. The thickness of the film is ~150micron.

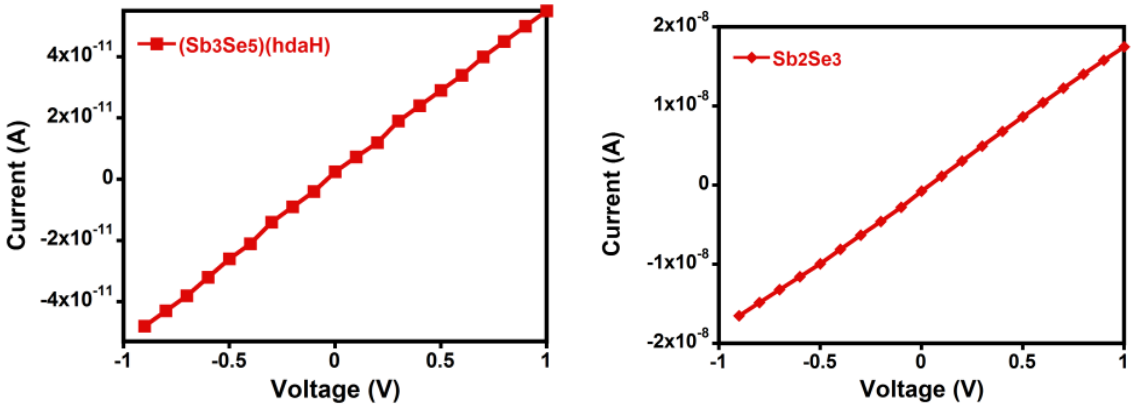

(a) **(b)**

Figure 4.20 I-V curve for (a) (Sb_3Se_5) (*hda*H), and (b) Sb_2Se_3.

Thermal conductivity: Pellets with diameter of 10mm and thickness of 1-1.5mm were used for thermal conductivity measurements. Pellets were prepared using the same condition as used for compound **1** and thermal diffusivity, specific heat and density of the samples were measured using the same process. Sb_2Se_3 pellet was used as a reference material. Thermal conductivity was calculated using $\kappa = \rho\alpha C_p$. As it is shown in **Figure 4.21a** specific heat capacity increases as a temperature goes up but there is no change in thermal diffusivity as a function of temperature (**Fig. 4.21b**). This leads to a net increase in thermal conductivity with temperature (**Fig 4.22**). Compound **2** has a lower thermal

conductivity compare to that of a Sb_2Se_3. Having lower thermal and electrical conductivity compare to compound **1** and Sb_2Se_3, shows that length and arrangement of organic molecule in the structure plays an important role in the conductivity of the materials. As discussed earlier, introducing the organic molecules to the structure leads to an increase in the phonon scattering which in turn reduce the thermal conductivity.[13]

Table 4.5 Selected bond distances (Å) and angels (deg) for compound **2**.

Sb(1)-Se(4)	2.5701(5)	Sb(3B)-Se(2)	2.5388(13)
Sb(1)-Se(1)#1	2.693(2)	Sb(3B)-Se(5)#2	2.694(3)
Sb(1)-Se(1)	2.706(2)	Sb(3B)-Se(5)	2.729(4)
Sb(1)-Se(2)#1	3.1178(19)	Sb(3B)-Se(4)#2	3.075(3)
Sb(1)-Se(2)	3.1281(19)	Sb(3B)-Se(4)	3.112(3)
Sb(2)-Se(5)	2.5852(5)	Sb(4)-Se(6)#3	2.5889(5)
Sb(2)-Se(3)	2.654(2)	Sb(4)-Se(7)	2.796(2)
Sb(2)-Se(3)#2	2.672(2)	Sb(4)-Se(7)#2	2.810(2)
Sb(2)-Se(2)	3.261(2)	Sb(4)-Se(6)#1	2.933(2)
Sb(2)-Se(2)#1	3.267(2)	Sb(4)-Se(6)	2.948(2)
Sb(3A)-Se(2)	2.5502(14)	Sb(5)-Se(7)	2.6221(5)
Sb(3A)-Se(4)	2.712(3)	Sb(5)-Se(8)#1	2.640(2)
Sb(3A)-Se(4)#2	2.732(4)	Sb(5)-Se(8)	2.652(2)
Sb(3A)-Se(5)	3.071(4)	Sb(5)-Se(6)#4	3.2560(19)
Sb(3A)-Se(5)#2	3.094(3)	Sb(5)-Se(6)#3	3.2674(19)
Se(4)-Sb(3A)-Se(5)	93.92(13)	Se(1)-Sb(1)-Se(2)	93.33(7)
Se(4)-Sb(1)-Se(1)	93.07(5)	Se(2)-Sb(2)-Se(2)#1	74.573(14)
Se(4)-Sb(1)-Se(2)	83.67(4)	Se(2)-Sb(3A)-Se(4)	93.15(9)
Se(4)#2-Sb(3B)-Se(4)	79.46(3)	Se(2)#1-Sb(1)-Se(2)	78.564(15)
Se(5)-Sb(2)-Se(3)	93.10(6)	Se(2)-Sb(3B)-Se(5)	92.44(9)
Se(5)-Sb(2)-Se(2)	80.33(4)	Se(6)#3-Sb(4)-Se(7)	88.77(5)
Se(5)-Sb(3A)-Se(5)#2	79.80(3)	Se(6)#1-Sb(4)-Se(6)	84.516(15)
Se(5)#2-Sb(3B)-Se(5)	93.64(4)	Se(7)-Sb(5)-Se(8)	91.41(5)
Se(3)-Sb(2)-Se(3)#2	95.887(19)	Se(7)#2-Sb(4)-Se(6)	92.24(7)
Se(3)#2-Sb(2)-Se(2)	94.39(7)	Se(8)-Sb(5)-Se(6)#3	93.45(6)

4.3 (Sb_7Se_{11})(*amp*H) (3)

4.3.1 Synthesis

Dark needle shape crystals with a yield of 50% were formed from the reaction of Sb (2mmol, 243.5mg) and Se (3mmol, 236.8mg) and 4-aminopyridine (4mmol) in DMF. Reaction was heated at 150 ˚C for 7 days. Powders were collected using the same procedure as the other two compounds.

4.3.2 Structure

Compound **3** crystallizes in monoclinic space group *C2/m* (**Table 4.6**). Similar to **1**, the structure of **3** is consist of negatively charged inorganic 1D-$\{Sb_7Se_{11}\}_\infty$ chain-like polymers, with organic cations in the channels (**Fig. 4.23a**). It is composed of 5-coordinated Sb atoms with both short and long Sb-Se bonds with the bond distance in the range of 2.5-3.2A. Sb_3Se_5 units are formed by three edge-sharing 5-coordinate square-pyramidal $SbSe_5$ (**Fig. 4.23b**). Two of these Sb_3Se_5 share a corner to form Sb_7Se_{11} chains. $\{Sb_3Se_5\}_2$, joined by one corner-sharing 6-coordinate octahedral Sb to another Sb_3Se_5 unit (**Fig. 4.23 c, d**). This is not unusual, and the wireframe projection view of the 5-coordinate Sb triplets look like the usual "double squares" of other $(Sb)_x(Se)_y$ in the Cambridge database. The 1D polymers are joined by dative Sb-Se bonds of about 3.6-3.8Å, but only between 5-coordinate Sb groups in adjacent chains, the 6-coordinate groups are only intrachain linkers. Organic amino pyridine cations are in the channels (clefts) between the 6-coordinate Sb octahedral in adjacent 1D chain. There is van der Waals or ionic interactions of the cations with the poly-anion chains.

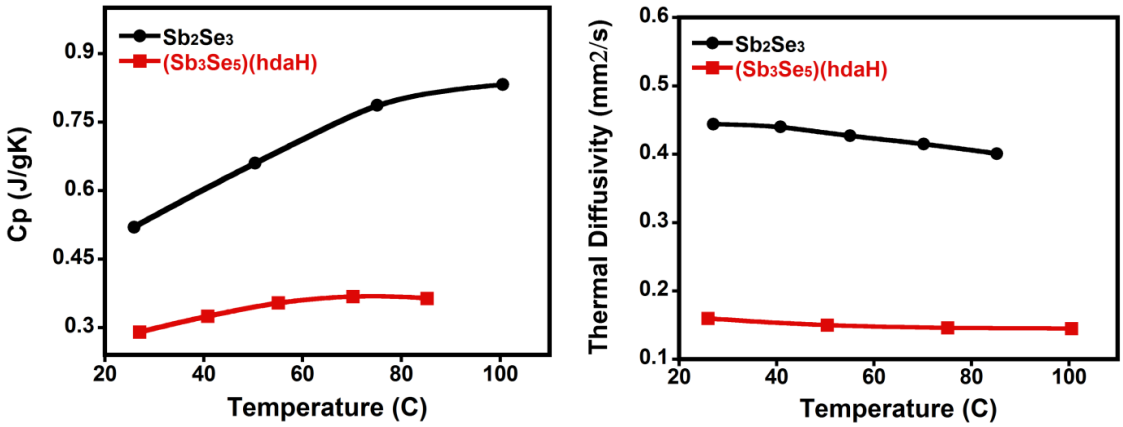

(a) **(b)**

Figure 4.21 (a**)** Specific heat, (b) thermal diffusivity plots for (Sb_3Se_5)(*hda*H) in comparison with Sb_2Se_3 as a reference material.

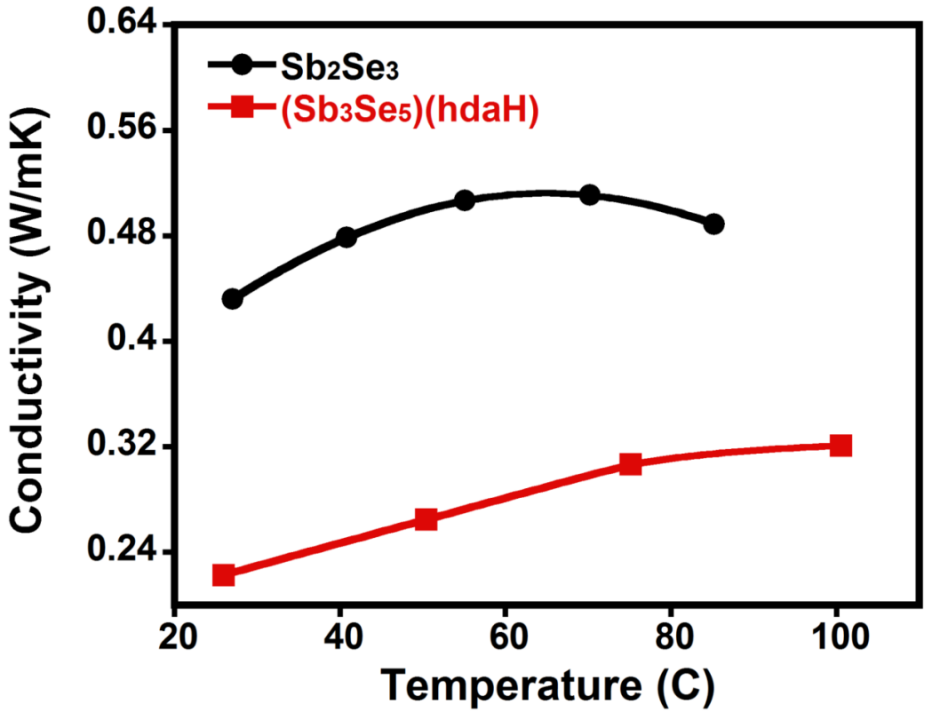

Figure 4.22 Thermal conductivity plots for (Sb_3Se_5)(*hda*H) and Sb_2Se_3.

4.3.3 Properties

Thermal properties: Compound **3** is stable up to 130 ˚C, then shows the weight loss of 8.2% (**Fig. 4.24**) which is slightly higher than the calculated value for losing the organic amine (calculated weight loss: 5.18%). This might be due to the impurities or existence of solvent on the surface of the sample. PXRD of the residue after the initial weight-loss and before the decomposition shows the reflections of Sb_2Se_3 in the samples. Final decomposition starts to occur at around 360˚C.

Optical properties: (Sb_7Se_{11})(*amp*H) has a band-gap of 0.6eV which is narrower than that of the Sb_2Se_3 parent structure (~1.1eV) (**Fig. 4.25**). This might be due to the presence of aromatic rings delocalized electrons in the channels of the structure.

Electrical conductivity: Electrical resistivity of compound **3** (8.03×10^5 Ωcm) (**Fig. 4.26**) is in the same range as that of the Sb_2Se_3 ($\rho = 7 \times 10^5$ Ωcm). Higher electrical conductivity of compound **3** is expected due to its smaller band-gap. It can be attributed to the presence of aminopyridine molecules with delocalized electrons, in the channels of structure. Presence of aromatic rings with π system in the structure may induce tunneling of electrons. Electron tunneling leads to an increase in the density of electrons and improve the electrical conductivity of the compound.

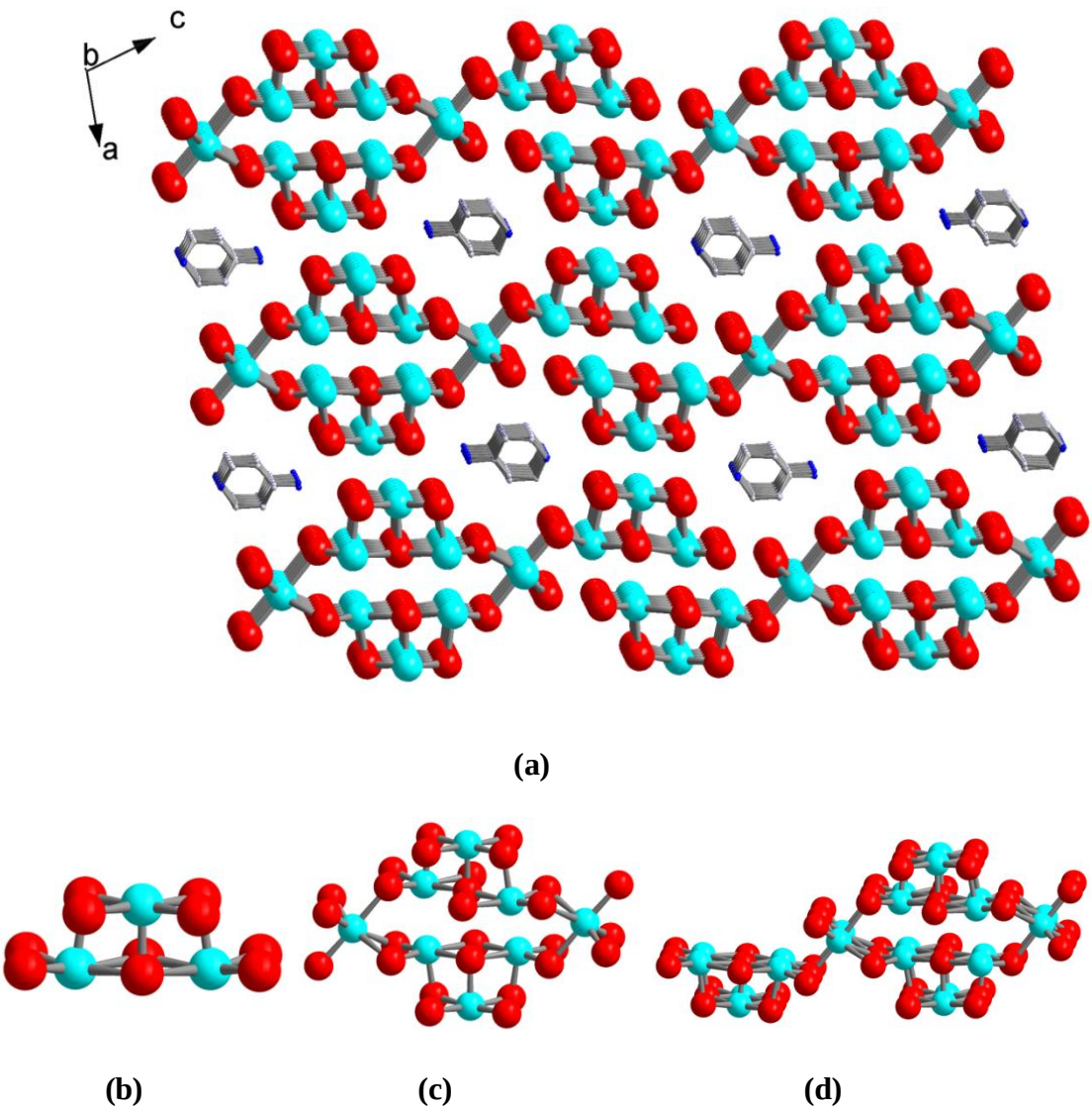

Figure 4.23 (a) View of the structure of **3** along the b axis, showing the location of organics amines molecules, (b) Sb_3Se_5 units formed by edge-sharing of three $SbSe_5$, (c) shows the connection of two Sb_3Se_5 units via corner-sharing, (d) connection of $\{Sb_3Se_5\}_2$ to another Sb_3Se_5 unit via six coordinated Sb atoms. Se atoms are red, antimony atoms are blue.

Thermal conductivity: In contrast to the other two hybrid compounds, (Sb_7Se_{11}) (*amp*H) thermal conductivity is higher than that of the Sb_2Se_3 inorganic reference. Specific heat capacity (**Fig. 4.27a**) increases while there is a slight decrease in thermal diffusivity (**Fig. 4.27b**). This leads to a net increase in thermal conductivity with temperature (**Fig. 4.28**).

Table 4.6 Crystal and structure refinement data for compound **3**

Formula	C5 H6 N2 Sb7 Se11	**T (K)**	160
Fw	1814.93	**Z**	4
crystal system	Monoclinic	**D_{cal} (mg/m^3)**	4.825
space group	C2/m	**total reflns**	7525
a (Å)	23.691(5)	**Unique reflns**	7525
b (Å)	3.9633(8)	**F (000)**	3128.0
c (Å)	27.770(5)	**R1[$I > 2\sigma(I)$]**	0.0824
α (deg)	90	**wR2[all data]**	0.2163
β (deg)	106.502(5)	**GOF**	4.825
γ (deg)	90	***V* (Å^3)**	2500.1(9)

Table 4.7 Selected bond distances (Å) and angels (deg) for Compound **3**

Sb(1)-Se(1)#1	2.630(4)	Sb(6)-Se(8)	2.566(2)
Sb(1)-Se(1)	2.637(3)	Sb(6)-Se(10)	2.685(4)
Sb(1)-Se(3)	2.766(2)	Sb(6)-Se(10)#1	2.698(4)
Sb(1)-Se(2)	3.001(2)	Sb(6)-Se(6)#1	3.153(4)
Sb(1)-Se(10)#2	3.228(4)	Sb(6)-Se(6)	3.155(4)
Sb(1)-Se(10)#3	3.244(4)	Sb(7)-Se(9)	2.587(2)
Sb(2)-Se(4)	2.593(2)	Sb(7)-Se(11)	2.660(4)
Sb(2)-Se(2)#4	2.680(4)	Sb(7)-Se(11)#1	2.667(4)
Sb(2)-Se(2)	2.697(4)	Se(10)-Sb(1)#3	3.228(3)
Sb(5)-Se(5)#1	2.825(4)	Sb(7)-Se(7)	3.300(3)
Sb(2)-Se(6)	3.152(4)	Se(1)-Sb(1)#4	2.630(4)
Sb(3)-Se(5)	2.625(2)	Se(2)-Sb(2)#1	2.680(4)
Sb(3)-Se(3)#4	2.735(4)	Se(3)-Sb(3)#1	2.735(4)
Sb(3)-Se(3)	2.766(4)	Se(4)-Sb(4)#4	2.926(4)
Sb(3)-Se(7)#4	3.024(4)	Sb(5)-Se(5)	2.860(4)
Sb(3)-Se(7)	3.043(4)	Se(6)-Sb(2)#1	3.144(4)
Sb(4)-Se(6)	2.549(2)	Se(6)-Sb(6)#4	3.153(4)
Se(10)-Sb(1)#2	3.244(4)	Se(7)-Sb(3)#1	3.024(4)
Sb(4)-Se(4)	2.828(4)	Se(7)-Sb(7)#1	3.271(3)
Sb(4)-Se(8)	2.923(4)	Sb(5)-Se(7)	2.553(2)
Sb(4)-Se(4)#1	2.926(4)	Se(9)-Sb(5)#4	2.878(4)
Se(8)-Sb(6)-Se(10)	90.85(11)	Sb(7)-Se(9)-Sb(5)	98.87(10)
Se(3)-Sb(3)-Se(7)	91.09(12)	Se(5)-Sb(3)-Se(3)	84.70(9)
Se(7)#4-Sb(3)-Se(7)	81.51(5)	Se(3)#4-Sb(3)-Se(3)	92.12(6)
Se(1)#1-Sb(1)-Se(1)	97.52(7)	Se(1)#1-Sb(1)-Se(1)	97.52(7)
Se(1)-Sb(1)-Se(3)	92.20(9)	Se(4)-Sb(4)-Se(4)#1	86.98(6)
Se(1)#1-Sb(1)-Se(2)	86.94(9)	Se(8)-Sb(4)-Se(4)#1	90.44(13)
Se(1)-Sb(1)-Se(2)	87.17(9)	Se(7)-Sb(5)-Se(5)#1	86.99(9)
Se(6)-Sb(4)-Se(8)	86.64(10)	Se(7)-Sb(5)-Se(5)	86.95(10)
Se(11)#1-Sb(7)-Se(7)	94.39(11)	Se(5)#1-Sb(5)-Se(5)	88.34(6)
Se(1)-Sb(1)-Se(10)#2	92.88(11)	Se(7)-Sb(5)-Se(9)#1	89.59(9)
Se(3)-Sb(1)-Se(10)#2	98.07(8)	Se(5)#1-Sb(5)-Se(9)#1	93.12(13)
Sb(6)#4-Se(6)-Sb(6)	77.80(5)	Sb(3)-Se(5)-Sb(5)	96.86(10)
Sb(5)-Se(7)-Sb(3)#1	93.93(10)	Sb(5)#4-Se(5)-Sb(5)	88.34(6)
Sb(5)-Se(7)-Sb(3)	93.98(10)	Sb(4)-Se(6)-Sb(2)#1	92.59(10)
Sb(3)#1-Se(7)-Sb(3)	81.51(5)	Sb(4)-Se(6)-Sb(2)	89.68(9)
Sb(5)-Se(7)-Sb(7)#1	90.04(9)	Sb(2)#1-Se(6)-Sb(2)	77.98(5)
Sb(2)-Se(4)-Sb(4)#4	96.87(10)	Sb(4)-Se(6)-Sb(6)#4	89.95(9)

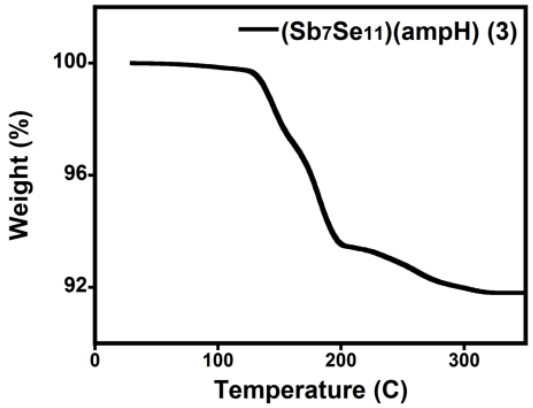

Figure 4.24 TGA data showing weight losses of 8.2% for (Sb_7Se_{11})(*amp*H).

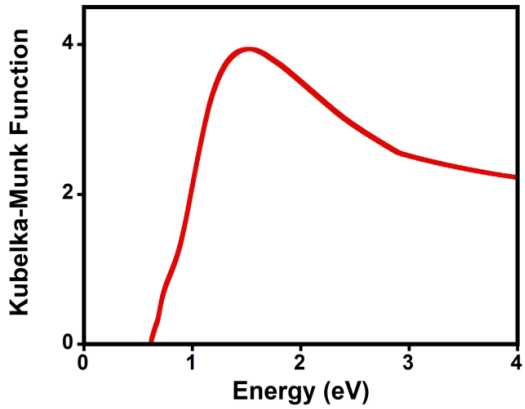

Figure 4.25 Room temperature optical absorption spectra of (Sb_7Se_{11})(*amp*H).

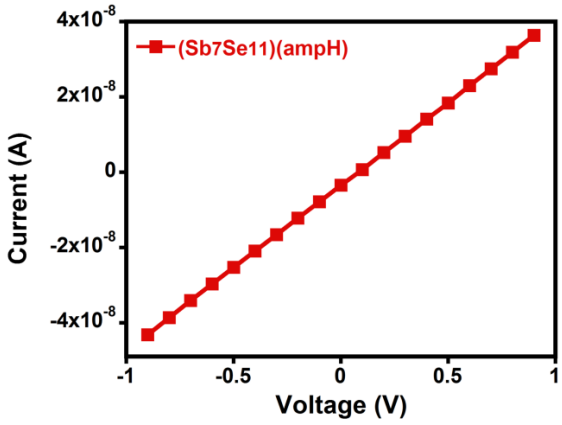

Figure 4.26 I-V curve for (Sb_7Se_{11})(*amp*H).

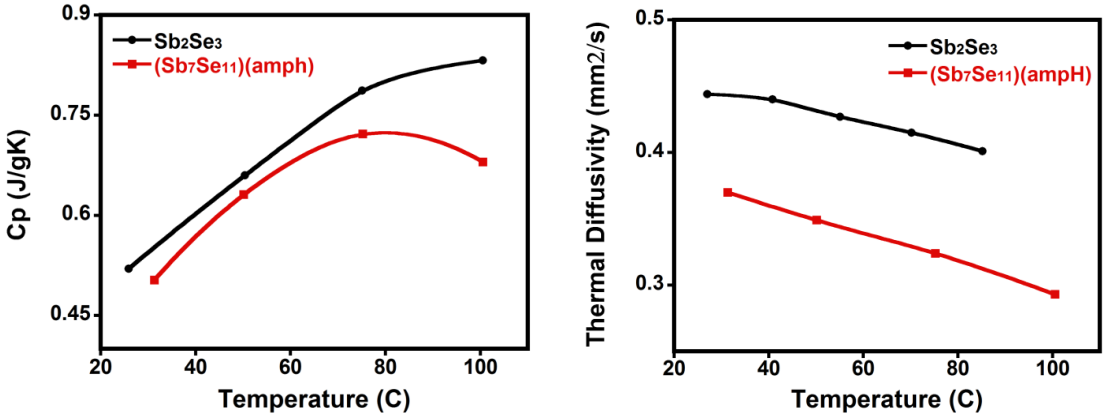

(a) **(b)**

Figure 4.27 (a**)** Specific heat, (b) thermal diffusivity plots for (Sb_7Se_{11})(*amp*H) in comparison with Sb_2Se_3 reference material.

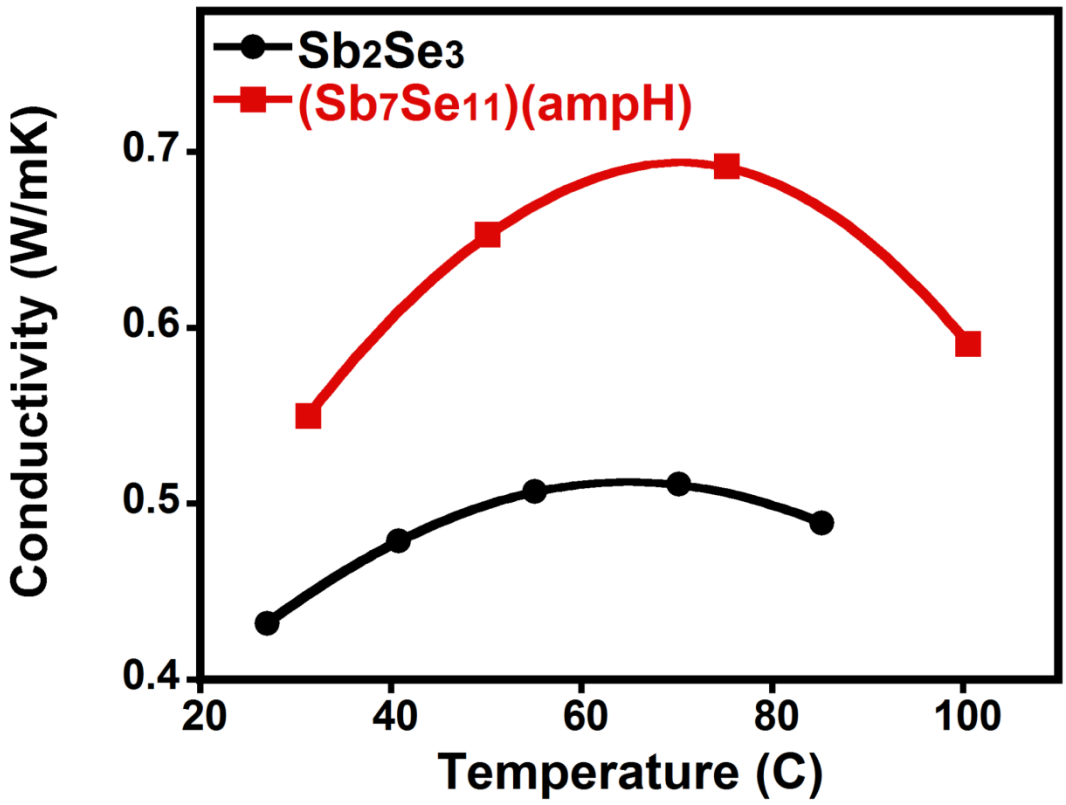

Figure 4.28 Thermal conductivity plots for (Sb_7Se_{11})(*amp*H) compare to the Sb_2Se_3 reference material.

4.4 $(Sb_2Se_3)(Sb_3Se_5)$(*ba*H) (4)

4.4.1 Synthesis and Structure

Mixing 2 mmol of antimony, 3 mmol of selenium in butyl amine afforded the dark needle crystals of $(Sb_2Se_3)(Sb_3Se_5)$(*ba*H). This compound crystallizes in P-monoclinic space group with P-monoclinic, a = 13.76Å, b = 3.963 Å, c = 18.30 Å, β = 100.57˚, volume = 980.6Å^3 and is iso-structural with compound **1** described earlier. The PXRD pattern of $(Sb_2Se_3)(Sb_3Se_5)$(*ba*H) compare to the simulated pattern of compound 1 is shown in **Figure 4.29**.

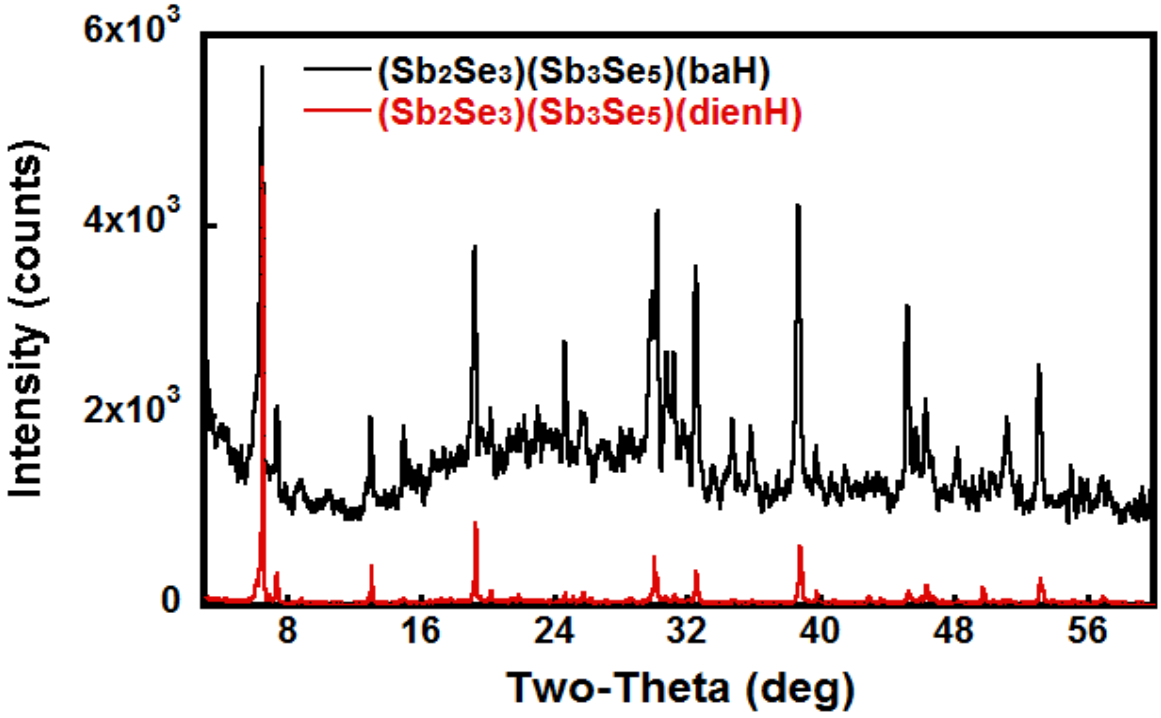

Figure 4.29 Powder x-ray pattern of $(Sb_2Se_3)(Sb_3Se_5)$(*ba*H) (black) compare to that of the $(Sb_2Se_3)(Sb_3Se_5)$(*dien*H).

4.4.2 Properties

Thermal properties: Compound **3** is thermally stable up to around 120 ˚C and then shows the weight loss of 6.37% in one step (**Fig. 4.30**). This weight loss is slightly higher than the calculated value for the loss of organic amine (5.5%) which can be due to the presence of small amount of impurities. The powder x-ray pattern of residue after the first step of weigh loss shows the reflections for Sb_2Se_3. The compound is fully decomposes after 250 ˚C.

Optical properties: Despite being isostructural with the $(Sb_2Se_3)(Sb_3Se_5)$(*dien*H), $(Sb_2Se_3)(Sb_3Se_5)$(*ba*H) has a larger band-gap of 1.2eV (**Fig 4.31**). This difference in the band-gap might be due to the different nature or arrangement of organic spacer in the structure. Further study of the electronic structure and band-gap calculations might shine a light on this issue.

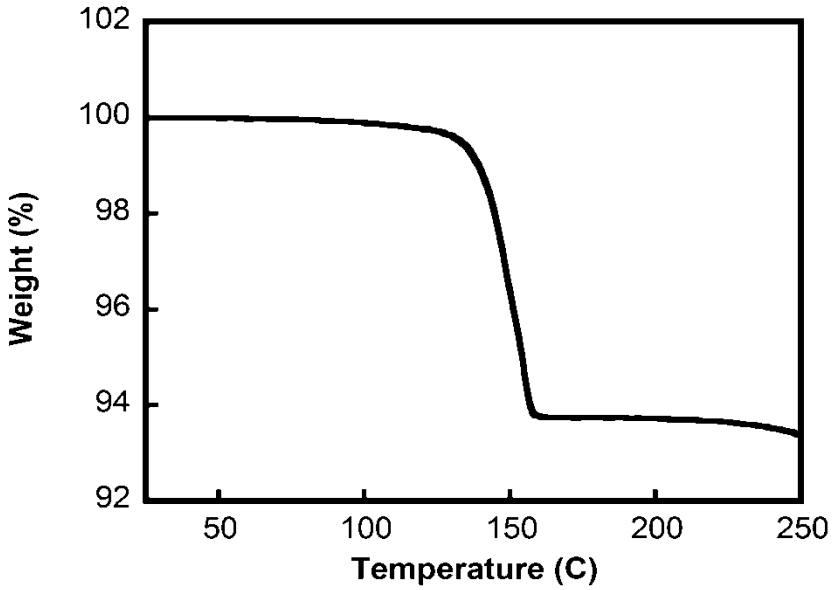

Figure 4.30 TGA data showing weight loss of 6.37% for $(Sb_2Se_3)(Sb_3Se_5)$(*ba*H).

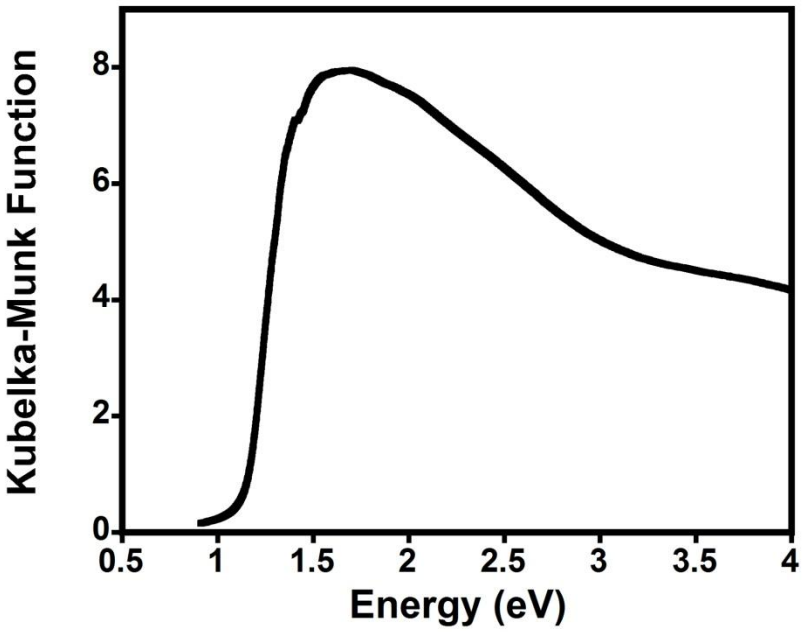

Figure 4.31 Room temperature absorption spectrum of $(Sb_2Se_3)(Sb_3Se_5)$(*ba*H) showing the band-gap of 1.2eV.

4.5 Bismuth based hybrids

Currently, there are no literature data available for hybrid compounds based on bismuth chlcogenides and no structure has been reported. The sole example of selenobismuthate is $(NEt_4)(BiSe_2)$.[15]Our effort to synthesis Bismuth chalcogenide based hybrid resulted in a formation of new compounds. Due to the lack of single crystal, their crystal structure is not known but results obtained based on the X-ray diffraction and TGA data indicate the presence of organic amine in the structure. Few examples of such compounds are presented here.

4.5.1 Bi_xS_y (*L*), (*L = en, pda*)

Synthesis: Bi_xS_y (*L*) was synthesized by mixing of $BiCl_3$ (2mmol) and S (3mmol) in 6 ml of ethylendiamine or 1,3-propanediamine (6ml) in a digestion bomb. The reaction was

placed in the oven and heated at 80 ˚C for 6 days. Product was washed with water and ethanol and then was dried at 60 ˚C in a vacuum oven for 20 minutes. Black powder with 80% yield based on S was obtained. Same products were obtained at 60 ˚C and 100 ˚C, while heating to higher temperatures resulted in the formation of the binary phase of Bi_2S_3.

Structure: Powder X-ray patterns of both $Bi_xS_y(en)_z$ (**Fig. 4.32**) and Bi_xS_y (*pda*) show a small peak at around 6.5 degree. This low angle peak is due to the enlargement of unit cell and indicates that the *en* or *pda* molecules are incorporated into the structure.

Band-gap: Both compounds have a direct band gap of 1.2 eV which is smaller than that of the Bi_2S_3 binary compound. **Figure 4.33** shows the absorption spectra of the two hybrid compounds compare to that of the Bi_2S_3 which was synthesized via solvothermal method at 150 ˚C. Results suggest that the length of the amine's chain doesn't have a significant effect of the determining the band-gap. This result is consistent with the obtained results from the previous studies on the II-VI based hybrid compounds. Further studies, such as band-gap calculations or crystal structure determination, are required for better understanding of this matter.

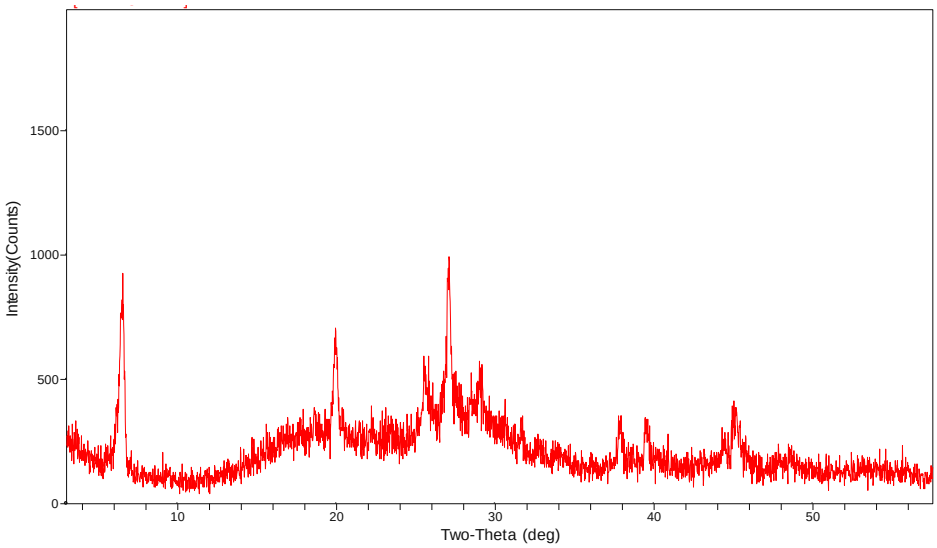

Figure 4.32 PXRD pattern of Bi_xS_y (*en*).

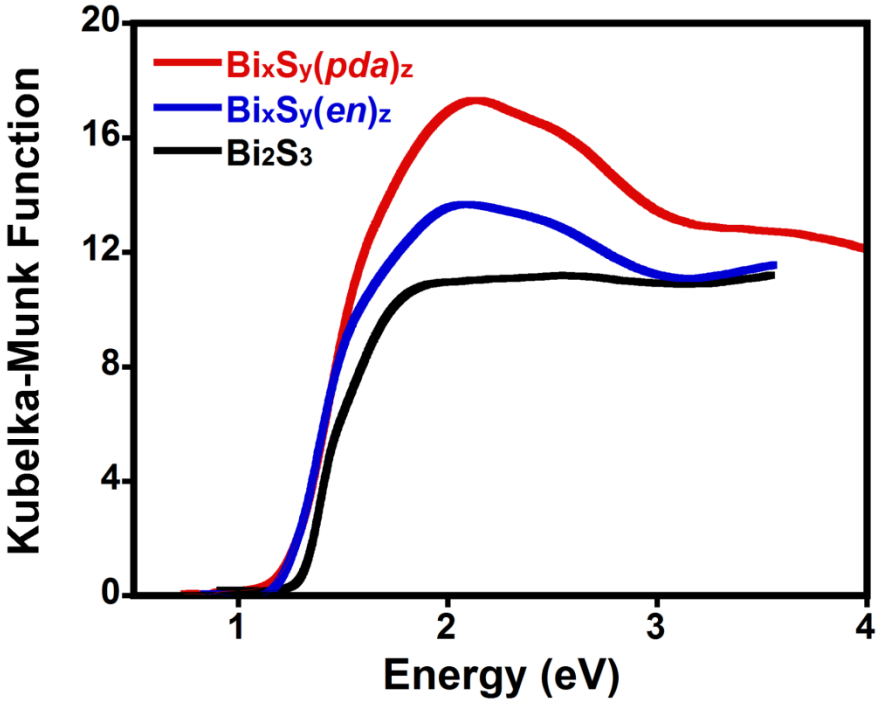

Figure 4.33 Room temperature absorption spectra of Bi_xS_y(*en*) and Bi_xS_y(*pda*) compared to that of the Bi_2S_3.

Thermal properties: 10 mg of sample was heated to sample to 300˚C at the rate of 10˚C/min. TGA shows a weight loss of 3.5% for Bi_xS_y(*en*) , and 17% for Bi_xS_y(*pda*) . The post TGA powder X-ray patterns for both samples show the existence of pure binary Bi_2S_3 compound.

Electrical and thermal conductivity: Pellets prepared using the same process as previously described and the measurement was performed using the same procedures. At room temperature Bi_xS_y(*en*) shows an electrical resistivity of 1.6 x 10^3 Ω.cm. Bi_xS_y(*pda*), having a longer organic chain length, shows a resistivity of 5.5 x 10^3Ω.cm which is slightly higher than that of the $Bi_xS_y(en)_z$ .Difference in the resistivity might also be due to the difference in the arrangements organic amines in the structure of these two compounds. At 306K, Bi_xS_y(en) has a low thermal conductivity of 2.73W/mK and its thermal conductivity decreases to 0.8 W/mK as the temperature goes to 150K.

4.5.2 Bi_xSe_y(*en*)

Synthesis: Solvothermal reaction of $Bi(NO_3)_3$(2 mmol), Se (3mmol), and *en* (6 mL) in a acid digestion bomb at 100 °C for 7 days produced black powder of $Bi_xSe_y(en)_z$ with a yield of 75%.

Properties: powder x-ray *pattern of* Bi_xSe_y(*en*) is similar to that of the Bi_xS_y(*en*) and shows a small low angle peak. Upon heating, it shows a weight loss of 7.53% and its optical band-gap is ~ 0.8-0.9eV which is smaller than the band-gap of Bi_xS_y (*en*), as it is expected (**Fig. 4.34**).

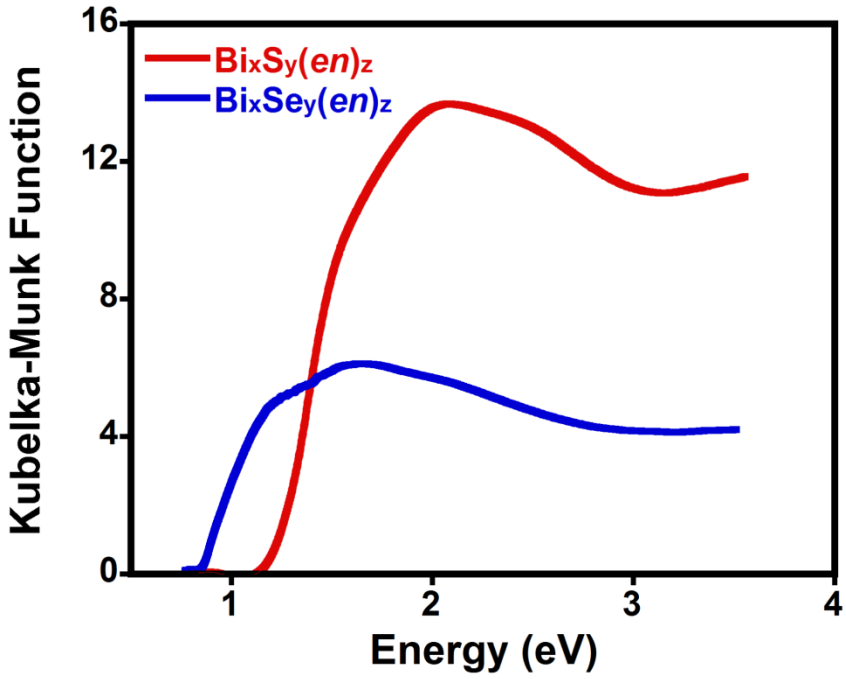

Figure 4.34 Room temperature absorption spectra of $Bi_xSe_y(en)_z$ compared to that of the $Bi_xS_y(en)$.

4.5.3 $Bi_xCu_ySe_z(en)$

Synthesis: The black poly crystalline powder of $Bi_xCu_ySe_z(en)$ with a yield of 50% was obtained from the reaction of elemental Bi, Cu and the excess of Se in ethylendiamine (8 mL) in a 23 mL acid digestion bomb at 120 -150 °C for 7 days.

Properties: Powder X-ray pattern shows that sample is highly crystalline and has a high quality. PXRD pattern is characterized by few well defined, high intensity narrow peaks and a very intense low angle peak at 8 degree (**Fig. 4.35**). PXRD peaks do not match with the reflections of any known compounds which indicate the formation of new phase. This compound has a narrow and direct band-gap of ~0.6 eV (**Fig. 4.36**) and shows high electrical conductivity of 0.58 S/cm (ρ = 1.7Ωcm).

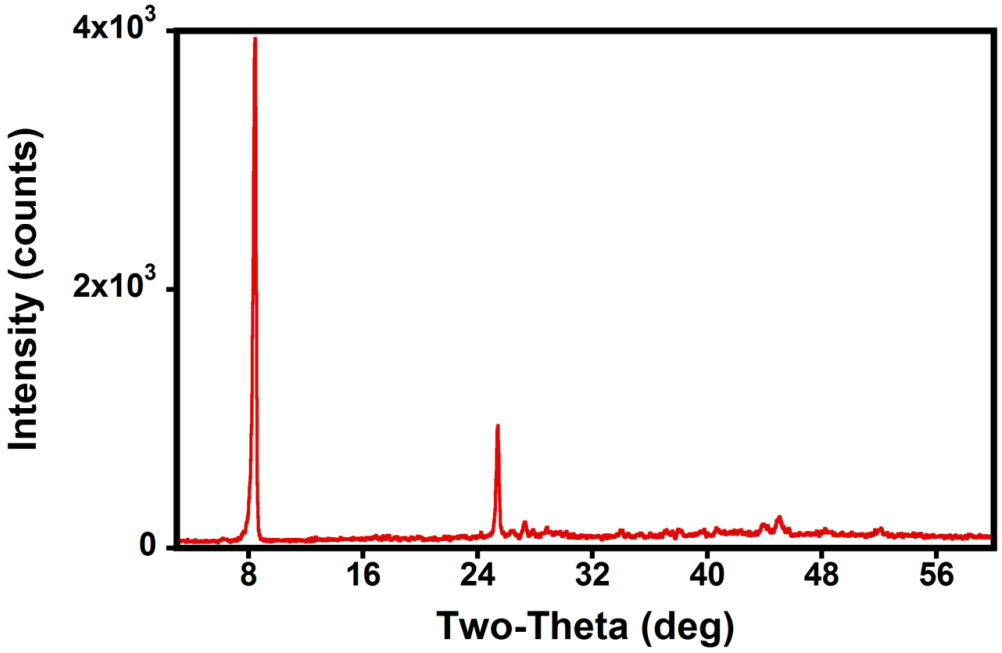

Figure 4.35 PXRD pattern of $Bi_xCu_ySe_z(en)$.

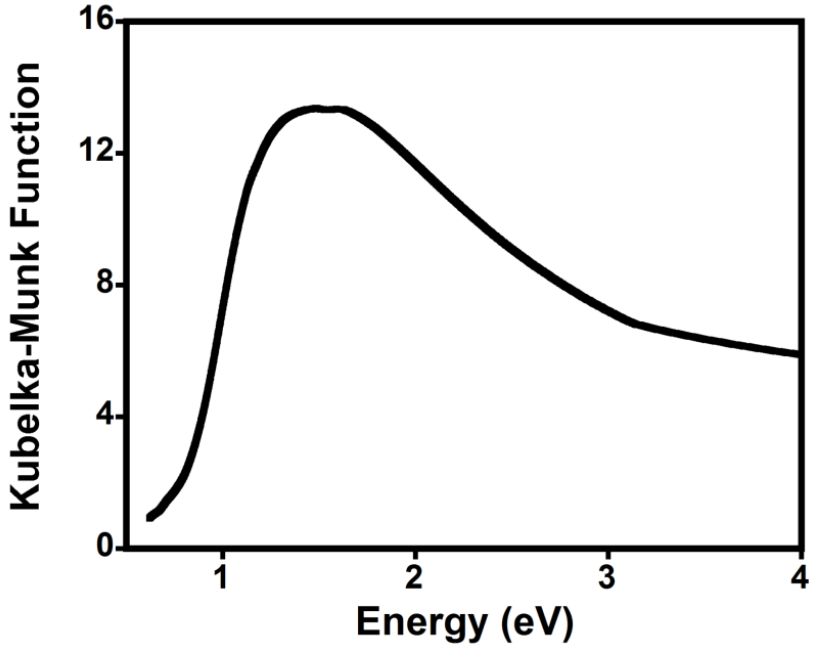

Figure 4.36 Room temperature optical absorption spectrum of $Bi_xCu_ySe_z(en)$.

4.6 Conclusion

A Series of hybrid compounds based on group V-VI semiconductors were prepared by solvothermal methods and their composition, structure, optical, electrical and thermal properties were investigated. Difference in the type and arrangement of organic amines in the structure resulted in three types of new selenoantimonate structures with different properties. Compound $(Sb_2Se_3)(Sb_3Se_5)$(*dien*H) and (Sb_7Se_{11})(*amp*H), in which organic amines are arranged in between the channels, have a narrow band-gap of 0.9 and 0.6eV respectively. While in compound (Sb_3Se_5)(*hda*H), in which the ligands are in between and perpendicular, band-gap is larger. Arrangement of organic ligands also affects the conductivity, both thermal and electrical, of the products. Thermal and electrical conductivities in (Sb_3Se_5)(*hda*H) samples, are lower than in $(Sb_2Se_3)(Sb_3Se_5)$(*dien*H), in which amines are in the channels formed by inorganic chains. Introducing the organic molecule in the structure leads to increase in phonon scattering and as a result the thermal conductivitis of (Sb_2Se_3) (Sb_3Se_5)(*dien*H) and (Sb_3Se_5)(*hda*H), are lower than that of the Sb_2Se_3 inorganic binary phase. Interestingly, when organic ligand with an aromatic ring, with delocalized electrons, was used in the structure, both electrical and thermal conductivity increased (e.g. (Sb_7Se_{11})(*amp*H)). Layered structure, direct and narrow optical band-gap and low thermal conductivity of these hybrid compounds based on group V-VI semiconductors makes them promising candidates for wide range of applications such as photovoltaics and thermoelectrics.

4.7 References

1. a) Y. Itzhaik, O. Niitsoo, M. Page, G. Hodes, G. *J. Phys. C* **2009**, *113*, 4254; b) Y.R. Lazcano, Y. Pena, M.T.S. Nair, P.K. Nair, *Thin Solid Films* 2005, *493*, 77; c) Z.R. Geng, M.X. Wang, G.H. Yue, P.X. Yan, *J. Crystal Growth* **2008**, *310*, 341.

2. a) K.Y. Rajpure, C.H. Bhosale, *Materials Chem. and Phys*. **2002**, *73*, 6; b) K.Y Rajpure, C.D Lokhande, C.H Bhosale, *Thin solid films*, **1997**, *311*, 114; c) N.S. Platakis, H.C. Gatos, *Phys. Status Solidi A* **1972**, *13*, K1; d) P**.** Arun, A. G. Vedeshwar, N. C. Mehra, *J. Phys. D: Appl. Phys.* **1999**, *32*, 183.

3. a) L.M. Peter, K.G.U. Wijiayantha, D.J. Riley, J.P. Waggett, *J. Phys. Chem. B.* **2003**, *107*, 8378; b) M.W. Shao, M.S. Mo, Y. Cui, Y. Chen, Y.T. Qian, *J. Crystal Growth* **2001**, *233*, 799.

4. a) D.G. Walker, A. Bulusu, *Supper Lattices and Microstructures* **2008**, *44*, 1; b) Shevelkov, A.V. *Russian Chemical Reviews* **2008**, *77*, 1.

5. L.D. Hicks, M.S. Dresselhaus, *Phys. Rev. B* **1993,** *19*, 12727.

6. J.O. Sofo, G.D. Mahan, *Appl. Phys. Lett.* **1994**, *65*, 2690.

7. a) B. Seidlhofer, V. Spetzler, C. Näther, W. Bensch, *J. Solid State Chem*. **2012**, *187*, 269; b) M. L. Feng, Z. L. Xie, X.Y. Huang, *Inorg. Chem.* **2009**, 48, 3904; c) V. Spetzler, C. Näther, W. Bensch, *J. Solid State. Chem.* **2006,** *179*, 3541.

8. a) Z. Rejai, H. Lühmann, C. Näther, R. K. Kremer, W. Bensch, *Inorg chem.* **2010,** *49* 1651; b) M. Zhang, T. L. Sheng, X. H. Huang, R. B. Fu, X. Wang, S. M. Hu, S. C. Xiang, X. T. Wu, *Eur. J. Inorg. Chem.* **2007**, *2007*, 1606; c) P. Vaqueiro, A. M. Chippindale, A. R. Cowley, A. V. Powell, *Inorg chem*. **2003,** *42*, 7846.

9. a) L. Engelke, C. Näther, W. Bensch, *Eur. J. Inorg. Chem*, **2002**, *2002*, 2936; b) J. L. Mertz, N. Ding, M. G. Kanatzidis, *Inorg chem*. **2009**, *48*, 10898; c) J. Zhou, X. H Yin, F. Zhang, *Inorg. Chem*. **2010**, *49*, 9671; d) A. Puls, M. Schaefer, C. Nather, W. Bensch, A.V. Powell, S. Boissiere, A.M. Chippindale, *J. Solid State Chem.* **2005**, *178*, 1171.

10. a) D. Jia, Y. Zhang, Q. Zhao, J. Deng. Inorg. Chem. **2006,** 45, 9812; b) Z. Chen, R. E. Dilks, R. J. Wang, J. Y. Lu, J. Li, *Chem. Mater*, **1998,** *10*, 3184; c) T. van Almsick, W. S. Sheldrick, *Z. Anorg. Allg. Chem.* **2006,** *632*, 1413; d) Z. Chen, R.J. Wang, X.Y. Huang, J. Li, Acta Cryst. **2000,** C56, 1100.

11. a) D. X. Jia, A.M. Zhu, Q.Y. Jin, Y. Zhang, W.Q. Jiang, *J. Solid State Chem*. **2008**, *181*, 2370; b) D. X. Jia, Q. Jin, J. Chen, Y. Pan, Y. Zhang, *Inorg Chem.* **2009**, *48*,

8286; c) D. X. Jia, Q. X. Zhao, Y. Zhang, J. Dai, J. Zhou, *Eur. J. Inorg. Chem.* **2006**, *37*, 2760.

12 N.W. Tideswell, F.H. Kruse, J.D. McCullough, *Acta Cryst.* **1957**, *10*, 99.

13. D. G. Cahill, W. K. Ford, K. E. Goodson, G. D. Mahan, A. Majumdar, H. J. Maris, R. Merlin, and S. R. Phillpot, *J. Appl. Phys.* **2003**, *93*, 793.

14. a) X. Zheng, Y. Xie, L. Zhu, X. Jiang, Y. Jia, W. Song, Y. Sun, *Inorg. Chem.* **2002**, *41*,455; b) Y. Rodríguez-Lazcano, Y. Peña, M.T.S. Nair, P.K. Nair, *Thin Solid Films*,**2005**, *493*, 77; c) K.Y. Rajpure, C.H. Bhosale, *Materials Chem. and Phys.* **2002**, *73*, 6.

15. M. A. Pell, J. A. Ibers, *Inorg. Chem* **1996**, *35(16)*, 4559.

APPENDIX I

METHODS AND INSTRUMENTS

Powder X-ray diffraction is a common method for characterization of solid materials. Each solid has its unique characteristic X-ray powder pattern which can be used for its identification. Powder X-ray diffraction (PXRD) analysis of samples was carried out on a Rigaku D/M-2200T automated diffraction system (Ultima+) using Cu Kα radiation (λ= 1.5406 Å). The data were collected at room temperature in a 2θ range of 3-60˚with a scan speed of 2˚/min. The operating power was 40kV/40mA.

Optical absorption spectra were measured at room temperature on a Schimadzu UV-3600 UV/VIS/NIR spectrometer. The reflectance data were used to estimate the band gap using Kubelka-Munk function, $\alpha/S = (1-R)^2/2R$, [1] where α is the absorption coefficient, S is the scattering coefficient and R is the reflectance. This graph would show a linear region above the optical absorption edge. Extrapolation of this line to the photon energy (h*v*) axis gives information about the band gap energy of the material. $BaSO_4$ powder was used as standard (100% reflectance). Wavelength range of 200-2000 nm was used for data collection. Kubelka-Munk function *F*(R) vs. h*v* was plotted.

Thermogravimetric (TG) analyses of samples were performed using the TA Instrument Q50 thermal gravimetric analyzer with nitrogen flow and sample purge rate at 40 ml/min and 60 ml/min respectively. About 10 mg of sample was loaded onto a platinum sample pan and heated from room temperature to 600˚C at a rate of 4 or 10 ˚C/min under nitrogen flow.

The room temperature photoluminescence (PL) emission spectra were collected

on a Horiba/Jobin-Yvon Fluorolog-3TM double grating–double grating fluorescence spectrophotometer. Excitation wavelength of 360 nm was used for all samples.

Thermal conductivity measurements were performed on the pellets with diameter of 10 mm and thickness of 1-1.5mm. The thermal diffusivity, specific heat and density of the samples were measured in the temperature range 25°C to 100 °C first and then thermal conductivity was calculated using the following equation: $\kappa = \rho\alpha C_p$, where κ is the thermal conductivity, ρ is the density, α is the thermal diffusivity, and Cp is the specific heat of the material. Thermal diffusivity measurements were carried out using laser flash apparatus LFA 457 Microflash (Netzsch Instruments) and specific heat measurements were made using DSC 204F1(Netzsch Instruments). For thermal diffusivity measurement, bottom face of the sample receives a pulse of radiant energy coming from a laser. The thermal diffusivity value was computed from the resulting temperature response on the opposite (top) face of the sample. Specific heat measurements were made in the temperature range 25 to 100 ºC using DSC 204 F1. The samples were cooled to 9 ºC, held at 9 ºC for 6 minutes and then heated up to 95 ºC. From the ratio of the heat flow to the sample to the heat flow to a standard sapphire sample (of known specific heat) taken through the same temperature program, the specific heat of the sample was determined.

Electrical conductivity measurements: Powder samples were pressed into pellets with the thickness ranging 80-120 micron using a Caver laboratory press under a load of 3.8 tons (2500 atm pressure). Gold contacts were evaporated on these pellets using a thermal evaporator. The I-V curves were obtained by applied voltage in the range of -1 to 1 V with 0.1 V incremental steps. Resistivity was calculated using the equation $\rho = R.d.a/b$ where d is the film thickness, b is the distance between the contacts, a is the length of the

contacts and *R* is resistance which was obtained from the slope of the linear fit to the I-V curve.

CIE Coordinate Calculation: The Horiba Jobin Yvon software package Quantum Yield and Colour Calculator were used for CIE coordination calculations. In CIE 1931 chromaticity diagram coordinates of x = 0.31, y = 0.31 correspond to the pure white light and in CIE-1976 diagram, u′ = 0.20, v′ = 0.46 are coordinates for a white light.

White LED assemblies: After the reaction, the remaining solvent (amine) was removed from the reaction vassal. The product was then mixed with water and ethanol (at 1:1 ratio) and centrifuged (1500rpm for 5 minutes). This process was repeated 3-5 times until a neutral pH was achieved (using pH paper). Finally, dimethylsulfoxide (DMSO) was added and mixed with the solid and centrifuged using the same conditions as above. The obtained gel (~20mg) was added to 10 ml of DMSO and treated by an ultrasonic processor. The resulting dilute gel-like sample was used to set up a WLED assembly. An alternative way to obtain a gel-like sample was by dispersing the powder in DMSO. For the WLED signs shown in Fig. 2.14b and c, solution was coated onto a glass slide and the coated glass slide was placed on top of the UV lamp and excited by a light source with wavelength of 365 nm. For the WLEDs shown in Fig. 2.14a, solution was coated onto the surface of a commercial 360 nm UV-LED.

APPENDIX II

QUANTUM YIELD MEASURMENT

I. Absolute method

Absolute fluorescence quantum yield (PLQY) measurements were carried out on both solution and solid samples using F-3018 Integrating Sphere mounted on the Horiba/Jobin-Yvon Fluorolog-3TM fluorescence spectrophotometer. [2] It is important to have very high reflectance within the sphere. Integrating sphere provides a reflectance >99% over the 400–1500 nm range and its accessories were made from Teflon (**Fig. A1**). A cylindrical optical quartz cuvette with a diameter of 8 mm, equipped with a Teflon stopper was used for measuring the solution samples. About 25 mg of powder was dispersed in 5 ml DMSO. Solvent was spectroscopic grade and optical density of solutions at the excitation wavelength was kept below 0.15. Sample holder was filled with1 ml of the solution and was placed in the sphere. Data were then collected over all emission angles to overcome the orientation dependence and then the data was integrated.

The procedure is as follows: first, the spectrum was recorded for the blank only, *La*, measuring scattered signal (λ_{ex}: 360nm), with a neutral-density filter in the optical path. Integration of the incident beam's signal intensity *I* was performed from 350 to 270nm. Bandpass was adjusted to give a peak intensity of ~1×10^6 counts/s. The same bandpass was used throughout the measurement. Next, the neutral-density filter was removed and the blank's fluorescence was measured and incident beam's signal was integrated from 360 to 710 nm. Intensity should be around 1×10^6 counts. If it is very below 1×10^6 counts/s, then

the last step should be repeated using the stronger filter (0.5% instead of 1%) and then bandpass should be adjusted again. In the third step the sample was placed into the sphere and its fluorescence *Ec* was measured and integrated from 360 nm to 710 nm and at last the sample's scatter *Lc* was measured and integrated from 350 to 270nm. PLQY was then calculated using the following equation: $\Phi f = (Ec\text{-}Ea)/ (La\text{-}Lc)$ Where *E*c and *Ea* are the integrated luminescence of the sample and empty sphere (or blank) respectively, *Lc* and *La* are the integrated excitation profiles of the sample and empty sphere (blank) when they are directly excited by the incident beam. It should be noted that the integration of the wavelengths and calculations was done by the software designed by the Horiba company and came with the integrating sphere. The emission and scattering data was plotted into the software and the software used the input data and performed the calculations. The same procedure was applied on solid samples. In this case, powders were placed on the glass slide and a blank glass slide was used as a reference. The results were in the similar ranges as those from the DMSO dispersed samples (**Table A1**).

Table A1 Summary of PL quantum yields calculated based on comparative and absolute methods

Sample	Trial #1 (solution)		Trial #1 (solution)		Trial #1 (solid)	Average
	Absolute	Relative	Absolute	Relative	Absolute	
$Zn_{1.7}Cd_{0.3}S_2$(*ha*)	17.9	17.3	17.1	16.6	18.0	17.4
$Zn_{1.7}Cd_{0.3}S_2$(*ha*):0.08%Mn	28.6	26.3	28.0	27.0	29.1	27.8
$Zn_{1.7}Cd_{0.3}S_2$(*oa*)	27.4	25.3	26.7	24.8	28.3	26.5
$Zn_{1.7}Cd_{0.3}S_2$(*oa*): 0.08%Mn	36.5	33.3	-	-	37.3	35.7

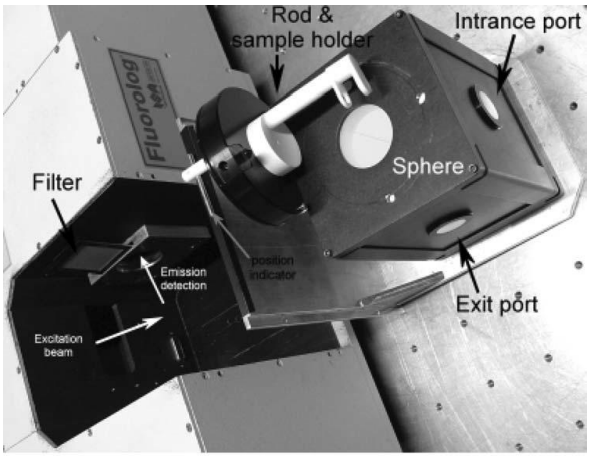

(a)

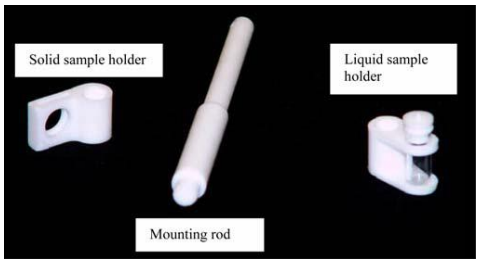

(b)

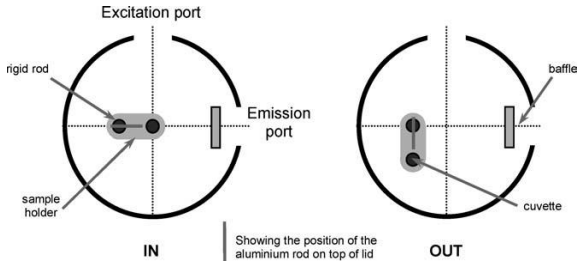

(c)

Figure A1 (a) F-3018 Integrating Sphere mounted on the Horiba/Jobin-Yvon Fluorolog-3TM fluorescence spectrophotometer, (b) sample holders and, (c) position of solid (left) and liquid (right) sample holders used for PLQY measurements in the integrating sphere.

II. Relative/comparative method

In this method a standard is used as a reference and the PLQY is obtained by a comparison of the luminescence spectra of samples of the unknown and standard with normalized absorptions. This method is suitable for the study of weakly absorbing samples. In comparative method the absorption and luminescence of the standard sample should be ideally similar to that of the material under investigation.[3] In this study, comparative method was employed to calculate fluorescence QY of solution samples using trans-

stilbene as a reference dye.[4] For all the measurements the 10 mm fluorescence cuvette was used and the absorbance was kept below 0.1 at the excitation wavelength in order to avoid the re-absorption effects. A constant slit width of 2 nm was used for both UV-vis absorbance and fluorescence measurements of all samples. The stock solution of *trans*-stilbene in hexane was made by dissolving 1 ml of *trans*-stilbene in 20 ml of hexane. UV-vis absorbance spectrum of hexane was recorded as solvent background. Fluorescence spectrum of the same solution was also recorded using the excitation wavelength of 320 nm. Then 50 μL from the stock solution was added to hexane using micropipette and the absorption and fluorescence of the solution were measured. This procedure was repeated 6 times and absorption and PL of the six solutions with increasing *trans*-stilbene concentration were measured. The integrated fluorescence intensity vs absorbance at the excitation wavelength was plotted. The same procedure was applied to another standard, quinine sulfate in 0.1 molar H_2SO_4 and the two standard compounds were cross-calibrated using the following equation: [5]

$$\Phi_X = \Phi_{ST}\left(\frac{\mathrm{Grad}_X}{\mathrm{Grad}_{ST}}\right)\left(\frac{\eta_X^2}{\eta_{ST}^2}\right)$$

Where η is refractive index of the solvent for the standard sample and the test sample, Grad_{ST} and Grad_X are the slope of the intensity-absorbance curves for the standard and the sample, and Φ_{ST} and Φ_X are the quantum yield of the standard and sample, respectively (0.11 for *trans*-stilbene in hexane and 0.54 for quinine sulfate in 0.1 molar H_2SO_4). This was done to ensure that the quantum yields of both standards are in agreement with the reported literature values. A deviation of ±10% is accepted.

After the cross-calibration of the standard samples, the quantum yield for the hybrid sample was measured and the value was calculated using the same equation. Typically, a 25 mg of sample was added to 20 ml of DMSO and dispersed in the solvent by sonication for 3 minutes. Absorption and fluorescence of samples with 5-6 different concentrations were measured and the graphs of integrated fluorescence intensity vs. absorbance at the excitation wavelength (λ_{ex}: 360nm) were plotted. The QY was calculated by inserting the values obtained from the slopes of the graphs in the equation mentioned earlier.

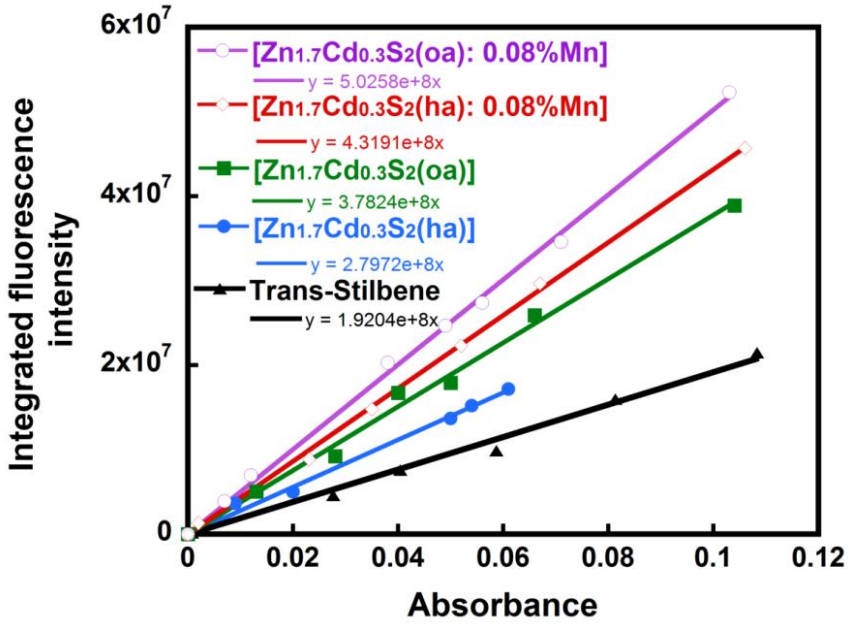

Figure A2 Linear plots of integrated fluorescence intensity vs absorbance for a standard sample, *trans*-stilbene in hexane and hybrid samples, 2D-$Zn_{1.7}Cd_{0.3}S_2$(*ha*), 2D-$Zn_{1.7}Cd_{0.3}S_2$(*oa*), 2D-$Zn_{1.7}Cd_{0.3}S_2$(*ha*):0.08%Mn, and 2D- $Zn_{1.7}Cd_{0.3}S_2$(*oa*):0.08%Mn.

APPENDIX III

EXPERIMENTAL DATA FOR CHAPTER TWO

A. Synthesis of Zn_2S_2(*L*) and its derivatives

All compounds were synthesized using solvothermal reactions. The proper amounts of reactants were weighted, placed into 23 ml Teflon-lined stainless acid digestion bombs and dissolved in the corresponding amine. Amines were used both as a reactant and as a solvent. Reaction of $ZnCl_2$ (0.231 g, 1.7 mmol), $CdCl_2$ (0.68g, 0.3 mmol), and S (0.032 g, 1 mmol), in proper amine (*pa, ba, ha,* and *oa*) (6 ml) at 120 °C for 5 days resulted in a fine powder of of Zn_2S_2 (*L*). Light yellow powder of $Zn_{1.7}Cd_{0.3}S_2$ (*L*) was obtained from reactions of $ZnCl_2$ (0.231 g, 1.7 mmol), $CdCl_2$ (0.68g, 0.3 mmol), and S (0.032 g, 1 mmol), in a desired amine (*pa, ba, ha,* and *oa*) (6 ml) at 120 °C for 5 days (yield ~70% based on S). To remove the organic amine and excess $ZnCl_2$ and $CdCl_2$ after the reaction, the products were filtered and washed with water and ethanol followed by drying with acetone. The resulted powder was dried in the vacuum oven at 50 °C for 10 minutes. To synthesize Mn doped samples, various molar concentrations of Mn were added to the reaction mixture and heated at 120 °C for 5 days (yield ~60% based on S).

B. PXRD

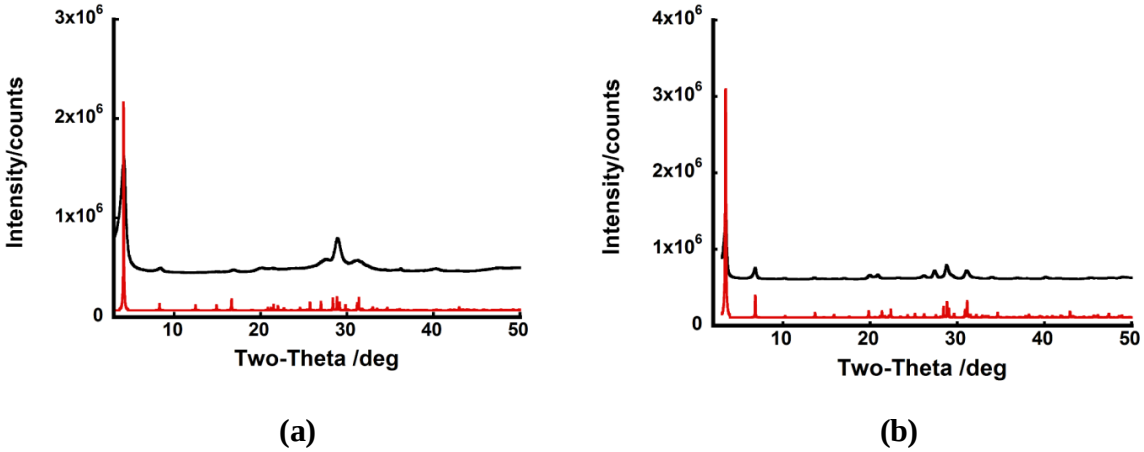

(a) **(b)**

Figure A3 Observed (black) and calculated (red) PXRD patterns of the double layered (a) 2D-Zn_2S_2(*ba*), (b) 2D-Zn_2S_2(*ha*).

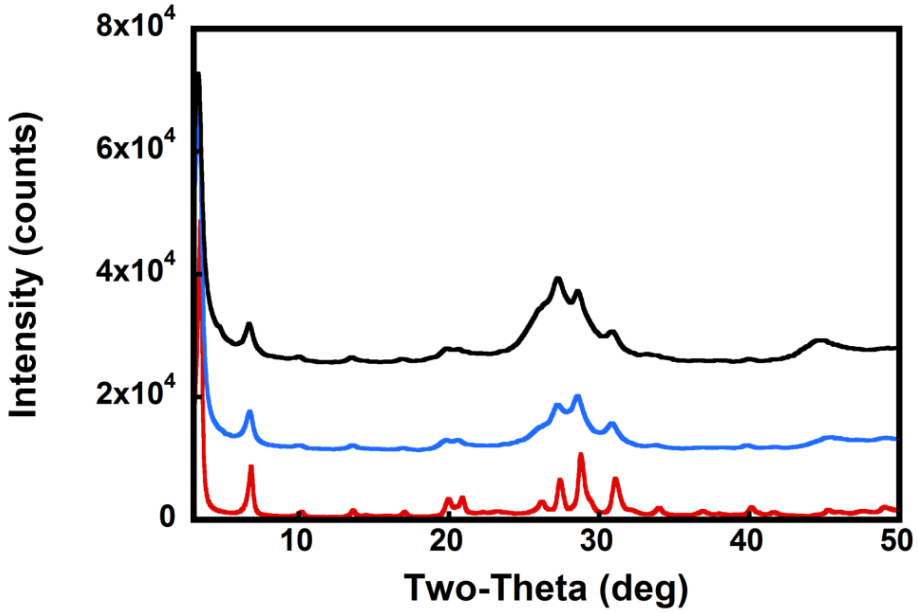

Figure A4 PXRD patterns of refined 2D-Zn_2S_2(*ha*) (red), 2D-$Zn_{1.7}Cd_{0.3}S_2$(*ha*) (blue), and 2D-$Zn_{1.7}Cd_{0.3}S_2$(*ha*):0.08%Mn(black).

C. Thermogravimetric Analysis (TGA)

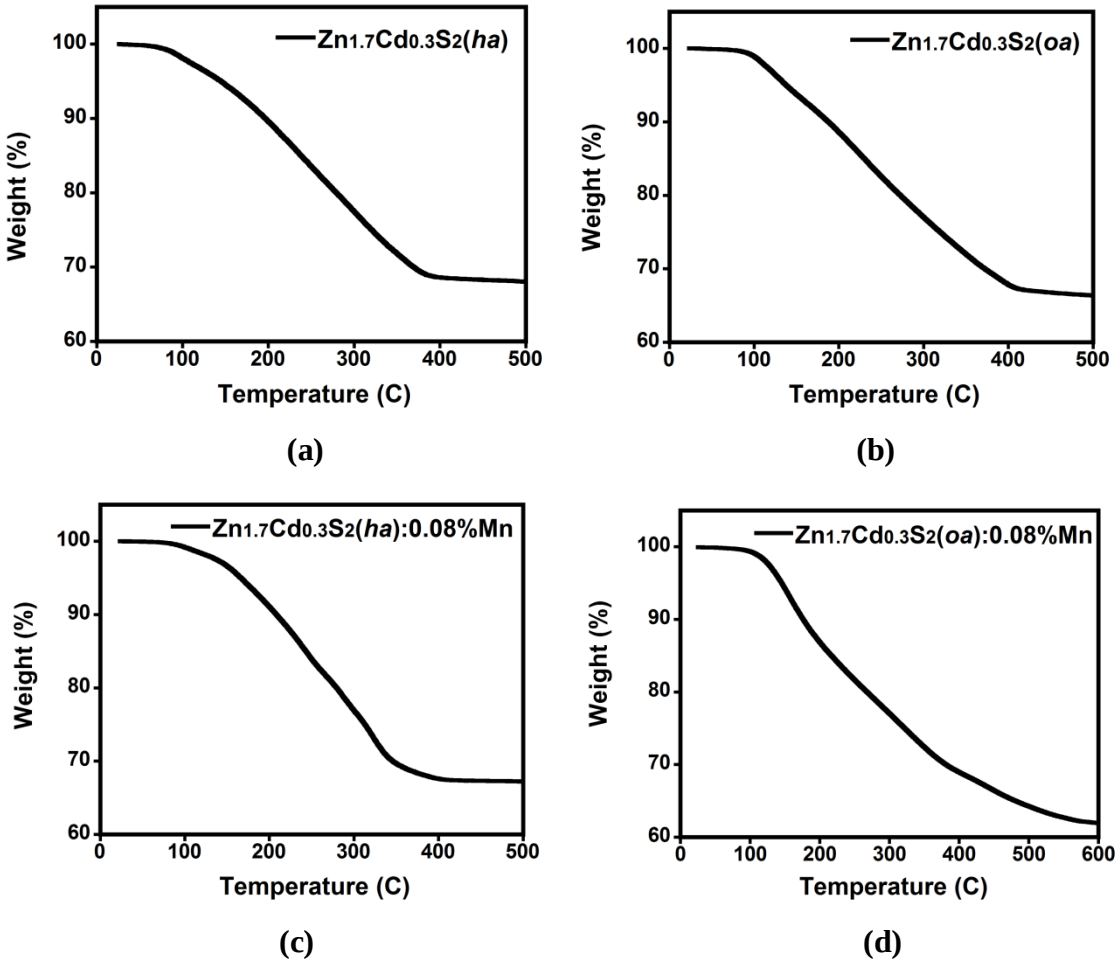

Figure A5 Thermogravimetric analysis (TGA) data showing weight losses of (a) 32.02% for $Zn_{1.7}Cd_{0.3}S_2$(*ha*),(b) 35,77% for $Zn_{1.7}Cd_{0.3}S_2$(*oa*), (c) 32.77% for $Zn_{1.7}Cd_{0.3}S_2$(*ha*):0.08%Mn, and (d) 38.12% for $Zn_{1.7}Cd_{0.3}S_2$(*oa*):0.08%Mn.

Table A2 TGA data for selected samples

Compound	Weight Loss (%) (Cal'd)	Weight Loss (%) (expt)	Possible Residuals
$Zn_{1.7}Cd_{0.3}S_2$(*ha*)	32.62	32.03	$Zn_{7.22}Cd_{2.77}S_{10}$, ZnS, S
$Zn_{1.7}Cd_{0.3}S_2$(*ha*):0.08%Mn	32.63	32.77	ZnS, (Zn,Mn)S, Cd
$Zn_{1.7}Cd_{0.3}S_2$(*oa*)	38.21	35.77	ZnS, CdS, S
$Zn_{1.7}Cd_{0.3}S_2$(*oa*):0.08%Mn	38.22	38.12	ZnS, CdS, MnS, S

D. **CIE coordinates**

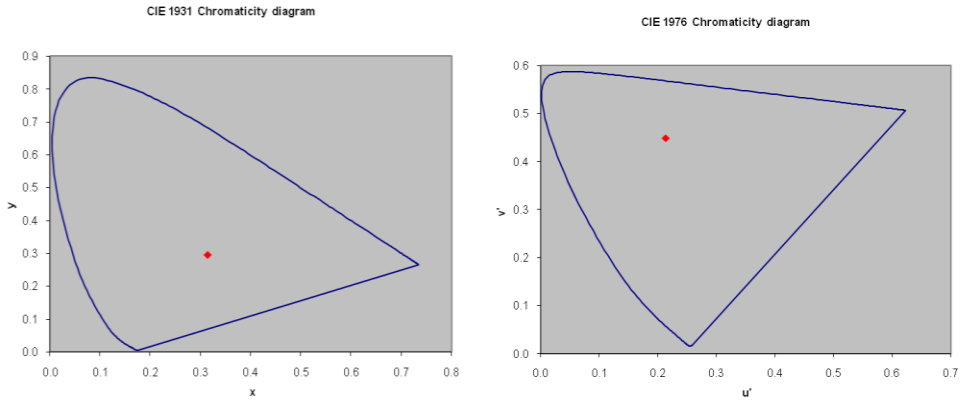

(a)

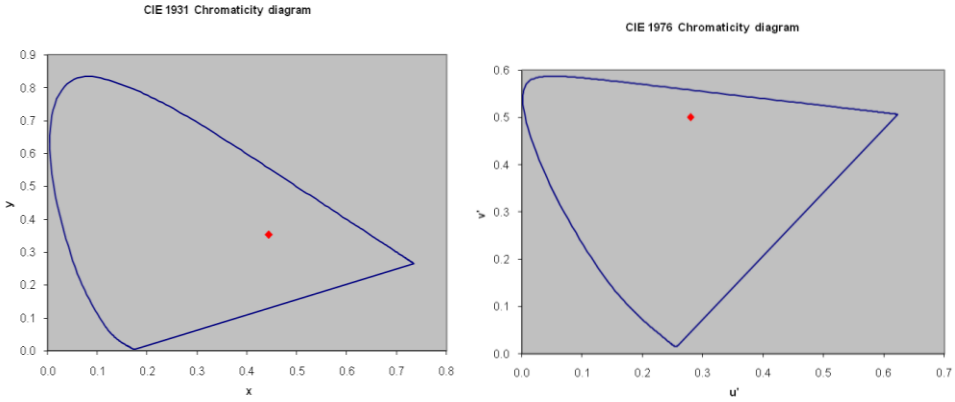

(c)

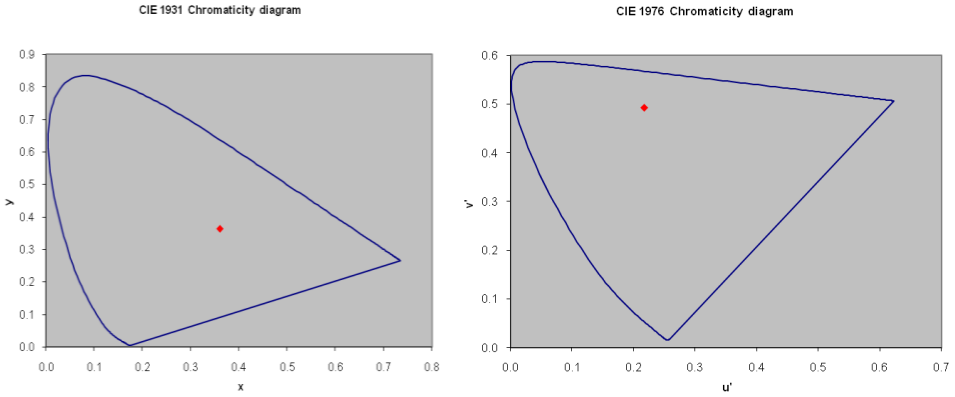

(d)

Figure A6 CIE coordinates of (a) $Zn_{1.7}Cd_{0.3}S_2$(*ha*) (x: 0.31, y: 0.29 and u′: 0.21, v′: 0.44), (b) $Zn_{1.7}Cd_{0.3}S_2$(*oa*) (x: 0.35, y: 0.42 and u′: 0.27, v′: 0.50), and (c) $Zn_{1.7}Cd_{0.3}S_2$(*ha*):0.08% Mn (x: 0.36, y: 0.36 and u′: 0.21, v′: 0.49).

D. Elemental Analysis

Table A3 Summary of elemental analysis for $Zn_{1.7}Cd_{0.3}S_2$(*ha*).

Element	**Experimental (%)**	**Calculated (%)**
C	22.95	23.13
H	4.77	4.84
N	4.29	4.51

References:

1. a) H. G. H. W. WM. Wendlandt, *Reflectance Spectroscopy*, Interscience, A Division of John Wiley & Sons, New York, **1966**; b) G. Kortüm, *Reflectance Spectroscopy*, Springer-Verlag, New York, **1969**.

2. L. Porres, A. Holland, L. O. Palsson, A. P. Monkman, C. Kemp, A. Beeby, *J. Fluo.* **2006**, *16*, 267.

3. a) J. N. Demas, G. A. Crosby, *J. Phys. Chem.***1971**, *75*, 991; b) A. T. R.Williams, S. A.Winefield, J. N. Miller, *Analyst* **1983**, *108*, 1067; c) G. Weber, F. W. J. Teale, *Trans. Faraday Soc.***1957**, *53*, 646.

4. a) A. Nag, D. D. Sarma, *J. Phys. Chem. C* **2007**, *111*, 13641-13644; b) W. Ki, J. Li, *J. Am. Chem. Soc.* **2008**, *130*, 8114.

5. Jobin Yvon Ltd. "A Guide to Recording Fluorescence Quantum Yields" from the website: http://www.jobinyvon.com/SiteResources/Data/MediaArchive/files/applications/quantumyieldstrad.pdf.